Observation of p-wave Capture Strength in the

$^2H(\vec{d},\gamma)^4He$ Reaction at E_d = 80 - 0 keV

by

Laird Hayman Kramer

Department of Physics

Duke University

Date: May 7, 1992

Approved:

Henry R. Weller, Supervisor

Dissertation submitted in partial fulfillment of
the requirements for the degree of Doctor
of Philosophy in the Department of
Physics in the Graduate School
of Duke University

1992

Abstract

Observation of p-wave Capture Strength in the $^2H(\vec{d},\gamma)^4He$ Reaction at E_d = 80 - 0 keV

The $^2H(d,\gamma)^4He$ reaction is expected to be dominated by electric quadrupole (E2) s-wave ($\ell = 0$) capture to the D-state ($\ell = 2$) of ^4He below E_d(lab) = 500 keV, where the centrifugal barrier should suppress the electric quadrupole (E2) d-wave ($\ell = 2$) capture to the S-state ($\ell = 0$). Enhancement of the total cross section below E_d(lab) = 500 keV has been attributed to this mechanism, although no direct evidence exists to support this claim.

To investigate this issue, we have measured the vector and tensor analyzing powers of the $^2H(\vec{d},\gamma)^4He$ reaction using an 80 keV beam of polarized deuterons. We present results for the vector and tensor analyzing powers $A_y(\theta)$ and $A_{yy}(\theta)$ and the differential cross section $\sigma(\theta)/A_0$ for E_d(lab) = 80 - 0 keV at $\theta_{c.m.} = 0°$, 45°, and 82°. A model-independent transition matrix element analysis of the data finds that a major portion of the capture strength results from electric dipole (E1) and magnetic quadrupole (M2) p-wave capture ($\ell = 1$). The data are also compared to a recent microscopic coupled-channel resonating group model calculation which includes electric quadrupole (E2), electric dipole (E1), magnetic quadrupole (M2), and magnetic dipole (M1) transitions and the coupled deuteron-deuteron, proton-triton, and neutron-^3He channels. The model produces fair agreement with the experimental data when a semi-realistic force is used.

Acknowledgements

I would like to thank the present and past members of the radiative capture group at TUNL – Mark Balbes, Bob Chasteler, Jerry Feldman, Mark Godwin, Greg Schmid, and Zandy Williams – who have given many hours of their time to build my experimental setups and assist in my data taking. I have been fortunate to have had Mark, Jerry, and Zandy around for most of my graduate student career. We solved many problems together and I owe them extra thanks. I would like to thank Ron Tilley for his assistance and valuable discussions. I would also like to thank Evans Hayward for her friendship and support over the past few years. Lastly, I would like to thank Henry Weller whose support, encouragement, and friendship have taught me a great deal about physics. I shall value this knowledge forever.

I am grateful to TUNL and the Department of Energy for their financial support over the past 5 years. I have also been fortunate to have had strong technical support from Paul Carter, Sidney Edwards, Al Lovette, and the whole instrument shop. The instrument shop went the extra mile to construct the NaI-recoil detector setup and I am indebted for their help.

I would like to thank my family, especially my parents Marie and Huck, for providing a supportive environment in which to learn. I certainly would not have reached this point without their encouragement over these many years.

I owe a great debt of gratitude to Patty Atkinson whose love and support have made my research worthwhile.

Table of Contents

Figures

Tables

CHAPTER 1

Introduction

Evidence for a tensor force in the two-nucleon system was first demonstrated by Schwinger in 1939 [Sch39]. He realized that the deuteron's finite electric quadrupole moment meant that the deuteron is not spherically symmetric as required by a central force. Therefore the deuteron must have a D-state admixture in the ground state wave function, in order to create a prolate system. The deuteron wave function is now known to be predominantly a symmetric S-state with a 4 - 7% D-state admixture. Early phenomenological analysis of the deuteron showed that the tensor force was crucial, accounting for 70% of the binding interaction, despite the small D-state admixture [Bet40] [Rar41]. The tensor force was later found to be important in the A = 3 and 4 systems, where variational method calculations showed that it accounted for 50% and 40% of the binding interaction, respectively [Ger41].

The two-nucleon tensor force operator can be written in the form

$$S_{1\,2} = (\vec{\sigma}_1 \cdot \vec{r})\,(\vec{\sigma}_2 \cdot \vec{r}) - \vec{\sigma}_1 \cdot \vec{\sigma}_2, \qquad (1.1)$$

where $\vec{\sigma}_1$ and $\vec{\sigma}_2$ are the spin operators for the two nuclei and $\vec{r}$ is the distance between the two nucleons. In the deuteron and other systems, the D-state admixture is related to the strength of the tensor force. Unfortunately, the D-state probability is not a true

observable, it requires knowledge of the complete wave function [Fri79]. It can only be inferred from measured quantities and calculations. In the case of the deuteron, the finite quadrupole moment is a signature of the presence of the D-state and tensor force. In the A = 3 and 4 systems, there is no quadrupole moment, so other observables are used to probe the D-state. These include the asymptotic D-to-S state ratio, the tensor analyzing powers, and the electromagnetic quadrupole form factor.

The measurement of non-zero tensor analyzing powers in the $^2H(\vec{d},\gamma)^4He$ reaction has established the existence of a D-state in ^4He [Wel84]. Subsequent studies of the $^2H(d,\gamma)^4He$ reaction have broadened the knowledge of the ^4He D-state. Above $E_d(lab)$ = 3 MeV, the reaction is dominated by E2 d-wave capture to the ^4He S-state with an admixture of E2 s-wave capture to the ^4He D-state. It is expected that the low energy cross section, where the centrifugal barrier should suppress the E2 d-wave capture, should be especially sensitive to the ^4He D-state. Several studies of the $^2H(d,\gamma)^4He$ cross section below $E_d(lab)$ = 500 keV [Wil85], [Bar87] found an enhancement in the low energy cross section over earlier predictions [Fow84]. This enhancement was attributed to E2 s-wave capture to the D-state. Direct capture calculations were performed to extract the D-state admixture from the data, resulting in estimates of 4 - 7% [Wel86], [Ass87], [Pie87]. However, these conclusions were based on the assumption that the reaction proceeded mainly via E2 s-wave capture to the D-state of ^4He, and thus do not rule out the existence of other multipoles.

One motivations of the present work has been to attempt to extract information about the $^2H(d,\gamma)^4He$ reaction mechanism at very low energies. A full understanding of this mechanism is necessary to allow for an accurate extrapolation of the cross section to energies appropriate to nuclear astrophysics. Radiative capture reactions play an important role in the formation of the various elements in the universe and are thus

important to nuclear astrophysics. Extrapolation of the low energy capture cross sections to astrophysical energies (the center of the sun is about 10^7K or about 1 keV) is, in general, the only method available to gain insight in the astrophysical energy region of nuclear reactions. The ^{2}H(d,γ)^{4}He reaction is involved in both primordial (big bang) and stellar nucleosynthesis. While the total low energy cross section has been established for this reaction, the reaction mechanism has not been studied directly in the low energy region. This study seeks to understand the low energy reaction mechanism.

Another goal of this work has been to obtain detailed knowledge about the transition matrix elements in this low energy region where D-state effects of ^{4}He are expected to play a major role. The hope is that these matrix elements could then be compared to theoretical predictions and allow a more accurate extraction of the ^{4}He D-state probability. Previous investigations have only measured values for the total and differential cross sections. Since cross sections are the sum of transition matrix elements squared, information about individual transition matrix elements cannot be extracted. Also the symmetry of the reaction (guaranteed by the identical particles in the entrance channel) removes effects of interfering odd parity states in the differential cross section. However, since polarization observables arise from the interference of various transition matrix elements, polarization data can provide information about the transitions and multipolarities involved in the reaction. In this work, we have measured polarization observables with this purpose in mind.

In the d-d cluster model representation of the ^{4}He ground state, two deuterons are coupled to channel spin **S** and orbital angular momentum **L**. The ^{4}He ground state is composed of two components – $^1S_0$ and $^5D_0$. (We use the notation $^{2S+1}L_J$ to identify the ground state configuration.) The ground state is then taken to be an admixture of these two states. Since there are identical bosons in the entrance channel, symmetry

requirements demand that for the orbital angular momentum ℓ and total entrance channel spin **S**, the quantity ℓ + **S** must be even for the scattering state. This requirement forbids $\Delta S = 0$ E1 radiation, since ℓ must be 1 in the incident channel to form a 1^- state. Only $\Delta S = 1$ E1 transitions are allowed. However, $\Delta S = 0$ E2 transitions are allowed, and are expected to dominate. The allowed E2 transitions are then $^1d_2$-wave capture to the $^1S_0$ state and $^5s_2$-, $^5d_2$-, and $^5g_2$-wave capture to the $^5D_0$ state. (We use the notation $^{2S+1}\ell_J$ to identify the scattering state configuration.)

The polarization observables for the $^2H(d,\gamma)^4He$ reaction at E_d(lab) = 10 MeV showed sensitivity to the ^{4}He D-state component [Wel84]. Later measurements improved upon the data set in the region E_d(lab) = 0.8 - 50 MeV [Wel86], [Mel86a], [Mel86b], [Lan88], [Wel88], [Lan90]. These results indicated that the reaction is dominated by E2 radiation, most of which is due to $^1d_2$-wave capture to the $^1S_0$ state. However, the reaction was also found to include E1 and M2 radiative transitions, although these transitions only accounted for 10 - 15% of the strength [Mel86a], [Lan88], [Lan90].

As previously noted, the cross section measurements were extended to lower energies, where the centrifugal barrier should suppress the E2 $^1d_2$-wave capture to the $^1S_0$ state and thus allow the E2 $^5s_2$-wave capture to become dominant. Wilkinson and Cecil [Wil85] first measured the Γ_γ/Γ_p branching ratio in the energy region E_d(lab) = 50 - 150 keV, which, combined with the $^2H(d,p)^3He$ cross sections of [Bro90], showed an enhancement in the cross section over the previous estimates [Fow84]. Later, Barnes *et al.* [Bar87] measured the total and differential cross section in the energy region E_d(lab) = 100 - 1000 keV. The differential cross section at E_d(lab) = 150 keV was found to be isotropic (to within 20%) and the total cross section agreed with the earlier measurements, supporting the prediction of dominant E2 s-wave capture to the ^{4}He D-state. The data for the total cross section are shown in Figure 1.1.

To interpret these low energy results, several direct capture calculations were carried out [Wel86], [Ass87], [Blü87], [Pie87]. The calculations supported the interpretation that the reaction is dominated by E2 $^5s_2$-wave capture to the $^5D_0$ state in the low energy region. This is illustrated in Figure 1.1, where the result of a direct capture calculation is shown along with the experimental data. Note that the d-wave capture decreases rapidly at lower energies while s-wave capture dominates below E_d(lab) = 500 keV. These calculations were also used to extract information about the ^{4}He D-state, leading to estimates of a D-state probability in the ^{4}He ground state of 4 - 7%, where this represents the d-d part of the ^{4}He D-state probability. It must be emphasized that conclusions drawn from the direct capture calculations have been based on the *assumption* of dominant E2 radiation, although there has been no direct evidence for this behavior.

We have measured the vector and tensor analyzing powers of the $^2H(\vec{d},\gamma)^4He$ reaction using an 80 keV beam of polarized deuterons. Analyzing powers arise from the interference of various transition matrix elements (TME's); they provide a means of determining which transitions and multipoles are involved in the reaction and can give values for the amplitudes and phases of various TME's. If the reaction proceeds purely via E2 s-wave capture to the $^5D_0$-state, then the cross section and analyzing powers A_y and A_{yy} must be isotropic, where $A_y(\theta) = 0.00$ and $A_{yy}(\theta) = 0.25$. If this is not the case, then the most likely contaminant would be expected to be due to p-wave capture, which could result form the $^3p_1$ (ΔS = 1 E1) and $^3p_2$ (M2) transitions. We will present results for $A_y(\theta)$, $A_{yy}(\theta)$, and $\sigma(\theta)/A_0$ for E_d(lab) = 80 - 0 keV at $\theta_{c.m.} = 0°$, 45°, and 82°. To examine which transitions are involved in the reaction, we have performed a model independent transition matrix element analysis [Sey79]. We compare the results to a recent microscopic coupled-channel resonating group model (MCCRGM) calculation

which includes E2, E1, M2, and M1 transitions and the coupled d-d, p-^{3}H, and n-^{3}He channels. This model has been shown to agree well with previous measurements at somewhat higher (~1.2 MeV) energies [Lan88], [Lan90]. Our results indicate that over 50% of the cross section is due to E1 and M2 p-wave capture. In comparing our results to a MCCRGM calculation, we find fair agreement when a semi-realistic potential which includes a 2.2% D-state probability is utilized. Note that this D-state is the D-state associated with the L = 2 relative motion between two S-state deuterons.

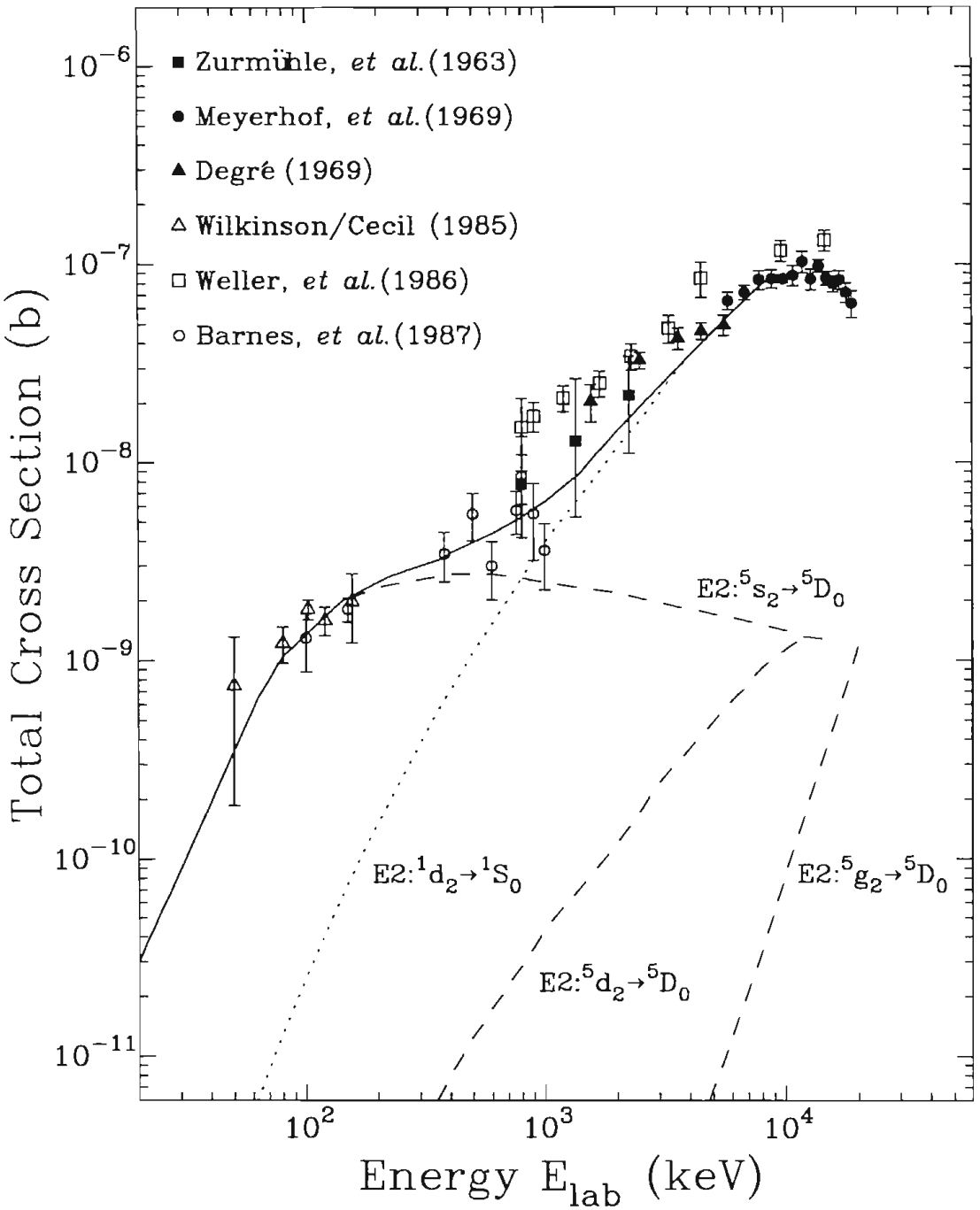

FIG. 1.1 Total cross section as a function of energy for the $^2H(d,\gamma)^4He$ reaction. Also included are results from a direct capture calculation, with contributions from the different transitions shown. Data and calculation are from [Bar87].

CHAPTER 2

Experimental Equipment and Procedures

2.1 Introduction

Development of this experiment began in October 1990 during the tandem upgrade project at TUNL. The upgrade allowed us plenty of beam time to determine the best experimental methods to employ in the project. The greatest problem was designing a system to measure the very low cross section of the $^2H(d,\gamma)^4He$ reaction (~80 pb/sr at 80 keV). To overcome this problem, maximum beam current was used, the γ-ray detector was placed as close to the target as possible, and the background was reduced through shielding and electronic rejection. However, even by utilizing these methods, the count rate was only 5 - 10 counts/hour. To achieve reasonable statistical errors (~ $\pm$0.10 for the analyzing powers), each run measured a single angle and lasted eight days.

One of the major factors that made this experiment possible was the new intense polarized-ion source at TUNL. In the low energy capture beam line the source is capable of producing up to 50 μA of 85% polarized deuterons at 80 keV. The experiment was performed as close to the source as possible to take advantage of the maximum current

from the source. In minimizing the distance to target, we omitted focusing elements in the capture beam line. Good quality beam tunes were achieved without the focusing elements, leading us to conclude that they were unnecessary.

The physical layout of the experiment is shown in Figure 2.1.1. Beam from the polarized source passed through a Wien filter and was then deflected by an inflection magnet into the 60° low energy capture beam line (LECL). On exiting the inflection magnet, the beam passed through a set of x-y collimation slits and onto a Deuterated-Titanium target. A collimated solid-state detector was placed upstream of the target to monitor the target thickness. To insure accurate beam current integration, charge from the beam line components following the beam collimation slits was collected. Also, the target and collimator slits were biased at 90 volts to suppress secondary-electron emission. Details of the beam collimation and integration along with the solid-state monitor collimation are shown in Figure 2.1.2. Typical experimental parameters were 35 - 40 μA on target with 3 - 4 μA on the collimator slits. The capture γ rays were observed with an anti-coincidence shielded NaI(Tl) detector system. The following sections detail the individual components of the experimental setup.

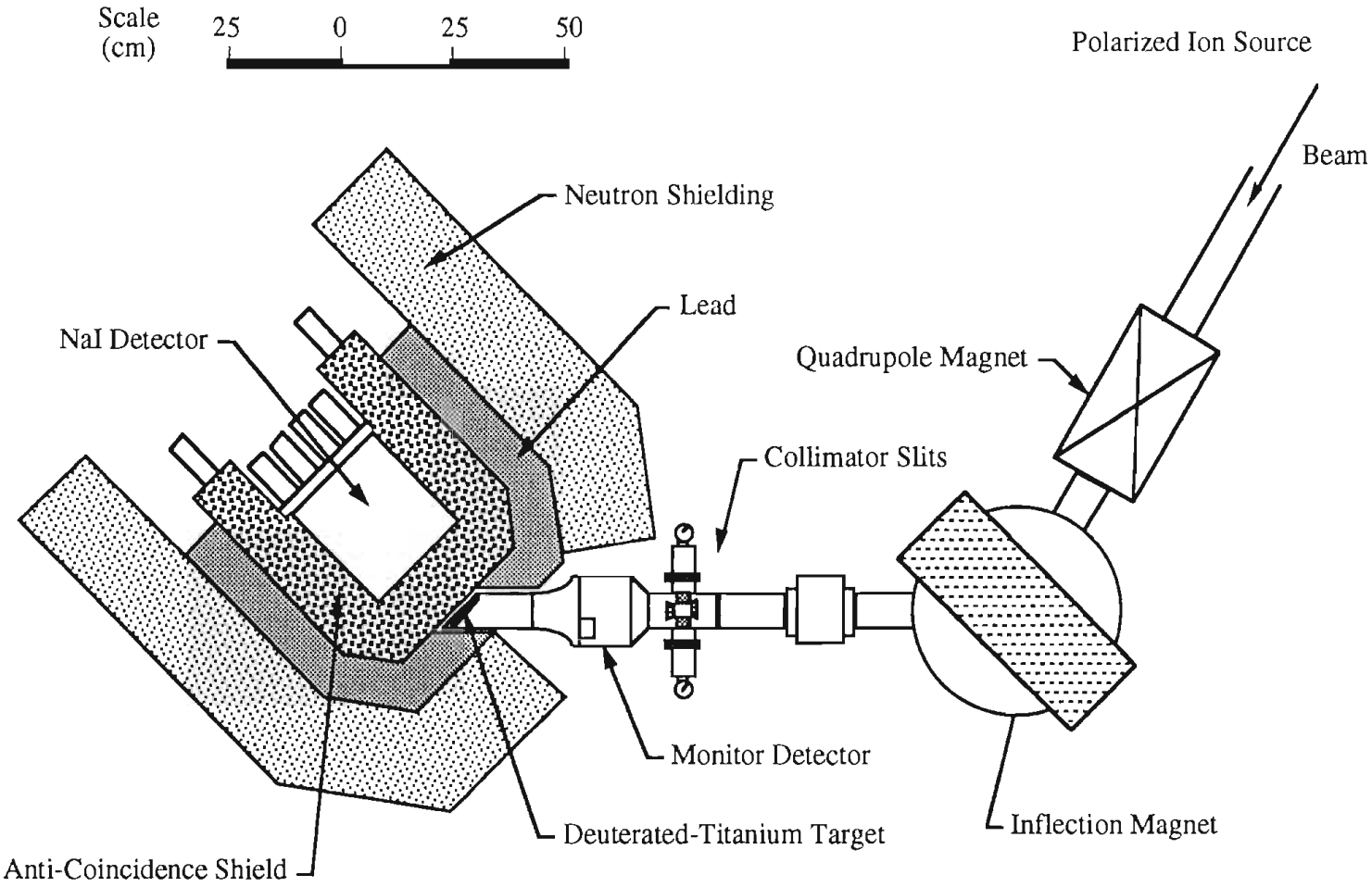

FIG. 2.1.1 Experimental setup used in the $^2H(\vec{d},\gamma)^4He$ measurement. Beam was deflected by the inflection magnet, passed through the collimator slits, and impinged upon the target. The capture γ-rays were detected in the NaI spectrometer. The monitor detector detected protons from the $^2H(d,p)^3He$ reaction for normalization purposes.

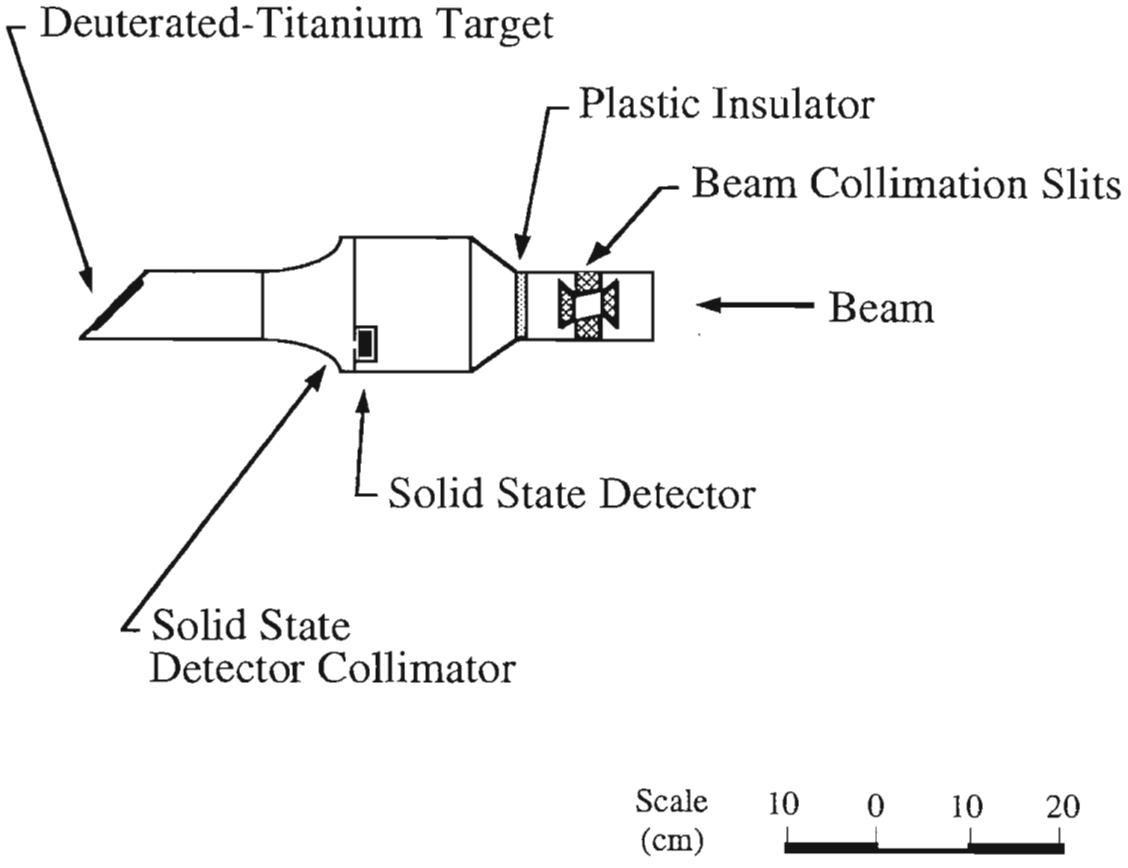

FIG. 2.1.2 Target assembly used in the $^2H(\vec{d},\gamma)^4He$ measurement. Beam entered from the right and was collimated by the x-y slits. Current was collected from elements downstream of the plastic insulator. The solid-state detector was placed at an angle of 173° with respect to the beam and collimated to 140 μsr.

2.2 Target

Due to target loading capabilities of titanium, Deuterated-Titanium targets were chosen for use in this experiment. Deuterium to titanium ratios as high as 1.75 have been observed in titanium [Dus62]. A commercially manufactured target, an Amersham model DBT-12, was used in the capture beam line. This target consisted of titanium evaporated on copper which was then deuterated. In the polarimeter beam line, we produced and used "homemade" Deuterated-Titanium foils.

The "homemade" Deuterated-Titanium foils were made by heating titanium foils in a deuterium atmosphere. The process began by placing titanium foil (5.08μm thick) in an evaporator between the two high current electrodes of the evaporator, and evacuating the chamber. Next, the foil was slowly heated by passing current through it to remove impurities, possibly including water, deuterium, and hydrogen. A high vacuum gauge monitored outgassing while the heating took place. Heating was stopped when increases in current (temperature) produced no change in pressure. The system was purged several times with high purity (99.8%) deuterium gas, which was passed through a liquid nitrogen filled cold trap. The chamber was then let up to approximately 150 mbar of deuterium and the foil was slowly heated to just below glowing (500 - 600°C). At this temperature the solubility of deuterium in titanium is maximum [Dus62]. Evidence of deuterium loading was obvious, as the target wrinkled when heated. Experience showed that overheating of the foils, especially in initial outgassing, produced brittle targets; therefore, care was taken to minimize foil heating.

One complication encountered was that the target thickness changed due to beam implantation. This can be understood as the combination of two effects. First, beam

deuterons stopping in the target became part of the target. For higher beam currents, more deuterons became part of the target per unit time. Second, the beam heated the target, causing target deuterons to boil off. More heat is produced with higher beam current, removing more deuterons from the target. The combination of these two effects created an equilibrium situation, where different target thickness equilibriums were created at different beam currents. An upstream solid-state detector monitored this effect through the $^{2}H(d,p)^{3}H$ reaction.

The solid-state detector monitor was positioned at 173° with respect to the beam and subtended a solid angle of ~140 μsr, see Figure 2.1.2. A thin Mylar foil (6.35 μm) was placed in front of the detector to stop scattered electrons and deuterons. At 173° the $^{2}H(d,p)^{3}H$ reaction produces 2.714 MeV protons and 0.703 MeV tritons from 80 keV deuterons. ^{3}He particles were also created through the $^{2}H(d,n)^{3}He$ reaction, but were stopped in the Mylar foil. The pulse height distributions produced by the protons and tritons were background-free and clearly separated, providing an excellent measure of the target thickness. A sample spectrum is shown in Figure 2.2.1. We found that higher beam currents produced thicker targets. This is illustrated in Figure 2.2.2, where data for relative target thickness are plotted as a function of average beam current for various runs. The data are the result of an eight-day run during which the beam current fluctuated between 21 and 41 μA. The trend toward greater target thicknesses for higher beam currents is apparent in the figure. We also found that the target thickness would reach equilibrium after a constant beam current was applied for several hours. This is shown in Figure 2.2.3, where data for the relative target thickness are plotted as a function of time for runs of nearly equal beam current (between 29.5 and 33.5 μA). As can be seen, the target thickness plateaus after about fifty hours.

The target was mounted on the end of the beam line in one of two configurations, depending on the NaI detector's position. For the $\theta = 45°$ and 82° measurements, a brass end piece was used, where the target was placed on an aluminum target holder which was mounted at an angle of 45° with respect to the beam direction. For the $\theta = 0°$ measurement, the target was mounted in an aluminum end cap, where the target was at an angle of 90° with respect to the beam direction. Use of these different end pieces was necessary to minimize the distance between the target and the NaI detector assembly. The two different target assemblies are shown in Figures 2.2.4 and 2.2.5.

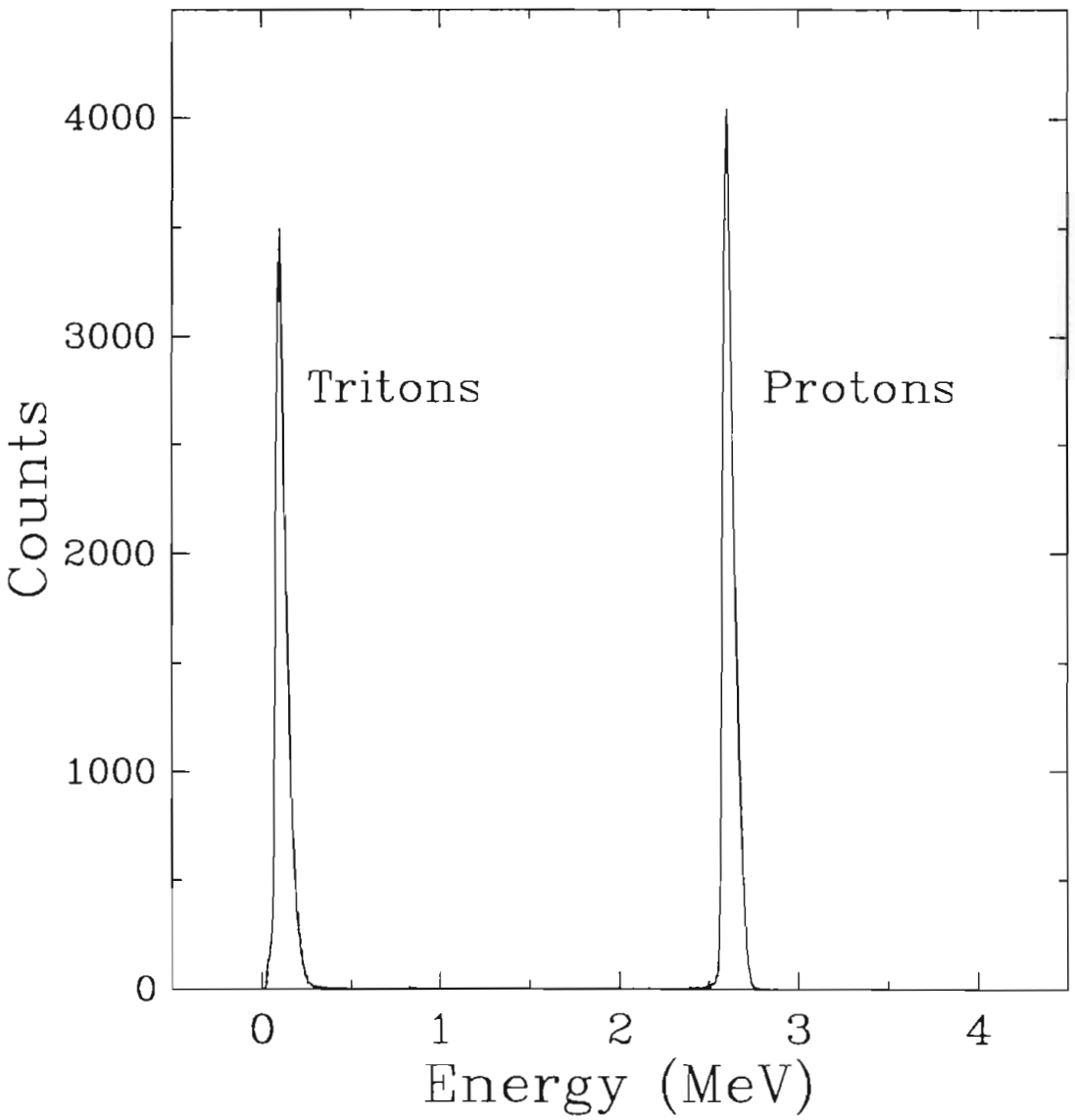

FIG. 2.2.1 Sample spectrum for the solid-state monitor detector. The monitor detector was positioned at 173° with respect to the beam, and detected protons and associated tritons from the $^{2}H(d,p)^{3}H$ reaction. The proton peak is clearly separated from the triton peak in the spectrum.

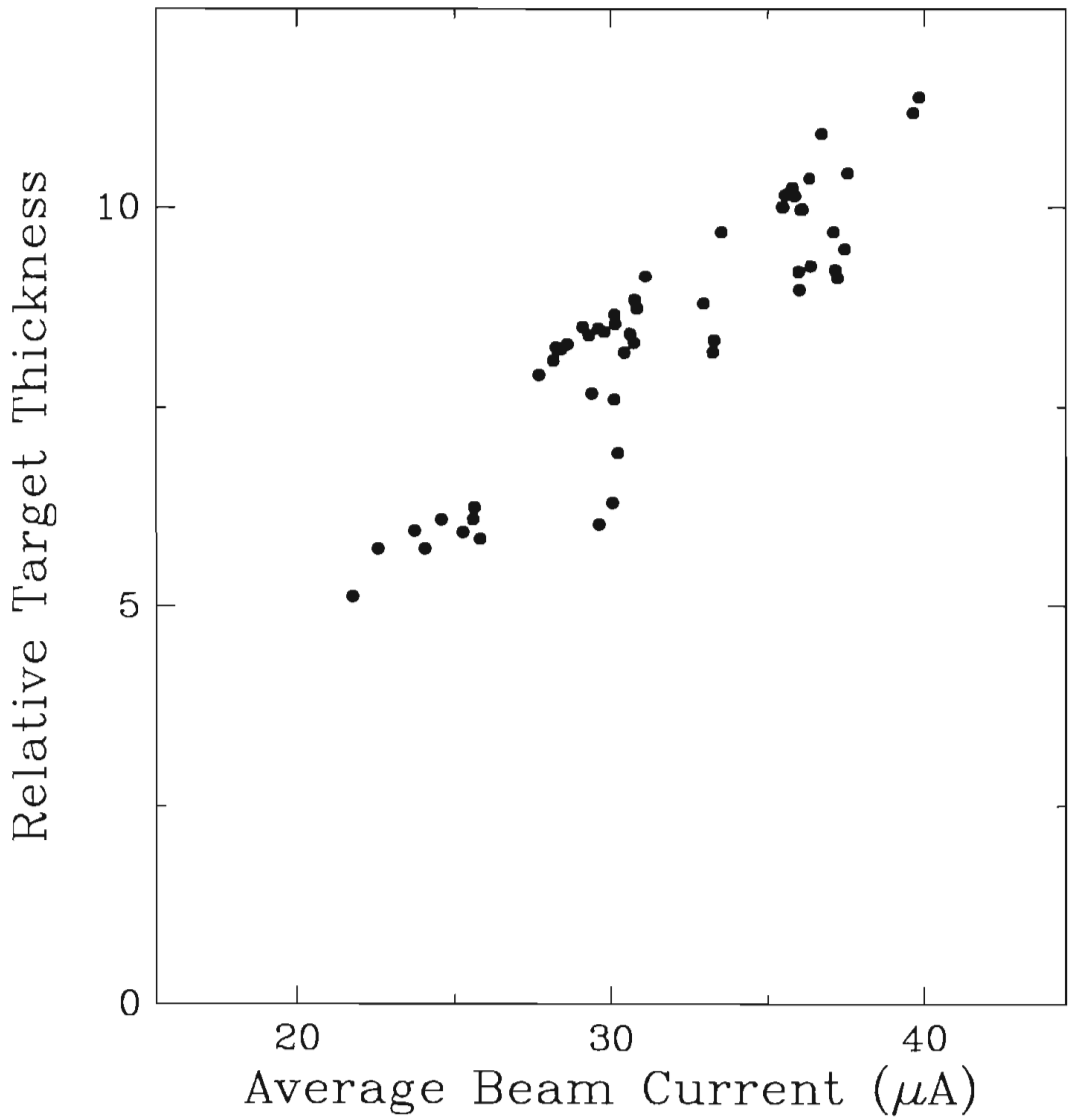

FIG. 2.2.2 Relative thickness of the Deuterated-Titanium target plotted as a function of average beam current for various runs. The trend toward greater target thicknesses for higher beam currents is apparent in the figure.

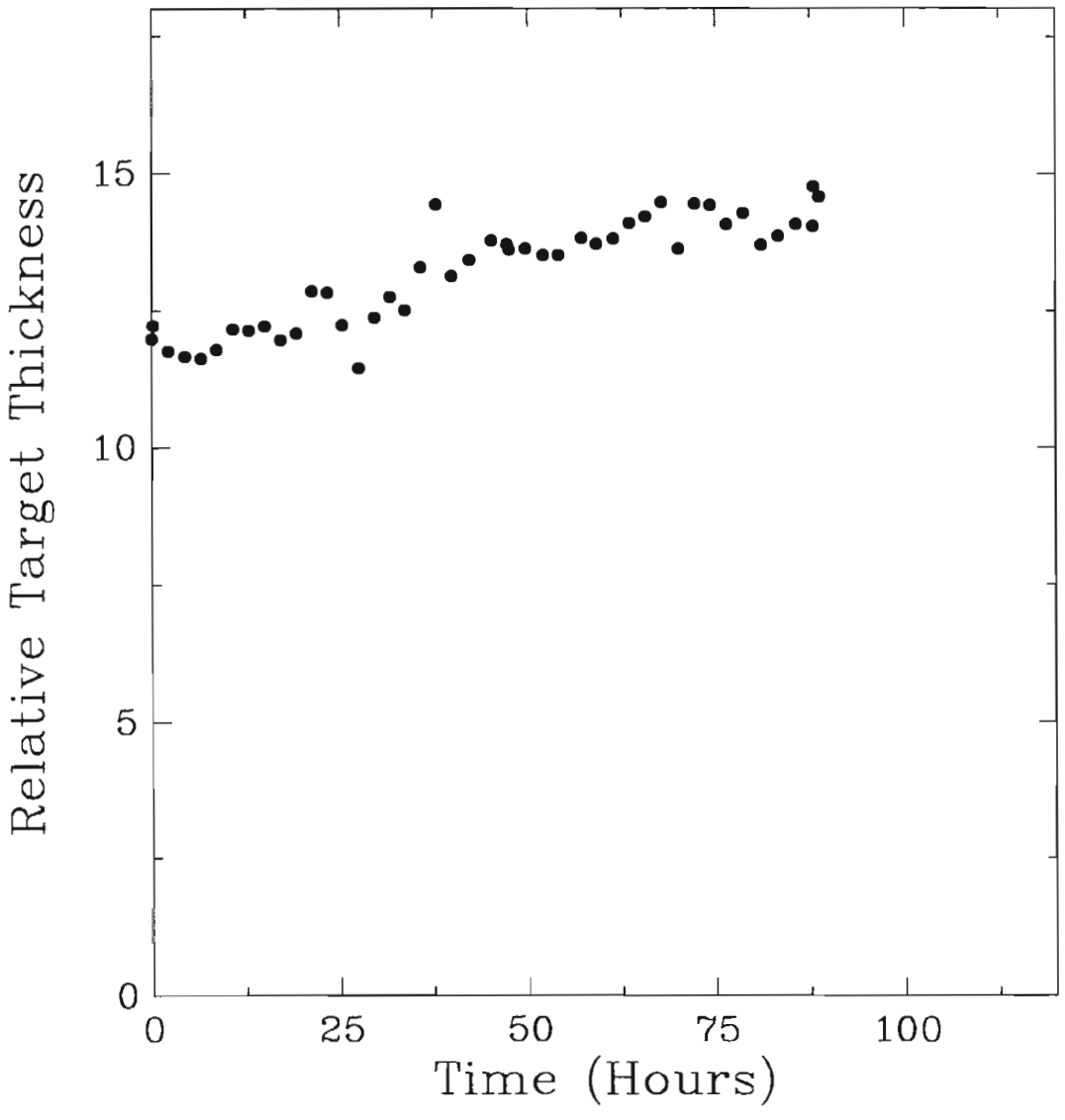

FIG. 2.2.3 Relative thickness of the Deuterated-Titanium target plotted as a function of time, where the beam current was nearly constant. The beam current remained between 29.5 and 33.5 μA. As can be seen, the target thickness reaches equilibrium after about fifty hours.

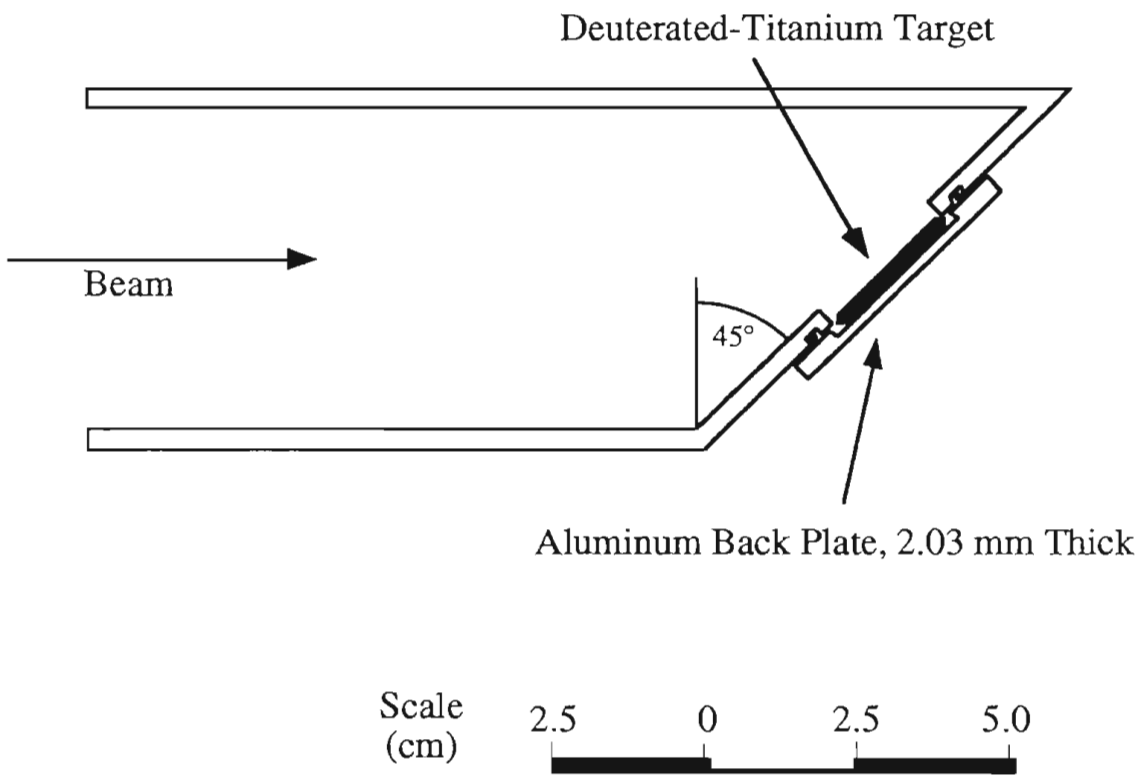

FIG. 2.2.4 Target assembly used in the $\theta = 45°$ and $\theta = 82°$ measurements. The detector assembly was positioned 0.32 cm and 2.22 cm from the back plate of the target in the $\theta = 45°$ and $\theta = 82°$ measurements, respectively.

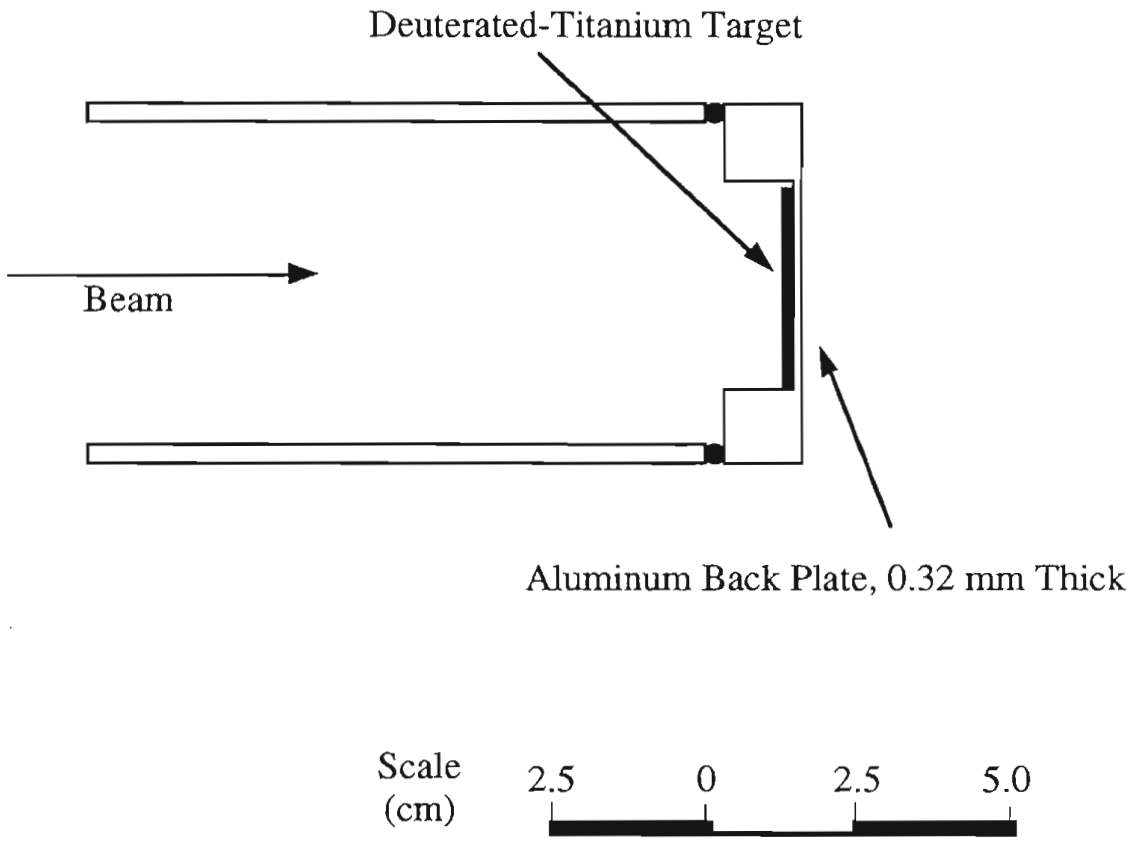

FIG. 2.2.5 Target assembly used in the $\theta = 0°$ measurement. The detector assembly was positioned 0.32 cm from the back plate of the target.

2.3 Polarized Ion Source

The polarized beam was produced by the new TUNL atomic beam polarized-ion source. A schematic diagram of the source is shown in Figure 2.3.1. In the source, deuterium gas is dissociated by a radio-frequency plasma. The atomic beam then diffuses into a high vacuum chamber through a cryogenically cooled nozzle at ~35 K. The cold nozzle prevents recombination of the atoms into molecules. High purity nitrogen gas is bled into the dissociator with the deuterium to coat the cold nozzle, also preventing recombination. A downstream skimmer is used to collimate the atomic beam, preventing background molecules from continuing into the rest of the source.

The beam now enters the region of the source where it is polarized. The aim is to rearrange the population of the various deuteron substates to create the desired polarization state. The energy level diagram of deuterium is shown in Figure 2.3.2. The atomic beam first enters a sextupole magnet where magnetic substates $m_j = -1/2$ (the lower three states in Figure 2.3.2) are swept out of the beam, leaving the atoms in the $m_j = +1/2$ state (upper three states in Figure 2.3.2). At this point, the atoms have their electron spins aligned. The beam then enters a strong field rf transition unit, where transitions are made between states of opposite m_j. In this experiment, both the $3 \leftrightarrow 5$ and $2 \leftrightarrow 6$ transitions were utilized. It should be noted that the source has two sextupole magnets each followed by two rf transition units. Different combinations of transitions provide different polarization configurations where the measurement determines which transitions are to be utilized.

Once the beam is polarized, it is ionized and extracted from the source. Ionization is accomplished in the electron-cyclotron-resonance (ECR) ionizer. Here a plasma is

created by introducing a buffer gas (high purity nitrogen) into the ECR region and applying rf. The plasma is localized by three magnetic lenses located outside the source. The neutral atomic beam enters the plasma region where it is stripped of its electrons by electron-impact ionization. Positive beam is then extracted by a negatively biased plate. A series of six electrostatic lenses follows the extraction plate, which focuses the beam. The source is raised to a positive potential with respect to ground, 80 kV in this experiment, which accelerates the beam out of the source.

In order to measure the analyzing powers $A_y(\theta)$ and $A_{yy}(\theta)$, the deuteron quantization axis must be aligned at $\beta = 90°$ and $\phi = 0°$, where β and ϕ are defined following the Madison Convention (Section 4.2). The beam emerging from the source has its quantization axis aligned at $\beta = 0°$ and $\phi = 0°$. A Wien filter located after the source precesses the quantization axis to the desired position. The Wien filter is simply a device with crossed electric and magnetic fields. The magnetic field precesses the spin while the electric field compensates for the deflection of the beam due to the magnetic field. It is located after the extraction lens and is raised to 5/8 of the source potential. The TUNL program PRECESS calculates the magnetic field necessary for a particular spin alignment at the target position.

A new procedure of maximizing beam polarization was recently developed at TUNL [Cro91]. Maximizing beam polarization involves tuning the rf transition unit's magnetic field to the resonant value. The transition unit is very sensitive to stray magnetic fields, so the resonant value is difficult to reproduce. Previously, the beam was sent into a polarimeter, and the polarization as a function of magnetic field was mapped out. However, this method proved tedious, generally taking several hours to complete. The new method utilizes the spin-spin dependence of the cross section for electron-impact ionization; therefore, the amount of beam extracted depends on the electron spin.

By pulsing the transition unit rf and measuring the difference in the polarized and unpolarized beam currents as a function of magnetic field, the polarization was maximized. The maximum difference corresponded to maximum polarization. The process was complicated by the fact that the polarized/unpolarized current differences were very small (~0.08% of the total beam). This problem was solved by employing a lock-in amplifier to measure the differences. Using this method polarization could easily be maximized in less than 1/2 hour. This was especially helpful since the polarization state was changed every few days during the experiment. Typical operating parameters were 35 - 40 μA of ~85% polarized beam on target.

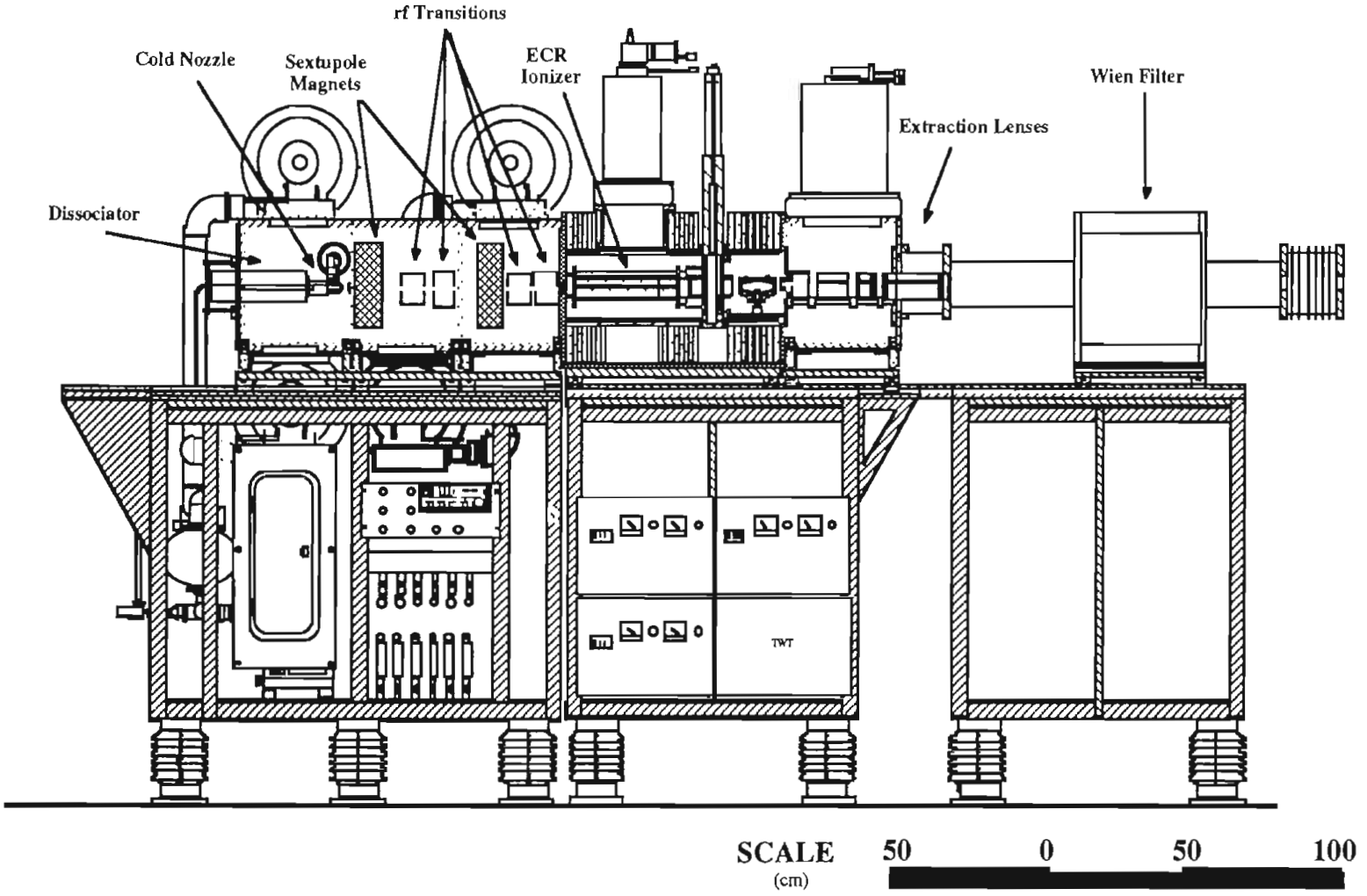

FIG. 2.3.1 Schematic drawing of the atomic beam polarized-ion source. Beam is created on the left side of the figure in the dissociator, passes through the transition and ionizer regions, and exits through the Wien filter on the right.

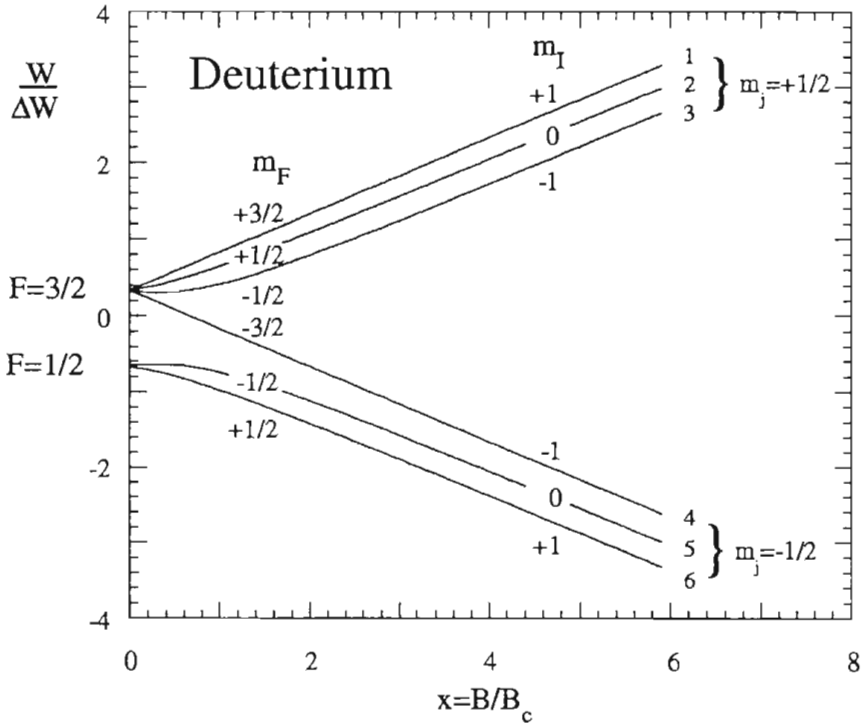

FIG. 2.3.2 Energy-level diagram of the deuterium atom in a magnetic field B. For the ground state B_c = 117 G, for the $^2S_{1/2}$ excited state B_c = 14.6 G.

2.4 Polarimetry

The beam polarization was measured by deflecting the beam into a second beam line which contained a $^2H(\vec{d},p)^3H$ polarimeter. The polarimeter consisted of a "homemade" Deuterated-Titanium target viewed by two solid-state detectors placed inside a scattering chamber. The target was thick enough to stop the beam; therefore, the beam energy extended from 80 - 0 keV. The solid-state detectors were positioned at 110° with respect to the beam direction.

Since the analyzing powers of the $^2H(\vec{d},p)^3H$ reaction are not known in our energy region, the low energy polarimeter had to be calibrated. This was accomplished by using our standard high energy polarimeter, utilizing the $^3H(\vec{d},p)^4He$ reaction. Direct calibration of the low energy polarimeter was especially useful since the beam stopped in the target, and a calibration for the $E_d(lab)$ = 80 - 0 keV integrated beam was established directly. The high energy polarimeter was calibrated for 5 - 12 MeV deuterons, so it was necessary to send the polarized beam through the tandem accelerator and into the polarimeter. The polarization of 5 MeV deuterons in the high energy polarimeter was first maximized. A series of short polarization runs were taken to insure consistency of the polarization. Next, the beam was deflected into the low energy polarimeter line where the analyzing powers of the $^2H(\vec{d},p)^3H$ reaction were measured. Again, a series of runs were taken to insure consistency of the measurement, and the average was taken as the analyzing powers. Results for the vector and tensor analyzing powers of 80 - 0 keV deuterons in the low energy polarimeter were found to be $A_y(110°) = 0.193 \pm 0.022$ and $A_{yy}(110°) = 0.296 \pm 0.022$, where the error bars indicate the statistical uncertainty in the data.

As with the Deuterated-Titanium target used in the capture measurements, the polarimeter targets would sometimes change thicknesses over time, resulting in erroneous polarization results. This problem occurred mostly with new targets; after targets had been exposed to beam for a period of time, this effect became negligible. To eliminate this problem a break-in period for new targets was established. New targets were exposed to a current of 3 - 4 μA and monitored for target thickness changes as a function of time until an equilibrium thickness was established. In subsequent measurements targets were exposed to similar currents. Polarization runs were broken up into a series of short runs to allow for monitoring of the target thickness, and only runs with consistent unpolarized sums were used in the measurement. These techniques effectively eliminated effects due to changing target thickness.

The vector and tensor beam moments, p_z and p_{zz}, for the low energy polarimeter with a left-right pair of detectors are given by

$$p_z = \frac{1}{3A_y(\theta)}\left(\frac{Y_{LP}(\theta)}{Y_{L0}(\theta)} - \frac{Y_{RP}(\theta)}{Y_{R0}(\theta)}\right), \tag{2.4.1}$$

$$p_{zz} = \frac{1}{A_{yy}(\theta)}\left(\frac{Y_{LP}(\theta)}{Y_{L0}(\theta)} + \frac{Y_{RP}(\theta)}{Y_{R0}(\theta)} - 2\right), \tag{2.4.2}$$

where θ is the detector angles, $A_y(\theta)$ and $A_{yy}(\theta)$ are the vector and tensor analyzing powers, $Y_{LP}(\theta)$, Y_{L0},(θ) $Y_{RP}(\theta)$, $Y_{R0}(\theta)$ are the polarized and unpolarized yields for the left and right detectors. The errors for the beam moments are given by

$$\Delta p_z = \sqrt{\left(\frac{1}{3A_y(\theta)}\right)^2 D(Y(\theta))}\,, \tag{2.4.3}$$

$$\Delta p_{zz} = \sqrt{\left(\frac{1}{A_{yy}(\theta)}\right)^2 D(Y(\theta))}\,, \tag{2.4.4}$$

$$D(Y(\theta)) = \left(\frac{1}{Y_{L0}(\theta)}\right)^2 (\Delta Y_{LP}(\theta))^2 + \left(\frac{Y_{LP}(\theta)}{Y_{L0}(\theta)^2}\right)^2 (\Delta Y_{L0}(\theta))^2$$

$$+\left(\frac{1}{Y_{R0}(\theta)}\right)^2 (\Delta Y_{RP}(\theta))^2 + \left(\frac{Y_{RP}(\theta)}{Y_{R0}(\theta)^2}\right)^2 (\Delta Y_{R0}(\theta))^2, \quad (2.4.5)$$

where ΔY_i are the errors in the yields given by:

$$\Delta Y_i(\theta) = \sqrt{Y_i(\theta)}. \quad (2.4.6)$$

The polarization was measured at the beginning of each set of runs for a spin state and rechecked every 24 - 48 hours. The polarization was found to be constant over time to within 10% for p_z and 5% for p_{zz}. Typical polarizations were $p_z = 0.290$ and $p_{zz} = 0.861$.

2.5 NaI Spectrometer

The capture γ rays were detected in an anti-coincidence shielded NaI spectrometer. At the center of the spectrometer was a Bicron 25.4 cm $\times$ 25.4 cm NaI(Tl) detector, viewed by 7 HPK R-1911 photomultiplier tubes with high-current transistorized bases. The NaI(Tl) detector was placed inside a 10.16 cm thick Bicron BC412 plastic anti-coincidence shield. The shield was viewed by 8 Amperex PM2312 photomultiplier tubes with high-current transistorized bases. The shield was used to discriminate against unwanted events – those due to cosmic rays, neutrons, and events which did not deposit their full γ-ray energy in the NaI(Tl) detector.

Due to the low count rate, much attention was placed upon reducing background in the NaI spectrometer. First, passive shielding was used to reduce sources of unwanted radiation before getting into the spectrometer. The detector assembly was shielded with lead, 10.16 cm on sides, 15.24 cm on top, and 5.08 cm on bottom, to reduce the γ-ray background, including cosmic rays. Additional shielding, including paraffin, lithium carbonate, and borated polyethylene, was stacked around the assembly to reduce neutron background. An 0.08 cm thick cadmium sheet was placed on the front face of the anti-coincidence shield to reduce thermal neutron background through neutron capture. Second, electronic circuitry eliminated background through active rejection. The cosmic-ray rejection circuit was carefully adjusted to achieve 99.8% rejection. Also, a pulse shape discrimination circuit was added to reduce neutron induced events.

Neutrons and γ rays interact differently in NaI, creating an opportunity to discriminate against one form of radiation. In NaI, neutrons interact and produce recoil protons and γ rays interact mainly through pair production (in the energy region of

interest) which creates recoil electrons. The slow component of the light pulses generated by the protons and electrons have different intensities. The current pulses from the photomultiplier tubes of the NaI, therefore, have different decay times for each particle. Pulse shape discrimination (PSD) techniques utilize this difference in decay times to discriminate against neutrons or γ rays. Several good references on PSD circuits are [Bir64], [Bas64], [Bar75], [Dol89], and [Whi86].

In this experiment, we modified the standard electronics circuit (Figure 2.5.1) to include a PSD circuit. Signals from the photomultiplier tubes (biased at negative high voltage) are summed and fed into a linear fan out. One output is then clipped to 400 ns by reflecting it down an almost shorted cable. It has been determined that clipping the signal has a negligible effect on the energy resolution. The clipped signal is then sent through a linear fan out which creates two branches, one branch handles the energy signal, while the other is used to create the necessary logic signals for the circuit.

The energy pulse is now prepared for processing by the computer. After the fan out, the pulse is sent through a bipolar amplifier, a 0.1μF capacitor (to remove DC offset), and then into a linear gate. The linear gate is opened only for signals that fire a discriminator in the logic branch of the circuit. After the linear gate is opened for 400 ns, it is closed for ~10 μs to allow for signal processing. This effectively eliminates pulse pile-up for any two signals arriving more than 400 ns apart. After passing through the gate, the energy signal is amplified by a spectroscopy amplifier and then linearly stretched to ~3 μs for input into the ADC.

On exiting the fan out, the logic pulse is sent through a bipolar amplifier, a timing filter amplifier, and into an EG&G TD101 discriminator. The timing filter amplifier produces 20 ns pulses so that two pulses separated by more than 20 ns will not fire the discriminator unless one of them exceeds the discriminator threshold. This eliminates

low-low pileup on the 20 ns time scale. The TD101 discriminator creates a logic output for signals above a given threshold, with timing based on a lower threshold set at a level corresponding to ~1 MeV γ rays. By timing on the lower threshold, time jitter is removed from the circuit. Also, one can vary the energy discriminator level (upper) without timing changes. This logic pulse is then used to trigger the linear gate and ADC, to increment the NaI scaler, and to check for coincidences between the NaI detector and the anti-coincidence shield. The shield is used to reject events which do not deposit all of their energy in the NaI detector and those due to cosmic rays. Signals from the shield are summed and sent through a fast discriminator. Logic signals from both the NaI (10 ns wide) and the shield (115 ns wide) are sent into a coincidence unit. The output is then sent to a router which is used to reject the event in software and to a scaler. The shield discriminator threshold is set to a level corresponding to ~1 MeV γ rays and is adjusted to achieve the desired amount of rejection. Lower thresholds achieve higher rejection but also reject some of the desired γ-ray peak. It should also be noted that in the experiment an extra long shield discriminator pulse (115 ns) was used, while normal operation utilizes a 50 ns long pulse. This was done to compensate for some time jitter in the circuit which could not be removed. Nonetheless, excellent cosmic-ray rejection (99.8%) was achieved. To estimate the accidental coincidence rate an accidentals circuit was also used. Coincidences between the NaI logic pulses and the shield logic pulses delayed by 300 ns were measured. The accidental rate is then the number of accidentals divided by the number of coincidences.

To create the PSD circuit the summed NaI energy signal was fanned out at the detector, creating 2 energy signals. One signal was clipped to 400 ns and sent through the standard electronics, while the second was used for the PSD circuit. The PSD circuit is shown in Figure 2.5.2. The PSD signal was sent into a double delay line amplifier

which integrated the signals, leading to signals with zero crossing depending on the decay time of the signal. The output was then sent into a single channel amplifier (SCA) operating in the zero crossing mode to create a logic signal based on the zero crossing time. To measure the decay time differences the SCA output was used to start a time amplitude converter (TAC), which was stopped by a fast output from the TD101 discriminator in the standard circuit. Output of the TAC was proportional to the decay time of the signal. Gating performed on the PSD-TAC spectrum resulted in approximately 30% reduction in background.

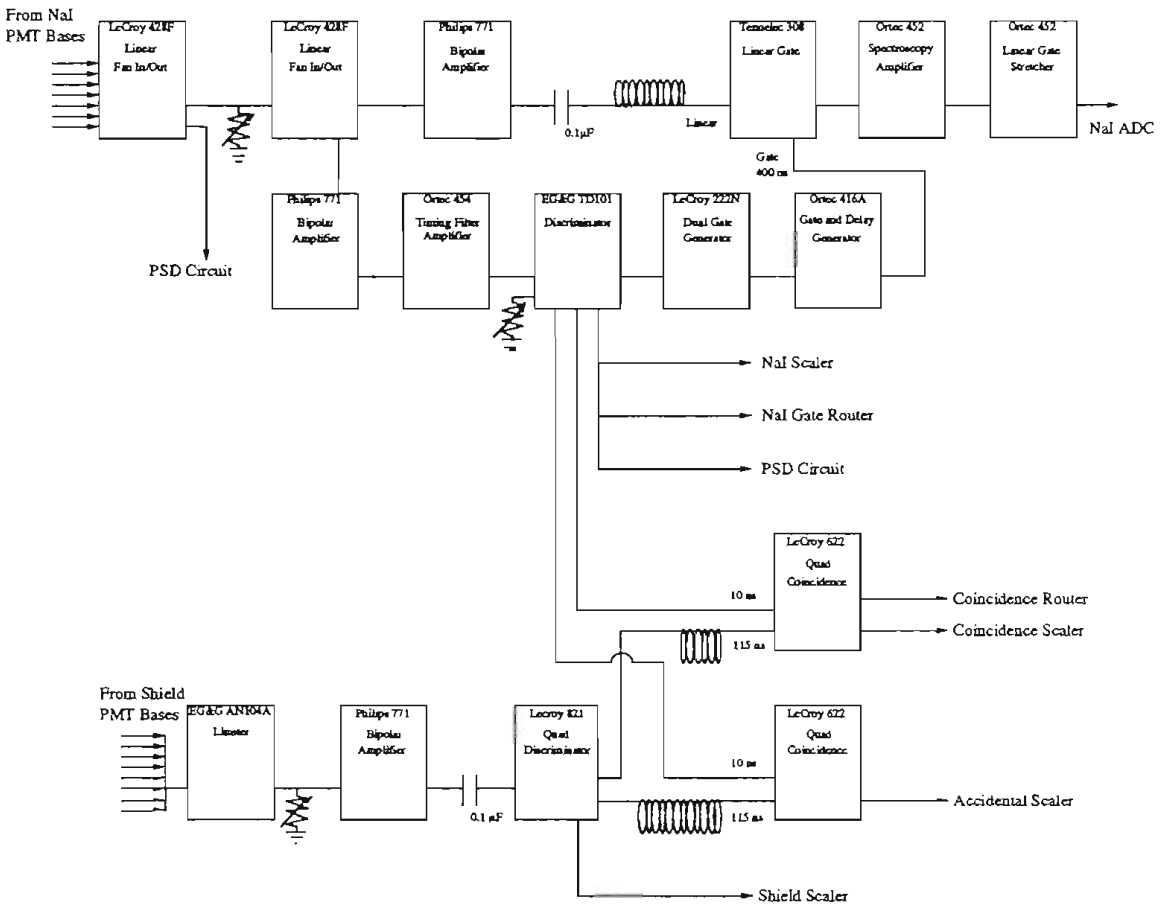

FIG. 2.5.1 Standard electronics circuit used in the experiment.

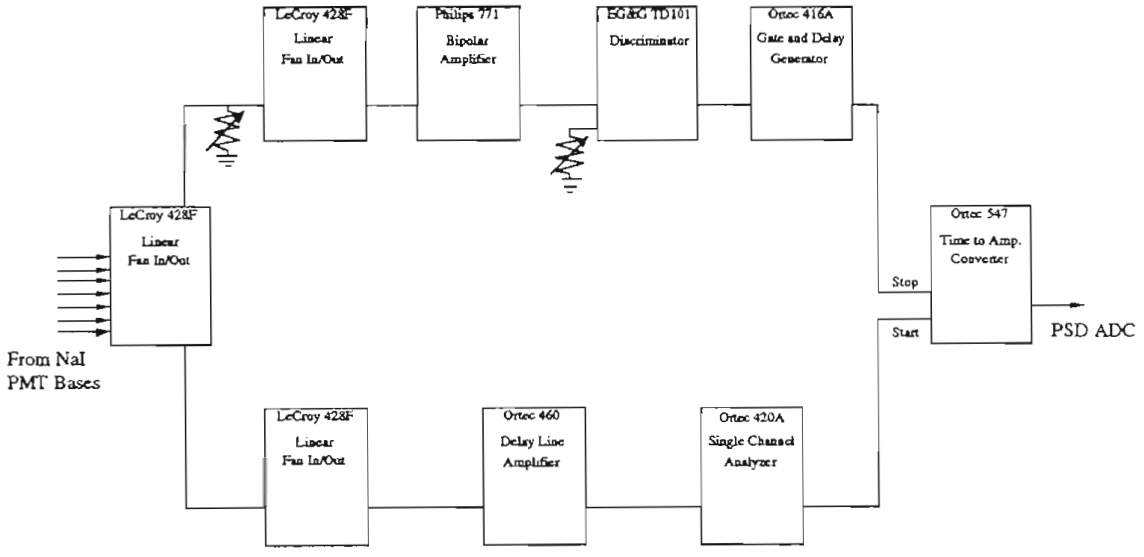

FIG. 2.5.2 Pulse shape discrimination circuit used in the experiment.

2.6 Data Acquisition

A MicroVAX 3200 running the TUNL XSYS data acquisition and analysis code was used for the data acquisition in this experiment. Signals, both linear and scaler, were fed into CAMAC ADC's and Scaler units. To allow for high data rates, event data from the ADC's were stored in a MBD-11. The MBD was flushed to the MicroVAX whenever the buffer filled. Event data included the energy, PSD-TAC, and rejection bit signals for the NaI spectrometer. Data for the NaI spectrometer were taken in the event storage mode, where events for which there were no shield rejection signals were saved. The event-mode data were written to a file for off-line analysis. This allowed for fine adjustment of the PSD-TAC gating. Scaler data included data used for on-line troubleshooting and off-line data corrections.

CHAPTER 3

Differential Cross Section

3.1 Introduction

We now describe the analysis of the data. This chapter is concerned with extracting the yields from the pulse height distributions and calculating the differential cross section. In the next chapter, polarization observables are summarized and the analyzing powers are calculated from the yields.

Differential cross sections are used to express the angular dependence of the cross section, explicitly

$$\sigma(\theta) = \frac{Y(\theta)}{Q t \varepsilon d\Omega}, \tag{3.1.1}$$

where $Y(\theta)$ is the yield at a given angle θ, Q is the number of particles impinging upon the target, t is the target thickness, ε is the detector efficiency, and $d\Omega$ is the solid angle of the detector.

In this experiment, we were unable to measure the product of the absolute efficiency and solid angle, $\varepsilon d\Omega$, because there are no reactions which produce sufficient

high energy γ rays at low energies to make an accurate determination of $\varepsilon d\Omega$. Therefore, we only measured the relative differential cross section, $\sigma(\theta)/A_0$, where A_0 is the total cross section divided by 4π. The absolute cross section has been reasonably well established by previous measurements. However, we did calculate the total cross section using estimates for the efficiency and solid angle based on previous calibrations of this detector, albeit in a somewhat different configuration. This served as a check on the reliability of our data.

Several steps were involved in extracting the differential cross section. First, the runs were normalized to the proton yields from the $^2H(d,p)^3He$ reaction. This was necessary because the target thickness changed over time, as explained in Section 2.2. Second, yields had to be extracted from the measured pulse height distributions. Finally, the relative efficiency for the three different target-detector arrangements was determined.

3.2 Normalization of the Yield to the Target Thickness

As explained in Section 2.2, the target thickness changed over time due to beam implantation. As a result, the yields had to be normalized to account for this problem. The solid-state monitor detected protons and associated tritons from the $^2H(d,p)^3He$ reaction. The monitor was positioned at 173° with respect to the beam and was collimated to 140 μsr. The protons were clearly separated, therefore providing an excellent basis for normalizations. By measuring the proton yields and using the $^2H(d,p)^3He$ cross sections given by [Bro90], an accurate measurement of Qt, the number of incident particles per second times the target thickness, was determined.

3.3 Replay of Event-Mode Data

Replay of event-mode data allowed for fine adjustment of the PSD-TAC gates. The event-mode data was sorted using the XSYS data acquisition and analysis routines. The event analysis (EVAL) codes, which sort the data, were rewritten to allow the energy spectrum to be sorted on many (20) gates placed on the PSD-TAC spectrum. These gates were then placed on the TAC peak in non-overlapping bins. Several TAC-gated energy spectra were summed in different combinations to determine which TAC gate settings were optimal. Also, the TAC spectrum was sorted on an energy gate placed on the γ-ray region of interest. This helped to determine which part of the TAC spectrum was related to γ-ray events.

Before each run, the PSD circuit was checked by setting the NaI threshold level to ~8 MeV. This increased the event rate and also allowed more neutron events into the circuit. With the low threshold, a definite peak corresponding to the γ rays was seen in the PSD-TAC spectrum. A sample of this low threshold TAC spectrum with the final PSD-TAC gate setting denoted is shown in Figure 3.3.1. With the threshold set at the level necessary for the experiment, only the upper part of the TAC peak relating to the γ rays remained. A sample TAC spectrum with the final gating set is shown in Figure 3.3.2. The effect of the TAC gating requirement is illustrated in Figures 3.3.3 and 3.3.4. Figure 3.3.3 shows the energy spectrum both with and without the TAC gating requirement. Figure 3.3.4 shows the PSD-TAC gate accepted and rejected energy spectra. As can be seen, the PSD technique reduced the γ-ray background by up to 30%.

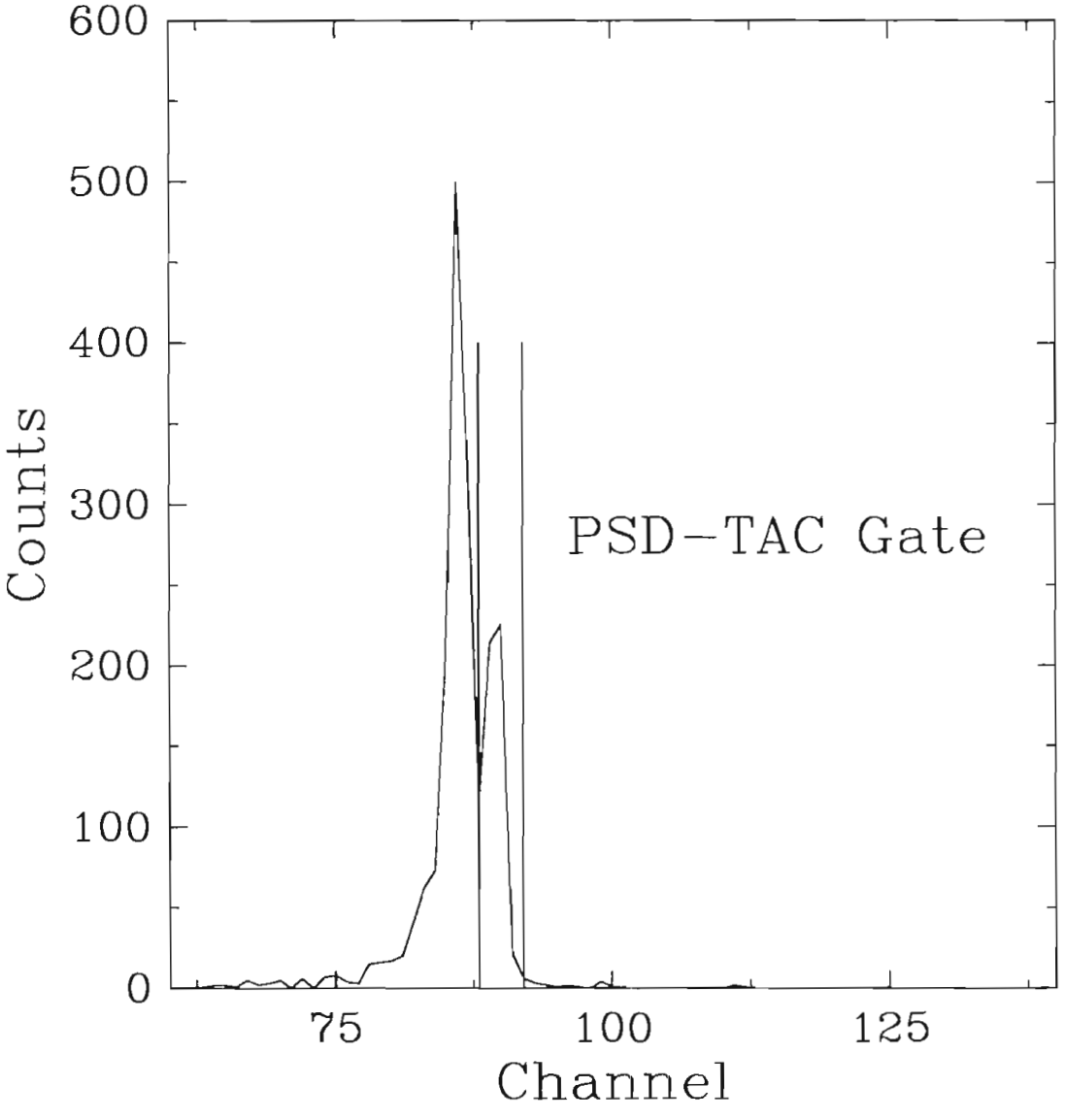

FIG. 3.3.1 Pulse shape discrimination TAC spectrum with NaI discriminator level set at 8 MeV. The peak to the right corresponds to the γ-ray events. The final gate setting is shown.

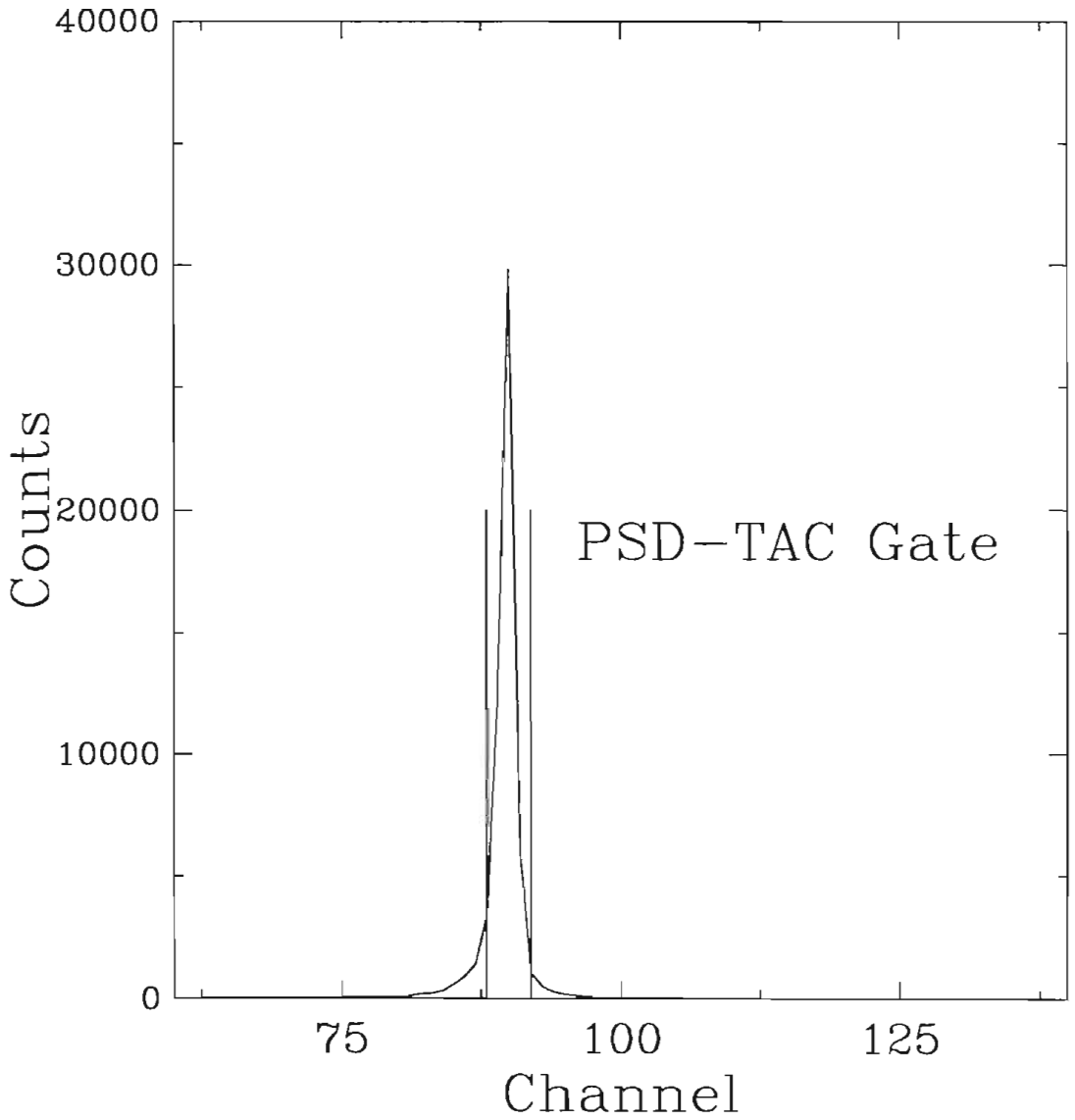

FIG. 3.3.2 Pulse shape discrimination TAC spectrum with the NaI discriminator set for the experiment. Note that the peak corresponding to γ rays remains. The final gate setting is shown.

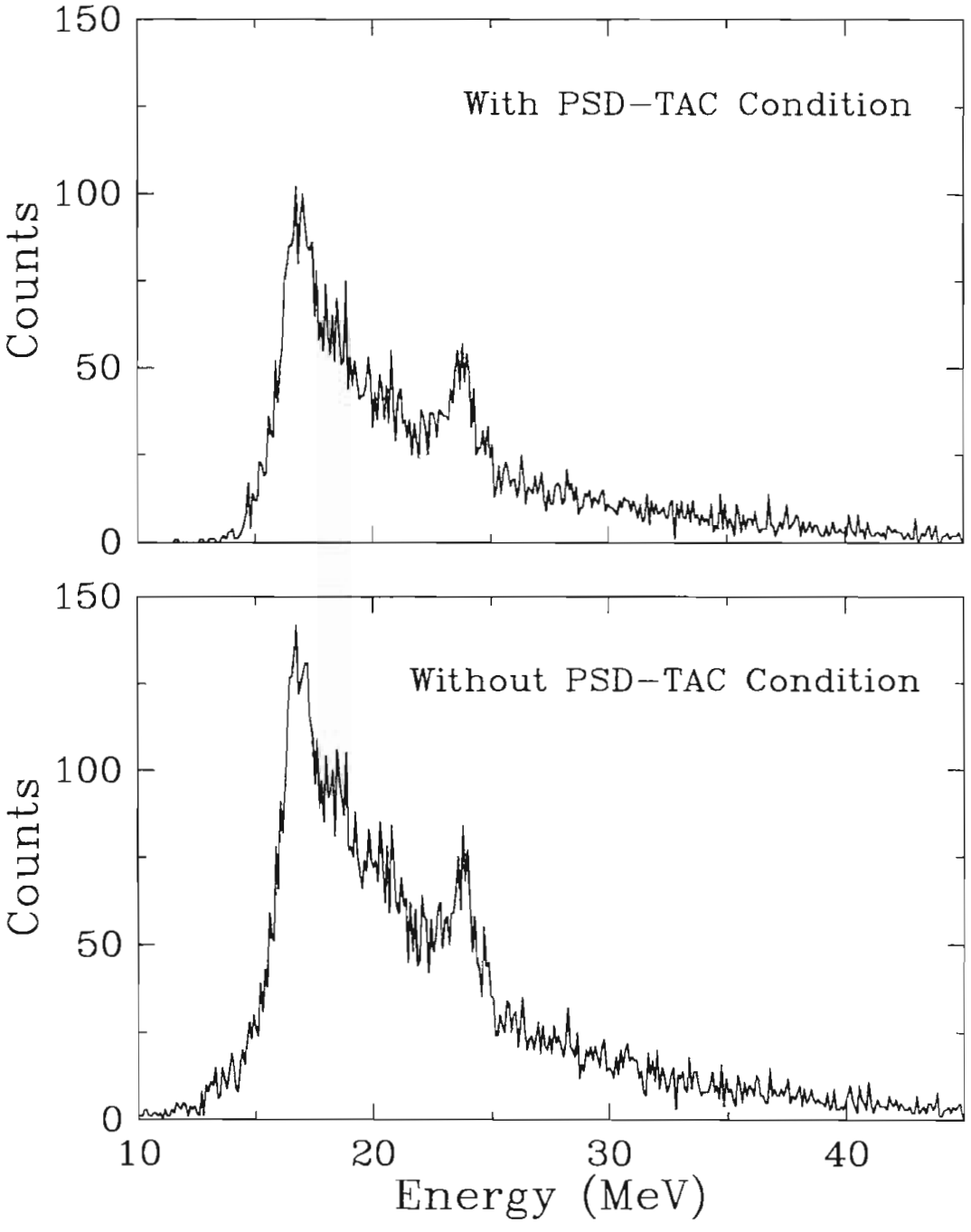

FIG. 3.3.3 Energy spectra with and without the PSD-TAC gating requirement. The region of interest is shown. The PSD requirement reduced background by ~30%.

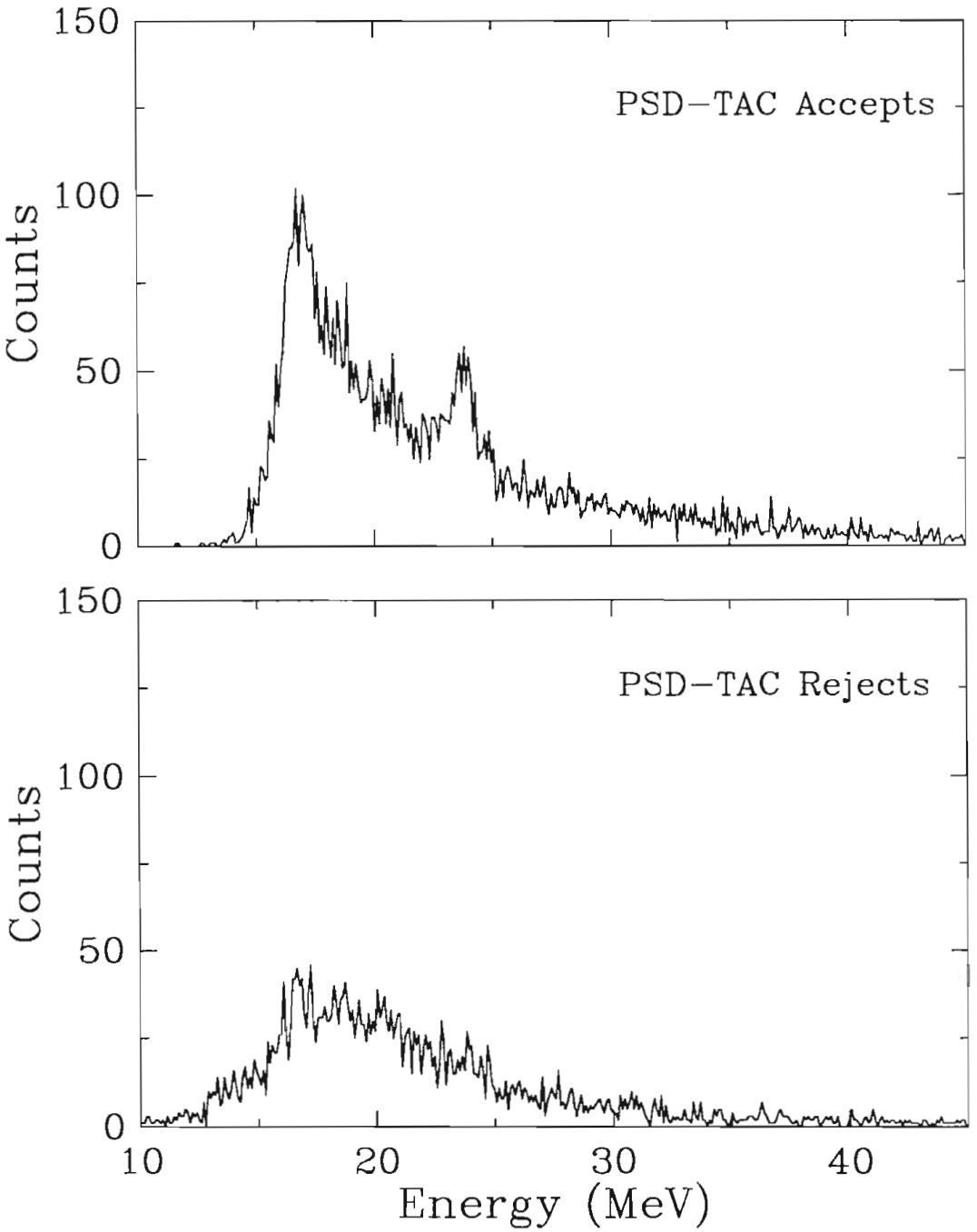

FIG. 3.3.4 Energy spectra resulting from accept (above) and reject (below) PSD-TAC gating requirements.

3.4 Spectra Fitting

The energy pulse height distribution consists of the 23.8 MeV capture γ ray superimposed on a continuous background. A sample spectrum is shown in Figure 3.4.1. In order to extract reliable yield information from the spectra, a background subtraction had to be performed. Energy spectra were simultaneously fit to the sum of a 23.8 MeV γ-ray response function and a continuum approximated by an exponential function with a quadratic argument using a χ^2 minimization routine. The background was then subtracted and yields were calculated from the sums.

The γ-ray response function was measured using the $^3H(p,\gamma)^4He$ reaction with 5.4 MeV protons. Unfortunately, to obtain the 5.4 MeV protons the tandem accelerator had to be employed. This required us to utilize a second detector in the 30° capture beam line for the response function measurement. The second detector is of a design similar to the one used in the experiment, so the response function is expected to be very similar. In order to replicate the conditions of the experiment, shielding and collimation were removed from the 30° detector and it was positioned as close to the target as possible. The response function was then measured using a Tritiated-Titanium target, shown in Figure 3.4.2.

The γ-ray response function was then parameterized by performing a fit to a composite function of two exponentials with quadratic argument [Bal92]. The functional form of the response function parameterization was given by

$$RES = \exp\left(a_1 + b_1 E' + c_1 E'^2 + d_1 E'^3 + e_1 E'^4\right) \qquad (3.4.1)$$

$$\text{for } E' < E_J,$$

$$RES = \exp\left(a_2 + b_2 E' + c_2 E'^2 + d_2 E'^3 + e_2 E'^4\right) \qquad (3.4.2)$$

for $E' > E_J$,

where a_1, b_1, c_1, d_1, e_1, a_2, b_2, c_2, d_2, e_2 are the parameters of the fit, E is the energy of the channel, and E_J is the matching point for the line shape. The fit required the function and its derivatives to be continuous at the matching point. The line shape was defined for energies between E_{low} and E_{high}. A χ^2 minimization routine, FITLINE, using MINUIT subroutines was used to fit the response function. The resulting fit is shown in Figure 3.4.2 and the parameters are given in Table 3.4.1.

The parameterized response function was then used in the fit to the pulse height distribution. Fits were performed with the program RAWFIT_LB which utilized MINUIT subroutines to perform a χ^2 minimization on the data. The RAWFIT_LB code is presented in Appendix B.1. The fit included the response function plus a background function. The response function was the measured line shape (eqs. 3.4.1 and 3.4.2) plus three fitting parameters including the height, width, and peak position as defined below. These allowed for yield normalizations and calibration errors. The parameters also allowed for differences in the responses of the two detectors (the low energy detector and the 30° beam line detector), expected to be small, by allowing the width to vary. The form of the line-shape function is given by

$$LS = hei \times \exp\left(a_1 + b_1 E' + c_1 E'^2 + d_1 E'^3 + e_1 E'^4\right) \qquad (3.4.3)$$

for $E' < E_J$,

$$LS = hei \times \exp\left(a_2 + b_2 E' + c_2 E'^2 + d_2 E'^3 + e_2 E'^4\right) \qquad (3.4.4)$$

for $E' > E_J$,

$$E' = \frac{(E - cent)}{width} + STCEN, \qquad (3.4.5)$$

where a_1, b_1, c_1, d_1, e_1, a_2, b_2, c_2, d_2, e_2 are the coefficients of the fit to the measured line shape, E is the energy of the channel, E_J is the matching point for the line shape, *STCEN* is the centroid of the measured line shape, and *hei*, *width*, and *cent* are the three fitting parameters. The line shape was defined for energies between E_{low} and E_{high} and the tail extends linearly from E_{low} to zero energy. The low energy extrapolation helped create a smooth fit, although it was not included in the sums.

As mentioned above, the energy pulse height distribution consists of the 23.8 MeV capture γ ray superimposed on a continuous background which decayed exponentially with increasing energy. The background was expected to be created by cosmic-ray events. This was confirmed in several beam-off runs where most events are caused by cosmic rays. A sample beam-off background spectrum is shown in Figure 3.4.3. It was found that the beam-off spectra were consistent with the continuous background under the capture γ-ray peak. The background fitting function was then taken to be an exponential with quadratic argument, explicitly

$$BK = \exp\left(A + BE + CE^2\right), \tag{3.4.6}$$

where E is the energy of the channel and A, B, and C are the fitting parameters. This function was found to reproduce the cosmic-ray background well. To check consistency of the background in the beam-off/beam-on runs, the beam-off spectrum was fit to the background solution of a beam-on run, allowing for an overall normalization. This fit was quite good ($\chi_\nu^2 = 1.136$), confirming that the background is due mostly to cosmic-ray events. The resulting fit is included in Figure 3.4.3.

The quality of the fits were dependent on the fitting region. The fits were most sensitive to the lower limit in the fit. If this limit was placed too far below the peak, the fit extended into the threshold region of the spectrum and the background was poorly represented. A limit placed too close to the peak cut off some of the low side of the peak,

resulting in erroneous yields. To determine the lower limit, fits were performed with a variety of lower limits set between the threshold and the peak. The best fits were found with the limits placed in the central region. For the central limit positions, the resulting fits were quite similar with the final lower limit taken to be the average of the best values. To obtain the best background estimates by allowing the largest possible region to be fit, the upper limit was set near the top of the energy spectrum, typically around 40 MeV. Using this procedure, good fits were obtained, where the resulting reduced χ^2 results for all spectra were near 1.1. The backgrounds were then subtracted and the resulting spectra were summed. The summing region was taken to be one γ-ray width up and one width down from the centroid of the peak. Sample fits and background-subtracted spectra for each of the three measured angles are shown in Figures 3.4.4, 3.4.5, and 3.4.6.

Error contributions to the sums arise from the statistical uncertainty in the yields and also by uncertainty in the background. The errors associated with the background were examined in two ways. First, a background coefficient was fixed at its final fit value plus its error. The spectrum was then refit with the one parameter fixed. The resulting background-subtracted sum was compared to the original sum, the difference indicative of the error due to the background. This was then repeated for the other background coefficients. In all cases, the differences were on the order of 1-3% of the background-subtracted sum. In the second method, the line-shape fit parameters and their associated errors were used to calculate the background-subtracted sum and its error. These errors were found to be less than or approximately equal to the statistical errors of the background-subtracted sums. It should also be noted that in determining the best fit, the background-subtracted sums were calculated. These sums were stable for different values of the final lower limit position to ~5%, further indicating that the background errors were relatively small. These investigations led us to conclude that the errors due to

the background fitting were small in comparison to the statistical errors of the sums. To insure a reasonable estimate of the errors, the statistical errors of the background-subtracted sums were weighted by the reduced χ^2 of the fit, after [Bev69], specifically

$$Statistical\ Error = \chi^2_\nu \times \sqrt{Yield}, \tag{3.4.7}$$

where χ^2_ν is the reduced χ^2 of the fit and *Yield* is the sum of counts in the spectrum.

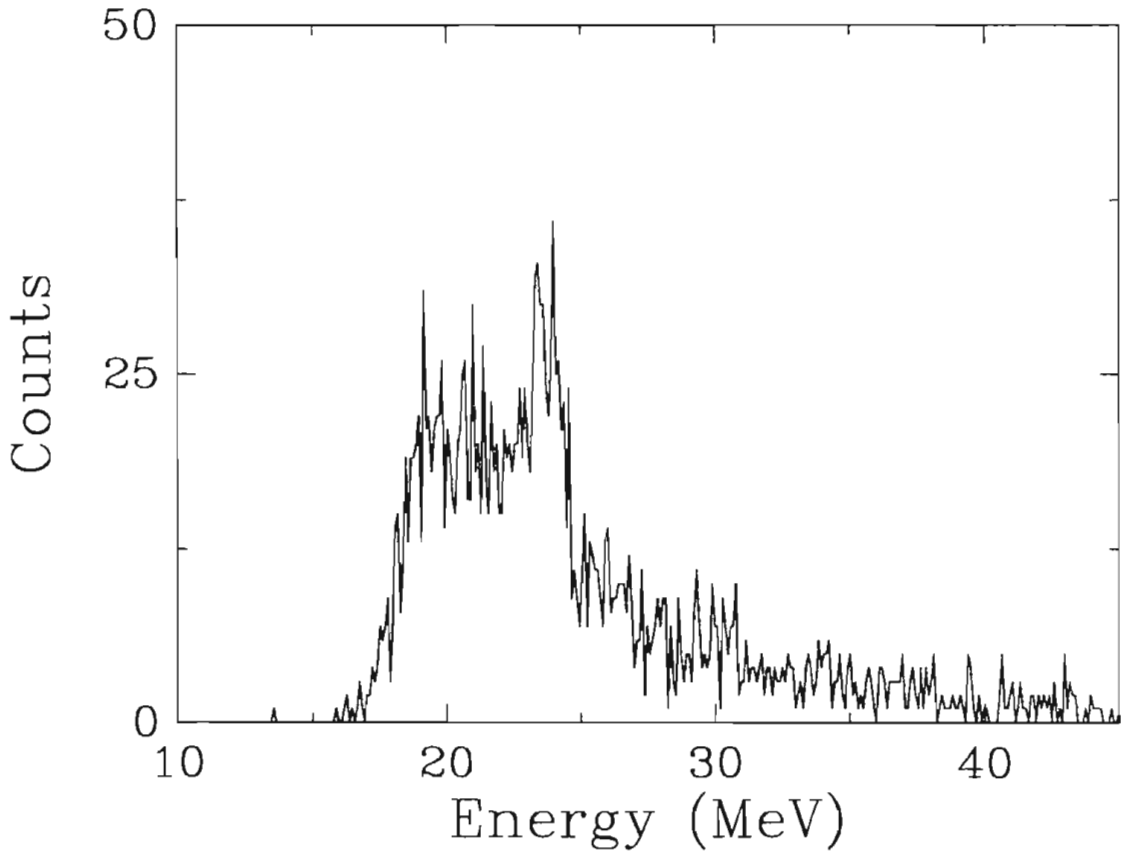

FIG. 3.4.1 The raw pulse height distribution produced by the 23.8 MeV capture γ rays emitted at $\theta = 0°$ for E_d(lab) = 80 - 0 keV.

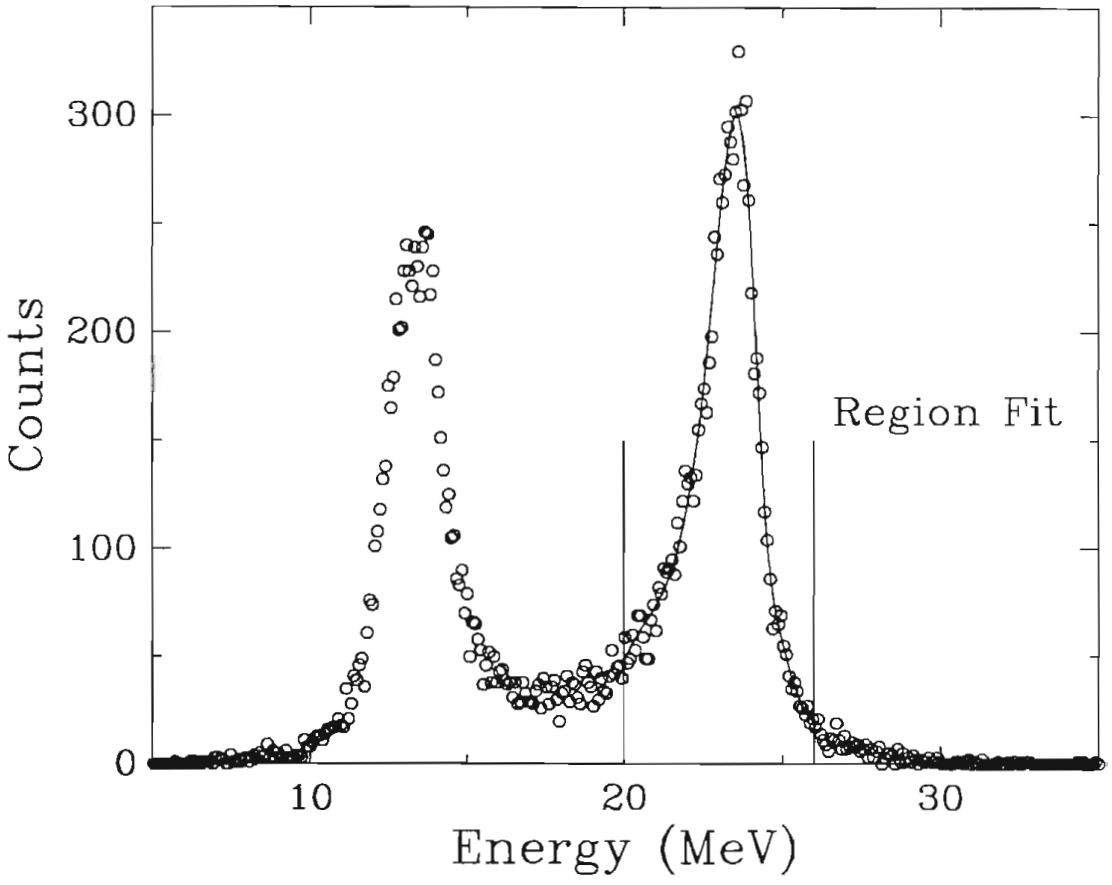

FIG. 3.4.2 NaI response function for 23.8 MeV γ rays produced in the $^{3}H(p,\gamma)^{4}He$ reaction. The resolution of the response function was found to be 2.01 MeV (full width at half maximum). Also included is the line-shape fit to the data. The fit parameters are given in Table 3.4.1.

a_1	-10149.542
b_1	1883.5661
c_1	-130.90048
d_1	4.0382005
e_1	-0.046645767
a_2	306021.28
b_2	-48598.524
c_2	2894.1017
d_2	-76.593899
e_2	0.76009464
E_J	24.39899
E_{low}	20.000
E_{high}	26.000
χ^2_r	1.027

TABLE 3.4.1 Line-shape response function fit parameters. The resulting line shape is shown in Figure 3.4.2. The form of the function is given in the text.

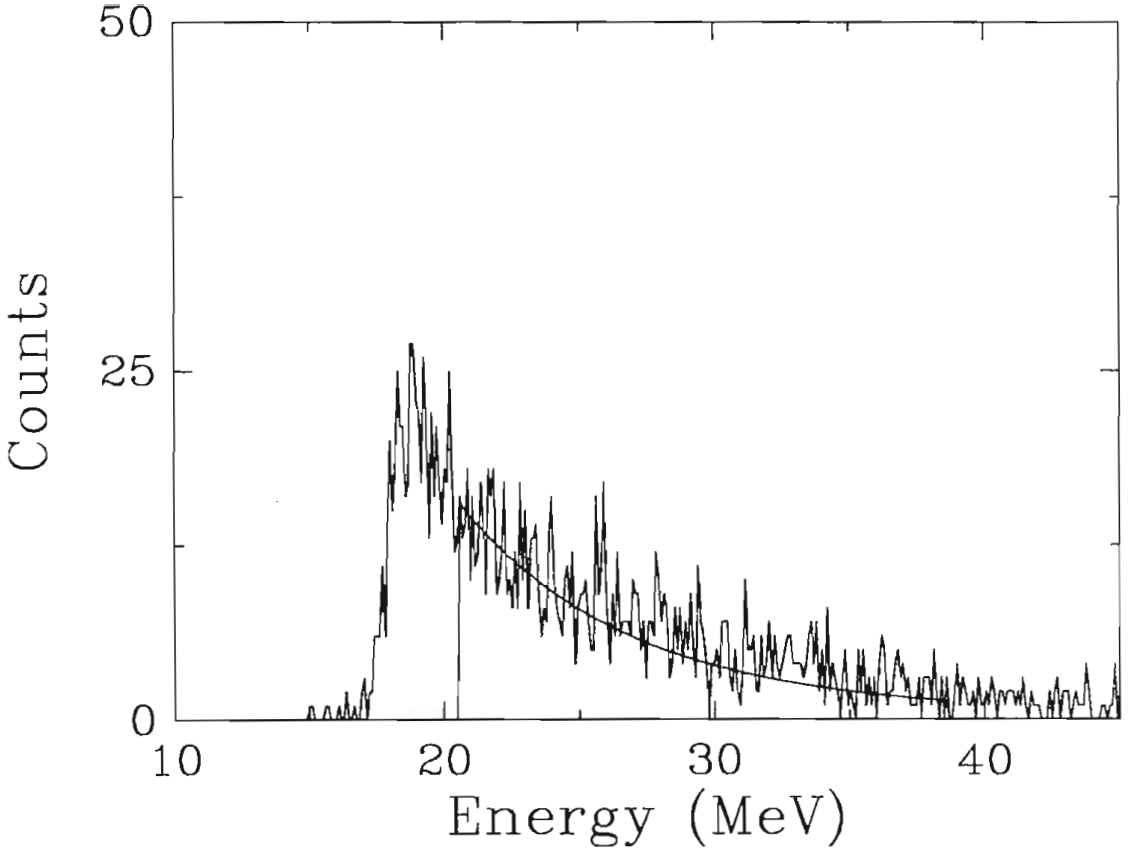

FIG. 3.4.3 Energy spectrum resulting from 25 hour beam-off background run. The background is dominated by cosmic-ray events. Also included is a fit to an exponential with quadratic argument.

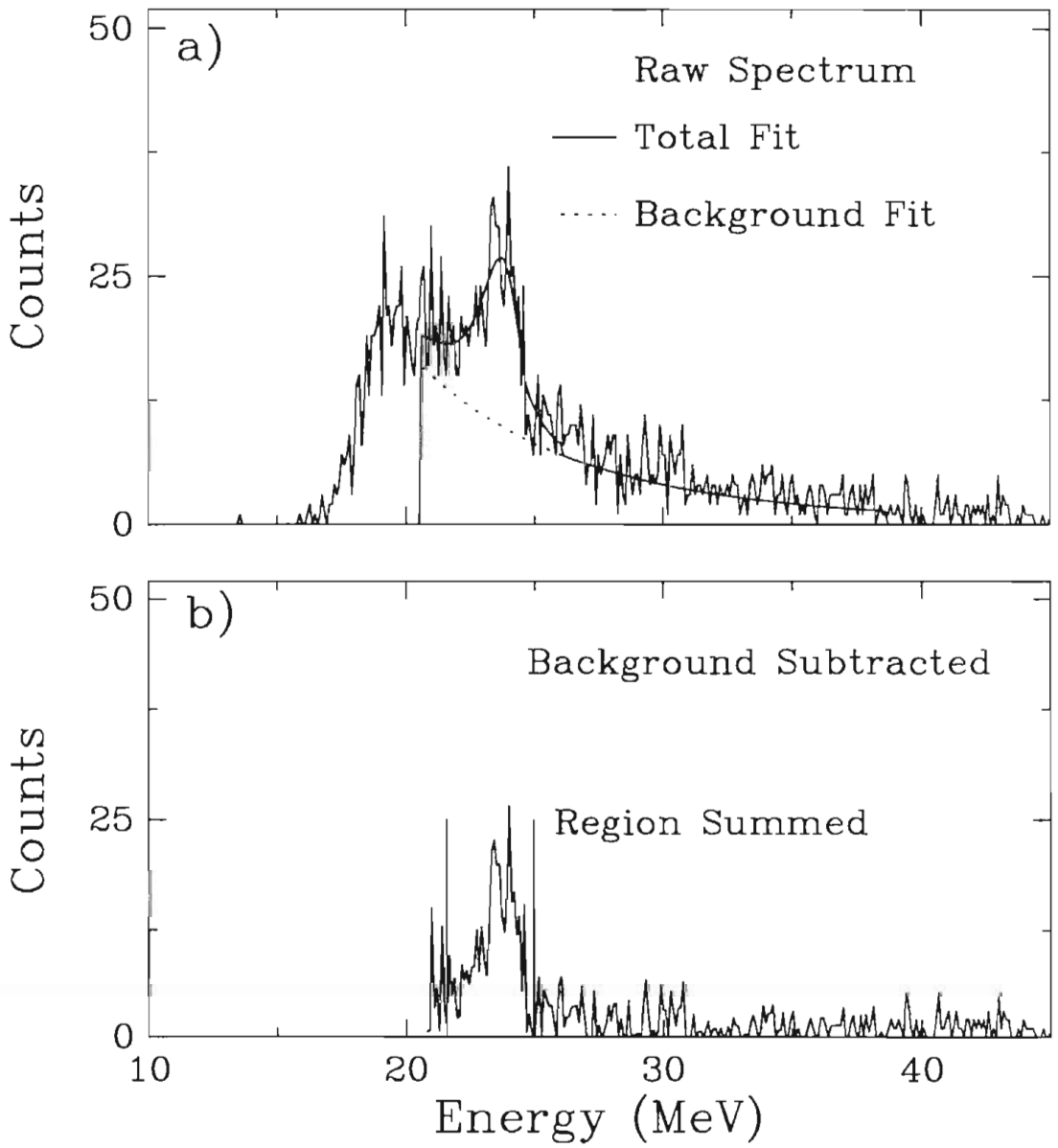

FIG. 3.4.4 The raw pulse height distribution produced by the 23.8 MeV capture γ–rays emitted at 0° for E_d(lab) = 80 - 0 keV (a) and the background subtracted pulse height distribution (b). The total fit (γ-ray response function plus exponential background function) is indicated in (a) by the solid line, the exponential background function is indicated by the dotted line. Also indicated is the summing region (discussed in the text) in the background subtracted spectra.

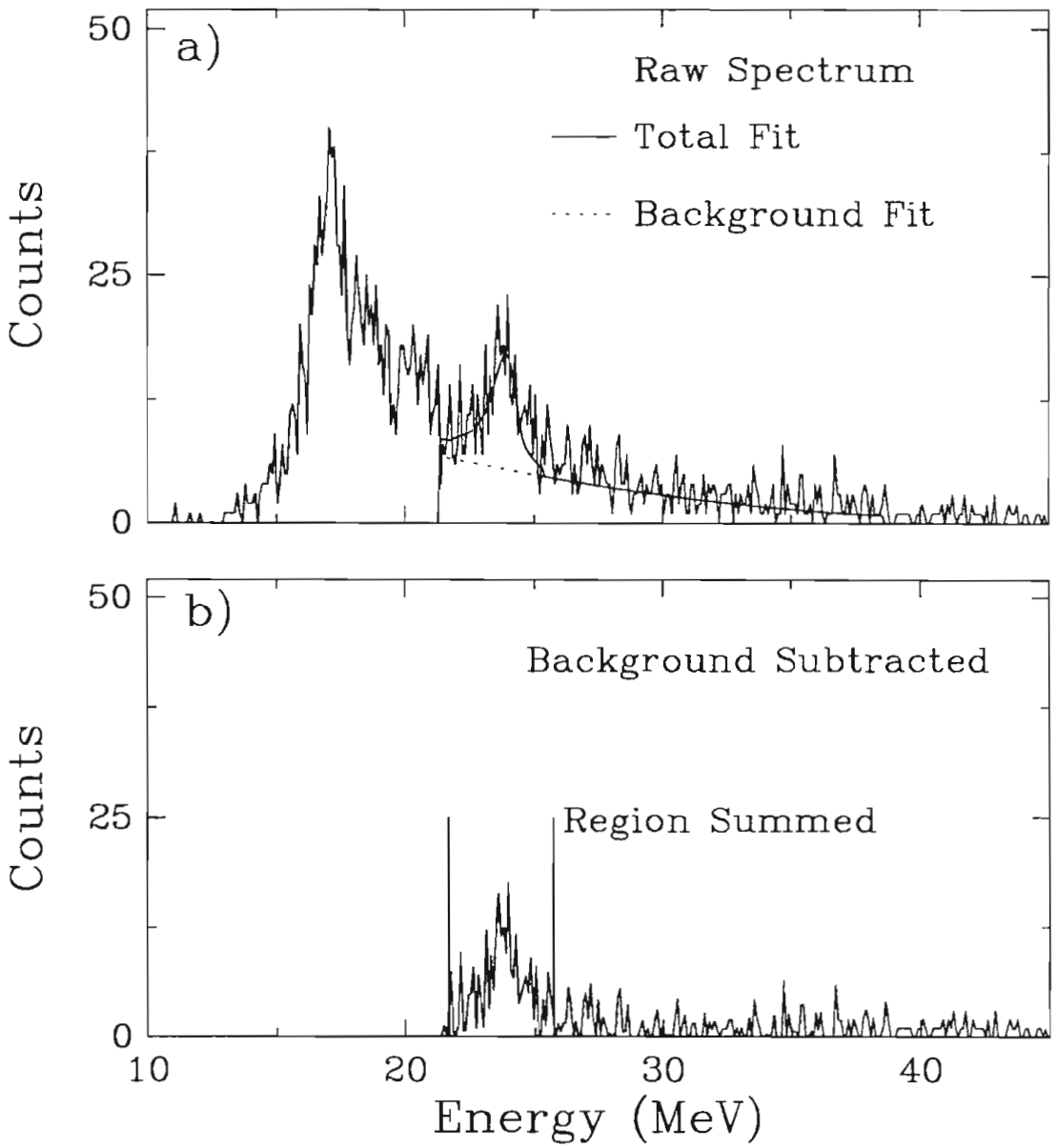

FIG. 3.4.5 The raw pulse height distribution produced by the 23.8 MeV capture γ rays emitted at 45° for E_d(lab) = 80 - 0 keV (a) and the background subtracted pulse height distribution (b). The fit and summing region are discussed in Figure 3.4.4.

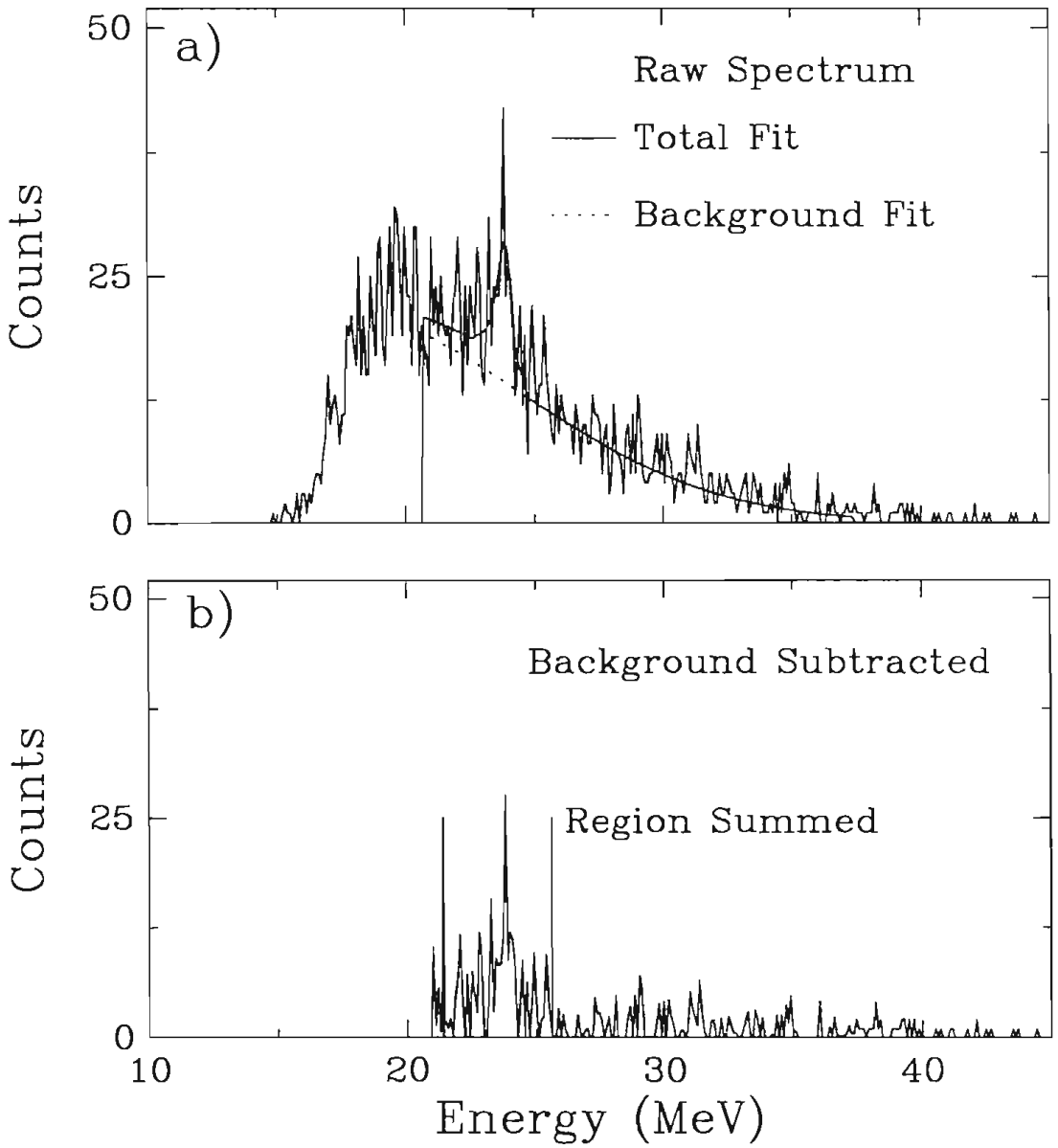

FIG. 3.4.6 The raw pulse height distribution produced by the 23.8 MeV capture γ rays emitted at 82° for E_d(lab) = 80 - 0 keV (a) and the background subtracted pulse height distribution (b). The fit and summing region are discussed in Figure 3.4.4.

3.5 Relative Efficiency Calibration

In order to calculate the differential cross section, the relative efficiencies for the three detector angles must be known. For the $\theta = 0°$ and $\theta = 45°$ measurements, similar target-detector arrangements were used. The only difference between the two measurements was the thickness of aluminum behind the target. In the $\theta = 0°$ measurement the aluminum was 0.32 mm thick and for the $\theta = 45°$ measurement it was 2.03 mm thick. The attenuation of γ rays through the two different aluminum thicknesses is 0.9981 for the 0.32 mm thick piece and 0.9882 for the 2.03 mm thick piece. Since the statistical errors of the data are large compared to the differences in the two attenuation coefficients, this effect was neglected. In the case of the $\theta = 82°$ measurement, the relative efficiency differences could not be neglected.

The measurement at $\theta = 82°$ required a reconfiguration of the target chamber and NaI detector arrangement. Here, the same target assembly as was used in the $\theta = 45°$ measurement was used. The detector was positioned as close to the target as possible, which was 1.91 cm farther from the target than in the $\theta = 45°$ measurement. Since the detector was positioned so close to the target, the 1.91 cm difference created an appreciable difference in the solid angle of the detector. Therefore, the differences in the product of the solid angle and efficiency, $\varepsilon d\Omega$, for the two configurations had to be determined.

Measurement of the relative efficiency for the two configurations was not easy. At low energies it is difficult to produce high energy γ rays at a sufficient rate to do a reasonably accurate measurement. We decided to measure the relative efficiency using the 4.44 MeV line from an Americium-Berylium source, and then extrapolate the result to

the pertinent energy using an EGS4 [Nel85] simulation. First, an Am-Be source was placed at the close target position and counted for five minutes. The 4.44 MeV line was then summed at full width half maximum. A second five minute run was taken to insure consistency of the sum. Next the source was placed at the far target position and the measurement was repeated. The resulting ratio was found to be $\sigma_{45°}/\sigma_{82°} = 1.107 \pm 0.006$, where the error indicates the statistical uncertainty of the measurement.

An EGS4 simulation was then used to extrapolate the results to higher energy γ-rays. First, the target-detector geometry was modeled and entered into the code. The model assumed a cylindrical detector divided into many segments. Each segment contained one type of material. The segmentation used is shown in Figure 3.5.1 and the materials in the segments are listed in Table 3.5.1. For the simulation, an isotropic source of γ rays was created at the target position. The γ rays were then tracked through the segments and the energy deposited in each segment was tabulated. Events which deposited most of the γ-ray energy in the NaI, while depositing less than 1 MeV in the anti-coincidence shield, were considered good events. The simulation was run for many events in each of the target configurations, and the ratio of good events was taken to be the relative efficiency. The simulation was first performed for 4.44 MeV γ rays which gave a ratio $\sigma_{45°}/\sigma_{82°} = 1.14 \pm 0.03$. Since this agrees with the Am-Be source, we felt that the EGS4 simulation was reliable. Next, the simulation was performed for 23.8 MeV γ rays where the result was found to be $\sigma_{45°}/\sigma_{82°} = 1.19 \pm 0.03$. This result was then used to adjust the yield for the $\theta = 82°$ measurement.

A second calculation was performed to check the EGS4 result. In this case, the relative absorption efficiency of an uncollimated NaI detector placed in the two positions was calculated using the absorption coefficient of NaI and integrating through the detector. The absorption efficiency is given by [Ros53]

$$\varepsilon_{absorbtion} = \int_0^{\gamma} (1 - e^{-\tau x(\beta)}) \sin\beta \, d\beta \quad , \tag{3.5.1}$$

where

$$x(\beta) = t\sec\beta \qquad \text{for} \qquad 0 \le \beta \le \tan^{-1}\left(\frac{r}{h+t}\right) = \beta', \tag{3.5.2}$$

$$x(\beta) = r\cos\beta - h\sec\beta \qquad \text{for} \qquad \beta' \le \beta \le \tan^{-1}\left(\frac{r}{h}\right) = \gamma, \tag{3.5.3}$$

and γ is the half-angle subtended by the front face, τ is the absorption coefficient for NaI, h is the distance to the front face of the detector, t is the thickness of the detector, and r is the radius of the detector. The result of this calculation was $\varepsilon_{45°}/\varepsilon_{82°} = 1.204$, in good agreement with the EGS4 result. This helped to convince us that the EGS4 code produced reasonable results.

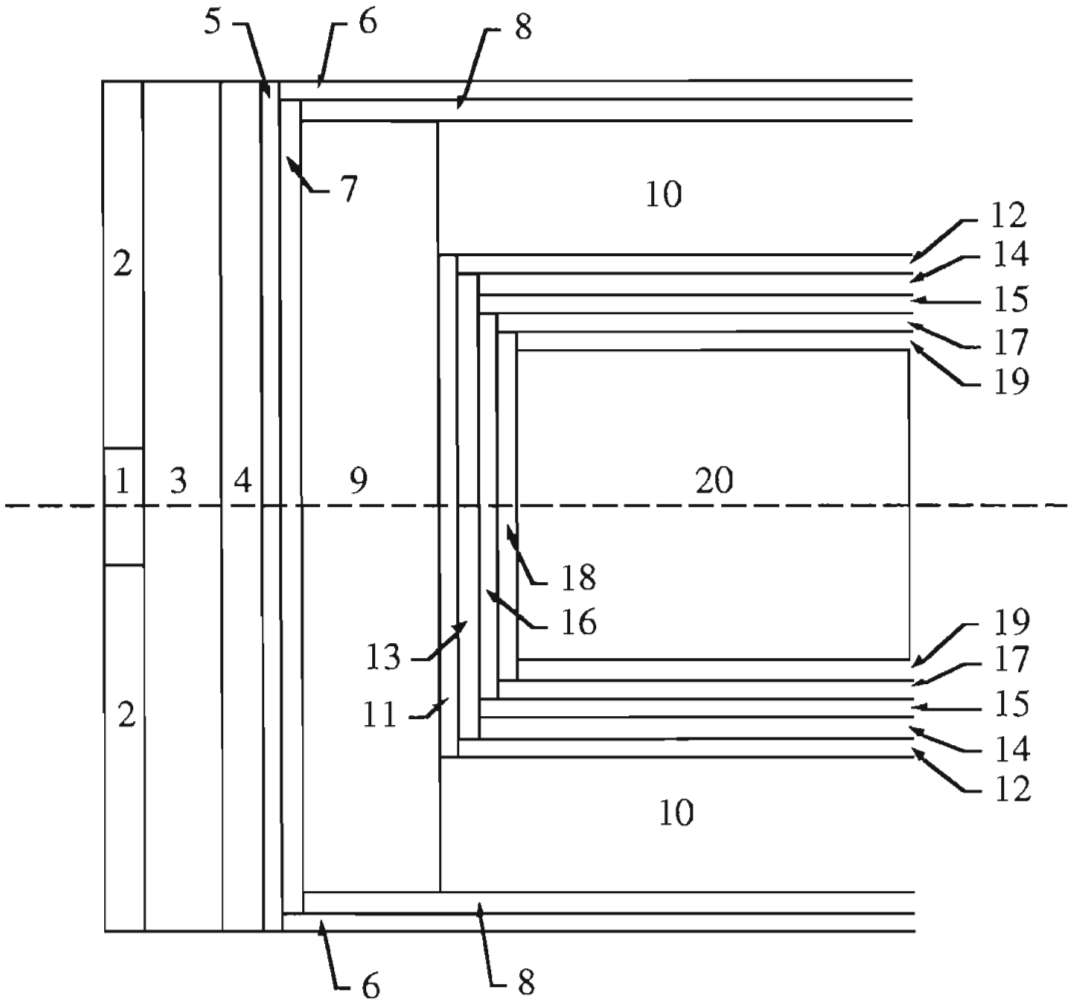

FIG. 3.5.1 Model of the detector-target setup used in the EGS4 calculation. Cylindrical symmetry about the z-axis (dashed line) was assumed. Segments consisted of right cylinders and annuluses. Materials and dimensions of the segments are given in Table 3.5.1.

Segment	Material	Inner Radius (cm)	Outer Radius (cm)	Length (cm)
1	Aluminum	-	2.54	0.20
2	Air	2.54	27.62	0.20
3	Air	-	27.62	0.32 / 2.22
4	Cadmium	-	27.62	0.04
5	Aluminum	-	27.62	0.32
6	Aluminum	27.31	27.62	34.93
7	Magnesium-Oxide	-	27.31	0.64
8	Magnesium-Oxide	26.67	27.31	34.29
9	Bicron BC-412 Scintillator	-	26.67	7.62
10	Bicron BC-412 Scintillator	13.85	26.67	26.67
11	Magnesium-Oxide	-	13.85	0.16
12	Magnesium-Oxide	13.69	13.85	26.51
13	Aluminum	-	13.69	0.16
14	Aluminum	13.53	13.69	26.25
15	Air	13.34	13.53	26.25
16	Aluminum	-	13.34	0.32
17	Aluminum	13.02	13.34	26.03
18	Magnesium-Oxide	-	13.02	0.64
19	Magnesium-Oxide	12.70	13.02	25.4
20	NaI Crystal	-	12.70	25.4

TABLE 3.5.1 Materials used in detector segments for the EGS4 calculation. Segments consisted of right cylinders and annuluses, with the radii and lengths given above. Positions of the segments are shown in Figure 3.5.1.

3.6 Accidental Corrections

The NaI spectrometer included an active shield rejection circuit. It was possible that good events in the NaI detector were accidentally rejected by this circuit. For example, this could occur when a good NaI event coincided with an uncorrelated shield event. Therefore, it was necessary to apply an accidental correction factor to the data. Given the number of accidental counts ACC and the number of coincidences between the shield and NaI detector $COIN$, the percentage of accidentals is just the ratio of ACC to $COIN$. The measured yield (Y_m) is then the true yield (Y_t) minus the percentage of accidentals. To obtain the true yield, we have

$$Y_t = Y_m \left(\frac{1}{1 - \frac{ACC}{COIN}} \right), \tag{3.6.1}$$

The resolving time of the detector was used to estimate the number of accidental counts. It is a measure of how close in time two events can occur without being rejected. The resolving time is then equal to the sum of the widths of the NaI and shield gates in the coincidence circuit. The resolving time in this experiment was t_r = 115 ns + 10 ns = 125 ns (see Section 2.5). The number of accidentals is given by

$$ACC = \frac{t_r \times Shld \times NaI}{Time}, \tag{3.6.2}$$

where *Time* is the length of a run, *Shld* is the number of shield counts in a run, and *NaI* is the number of NaI counts in a run. Average accidental corrections were on the order of 1.04 - 1.08.

3.7 Dead Time Corrections

Computer dead times result from the finite time a computer uses to process an event. If a second event occurs while the computer is processing an event, the second event is not read in. To account for this effect, the computer dead time is measured during the data taking and a correction is made in analysis. The dead time correction (DTC) is measured by sending the ADC gate into a fast (25 MHz) scaler (which has essentially no dead time) and comparing that to the total number of events. The yields are then multiplied by a correction factor:

$$DTC = \frac{number\ of\ event\ gates}{total\ number\ of\ events}. \qquad (3.7.1)$$

Dead time corrections were small in this experiment, on the order of 1.01 - 1.02 for both the NaI detector and the solid-state detector.

3.8 Energy Dependence of the Cross Section

In the experiment the target was thick enough to stop the beam, so the energies of the participating deuterons extended from 80 keV to zero energy. To investigate the contribution of different beam energies to the cross section, we calculated the thick target yield as a function of deuteron beam energy for E_d = 80 - 0 keV. In the calculation, the target was divided up into many thin layers, 5 $\mu g/cm^2$ thick. Energy loss for an 80 keV beam was calculated through the layers using the energy loss method of Anderson and Zeigler [And77]. The relative yields for each layer were then calculated using existing branching ratio and cross section data [Bro90], [Wil85]. The computer code listing is given in Appendix B.2. Results of the calculation are given in Table 3.8.1. As can be seen, 89% of the yield results from capture in the 80 - 40 keV range.

E_d (keV)	Yield (%)	Yield (% of Total)
80.0	10.1	10.1
76.9	9.4	19.5
73.8	8.8	28.3
70.7	8.2	36.5
67.7	7.6	44.1
64.7	7.0	51.1
61.8	6.4	57.5
58.9	5.8	63.3
56.1	5.3	68.6
53.3	4.8	73.4
50.6	4.2	77.6
47.9	3.8	81.4
45.3	3.3	84.7
42.8	2.8	87.5
40.3	2.5	90.0
37.9	2.1	92.1
35.5	1.8	93.9
33.2	1.4	95.3
31.0	1.2	96.5
28.8	1.0	97.5
26.7	0.7	98.2
24.6	0.6	98.8
22.7	0.4	99.2
20.8	0.3	99.5
19.0	0.2	99.7
17.2	0.1	99.8
15.5	0.1	99.9
14.0	<0.1	99.9
12.5	<0.1	100.0
11.1	<0.1	100.0
<9.7	<0.1	100.0

TABLE 3.8.1 Results of the thick target yield as a function of deuteron beam energy calculation for the $^2H(d,\gamma)^4He$ reaction with E_d = 80 - 0 keV. The γ-ray yield is expressed as a percentage of total yield. The accumulated yield percentage is also given. Details of the calculation are given in the text.

3.9 Total Cross Section

We now calculate the total cross section for comparison with previous measurements. In one previous measurement ([Wil85]), the detector was placed at $\theta = 0°$ and the cross section was calculated assuming an isotropic cross section. To best compare with this result, we calculate the cross section using our $\theta = 0°$ data and assume an isotropic cross section.

We begin by calculating the target thickness from the proton yield. We take the differential cross section at $\theta = 173°$ to be 1.1563 ± 0.080, as given by [Bro90]. The resulting target thickness is then

$$t = 1.259 \pm 0.087\ \mu g/cm^2,$$

where the error includes contributions from the statistical error of the yield and the uncertainty in the cross section.

We now calculate the total cross section. The largest uncertainty in the cross section is due to the uncertainties in the efficiency and solid angle of the detector. The efficiency was estimated by using the measured efficiency of the high-energy (30°) detector and compensating for the differences in the low-energy detector. The high-energy detector has 20.3 cm of paraffin placed in front of the detector. Paraffin was not placed in front of the low-energy detector. Also, a different summing region was used in the analysis of the low-energy data. The absence of paraffin decreases the γ-ray attenuation by 29%. The ratio of summing regions was found to be 0.5313. With these factors, the corrected efficiency is then estimated to be 22%.

The detector solid angle was more difficult to estimate because the detector had no collimation. Two extremes define the limits of the solid angle values. Any γ ray

entering the front face of the detector may interact and produce an energy signal. Those γ rays entering near the edges have a high probability of escaping before interacting in the crystal. Therefore, the solid angle defined by the front face is the upper limit. Any γ-ray in the solid angle defined by the back face more than likely interacts in the crystal, giving the lower limit. For purposes of this calculation, the solid angle is taken to be that which is subtended by the NaI crystal 7.6 cm beyond the front face.

The total cross section for $E_d(\text{lab}) = 80 - 0$ keV is then

$$\sigma = 1.15 \pm 0.63 \text{ nb},$$

where the error includes contributions from the statistical error of the yield, the uncertainty in the target thickness, an uncertainty in the efficiency of 10%, and an uncertainty in the solid angle of 0.5 sr. This result is plotted with previous data in Figure 3.9.1. It should be noted that the previous results below $E_d(\text{lab}) = 200$ keV, including [Wil85], are for measurements where the beam was stopped in the target. These data are plotted at the incident beam energy. As can be seen, the total cross section is in good agreement with the previous measurements.

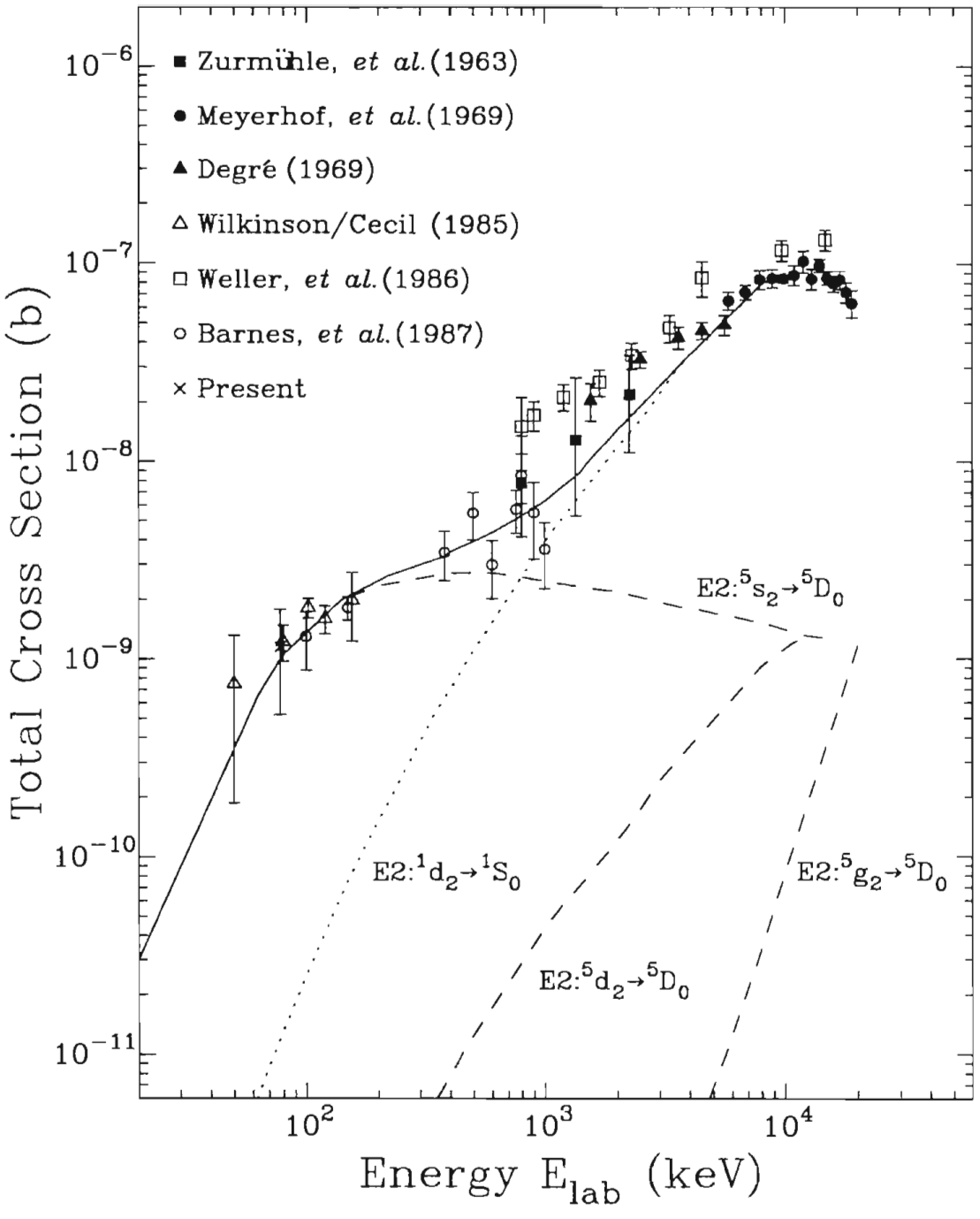

FIG. 3.9.1 The total cross section plotted as a function of lab energy. Results from earlier measurements and a previous direct capture calculation are included [Bar87].

3.10 Errors in the Differential Cross Section

Measurement of the angular distribution of a cross section is susceptible to systematic errors. Since the angular distribution was not an absolute measurement, some systematic errors were avoided, although not all sources of error were avoidable. Possible sources of systematic errors include the relative efficiency calibration, the target thickness normalization, the background subtraction, the PSD-TAC gate setting, and electronic corrections. Since a relative cross section was measured, cancellations occur that reduce many of these errors. As background subtraction errors were discussed in Section 3.4, we will concentrate on the remaining sources of error.

The largest source of systematic error was the relative efficiency calibration. Fortunately, this affected only the $\theta = 82°$ measurement. Errors arising from the Am-Be source ratio measurement did not directly affect the results since it served only as a check of the EGS4 calculation. Errors in the EGS4 calculation contributed the most uncertainty to the relative efficiency calibration. These errors were small since many systematic errors canceled out in taking the ratio. The simplified calculation gave similar results to the EGS4 calculation. We believe that the systematic errors are small, estimated to be less than 5% of the normalization factor.

Errors originating in the target thickness normalization resulted from inaccuracies in the solid-state monitor detector solid angle measurements. This only affected the $\theta = 0°$ measurement because the $\theta = 45°$ and $\theta = 82°$ measurements utilized the same geometry. Since the same monitor detector collimator was used for all measurements, only the measurement of the distance between the collimator and target introduced errors. The distance between the target and the monitor detector collimator was measured to

better than 1 mm accuracy, which corresponds to less than a 1% change in solid angle. Errors also may arise from the beam not being centered on the target, causing the solid angle subtended by the monitor detector to change. The difference in solid angle for the monitor detector when viewed from the center of the target verses the edge of the target differs is less than 4%. The combined systematic errors of the target thickness measurement are therefore estimated to be less than 5%.

The position of the PSD-TAC gate can add to the error by rejecting good events with PSD-TAC counts outside the gate. This effect was examined in off-line analysis by examining the sums in the energy spectrum as a function of TAC gate position. This technique led to the conclusion that no more than 5% of the counts were outside the PSD-TAC gate. Again, since this was only a relative measurement, the errors depend on the relative TAC efficiency. The gates in the final analysis were very similar for the three angles. This greatly reduces the errors, with a conservative estimate of 3%.

The correction factors, due to the electronic circuit applied to the data, also introduce errors into the cross section measurement. These include the dead time correction and the accidental correction. Errors in the dead time correction can arise if two events occur within the recovery time of the discriminator. Since the NaI event rate in the experiment was very low (~10 cts/sec) the errors in the dead time correction must be very small, less than 0.1%.

Accidental correction errors result in inaccuracies in the determination of the resolving time. The width of the gates was measured to better than 2 ns. Allowing for gate width changes gives an uncertainty in the resolving time of 6 ns. This corresponds to a 5% change in the resolving time. Since the number of accidentals is directly proportional to the resolving time, this leads to an error estimate of 5%.

The systematic errors are summarized in Table 3.10.1.

	Error (%)		
Source	$\theta = 0°$	$\theta = 45°$	$\theta = 82°$
Relative Efficiency	–	–	5.0
Target Normalization	5.0	5.0	5.0
PSD-TAC Gating	3.0	3.0	3.0
Dead Time Correction	0.1	0.1	0.1
Accidental Correction	3.0	3.0	3.0
Statistical Error	6.0	7.0	8.0
Total	8.9	9,6	11.5

TABLE 3.10.1 Summary of systematic errors in the differential cross section for the three angles measured.

3.11 Results

The results obtained for the angular distribution of cross section $\sigma(\theta)/A_0$ at $E_d(lab) = 80 - 0$ keV are given in Table 3.11.1 and shown in Figure 3.11.1. Since there are identical deuterons in the entrance channel, the cross section must be symmetric about $\theta = 90°$ in the center-of-mass system. This can be understood by examining the inverse reaction $^4He(\gamma,d)^2H$. In the center-of-mass system, the ^4He nucleus photodisintegrates into two deuterons, which recoil at angles θ and θ', see Figure 3.11.2. Since the deuterons are identical particles, $\theta + \theta' = \pi$, or $\theta' = \pi - \theta$. The system can now be rotated about the ϕ-axis so that deuteron 2 is in the same hemisphere as deuteron 1 was originally. This shows that the same number of deuterons emerge at angles θ and $\pi - \theta$, *i. e.* the cross section is symmetric about $\theta_{cm} = 90°$. It should be noted that this does not hold for polarization observables, since one deuteron is polarized, this breaks the ϕ symmetry. Therefore, the data for the relative cross section have been reflected around $\theta_{cm} = 90°$. The indicated errors represent the statistical uncertainty of the data. (The finite geometry corrected data are given in Appendix C.) The angular distribution $\sigma(\theta)/A_0$ exhibits a non-isotropic component indicating the presence of non s-wave capture.

Due to the small number of data points, an extraction of the contributing transition matrix elements (TME's) is not feasible at this point. With the addition of analyzing power data, the data set will be large enough to extract information on these TME's. The next chapter describes the analyzing power measurement, and the following chapter describes the extraction of transition matrix elements.

θ_{cm} (degrees)	$\sigma(\theta)/A_0 \pm \Delta\,\sigma(\theta)/A_0$
0.	0.723 ± 0.0373
45.	0.964 ± 0.0668
82.	1.103 ± 0.0853

TABLE 3.11.1 Results obtained for the angular distribution of cross section $\sigma(\theta)/A_0$ at E_d(lab) = 80 - 0 keV for the $^2H(d,\gamma)^4He$ reaction. The indicated errors represent the statistical uncertainty of the data.

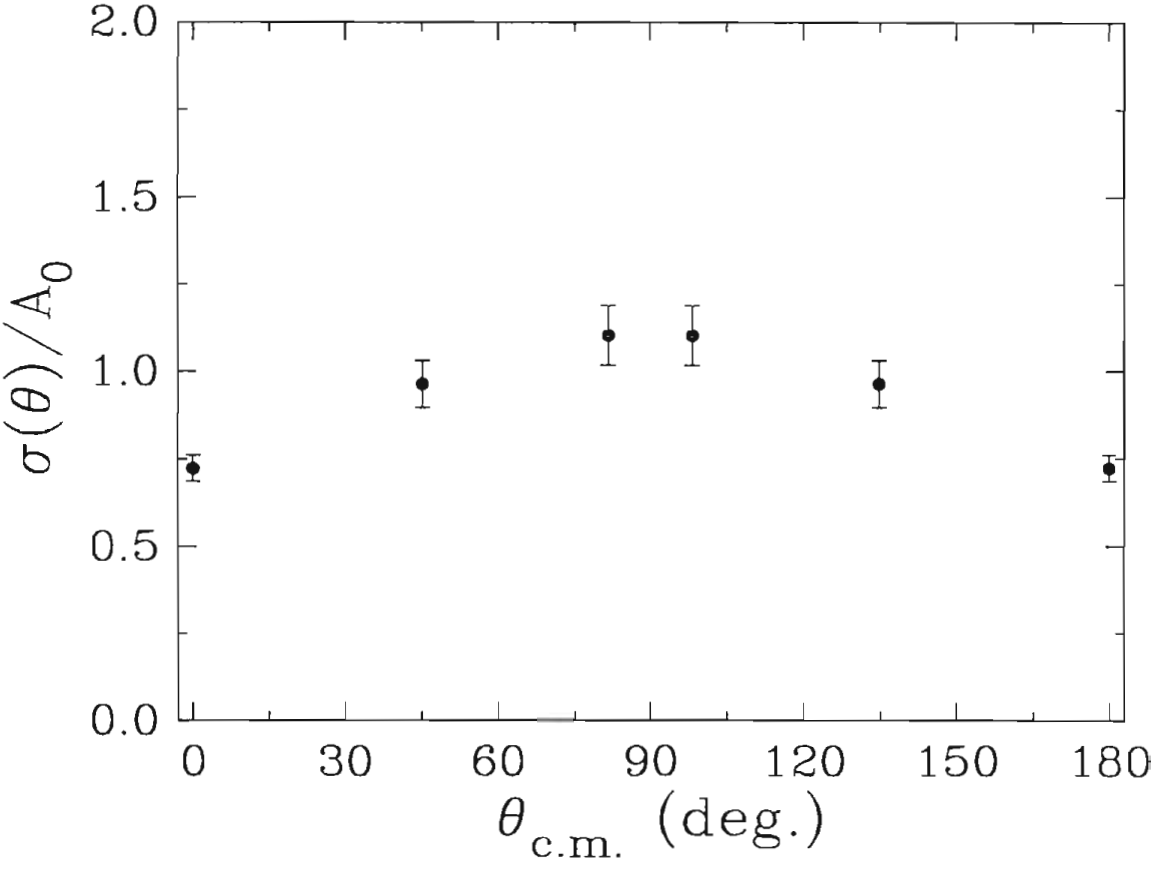

FIG. 3.11.1 Results obtained for the angular distribution of cross section $\sigma(\theta)/A_0$ at E_d(lab) = 80 - 0 keV for the $^2H(d,\gamma)^4He$ reaction. Since the cross section must be symmetric about $\theta = 90°$ (due to the identical deuterons in the entrance channel), the data has been reflected around $\theta = 90°$. The indicated errors represent the statistical uncertainty of the data.

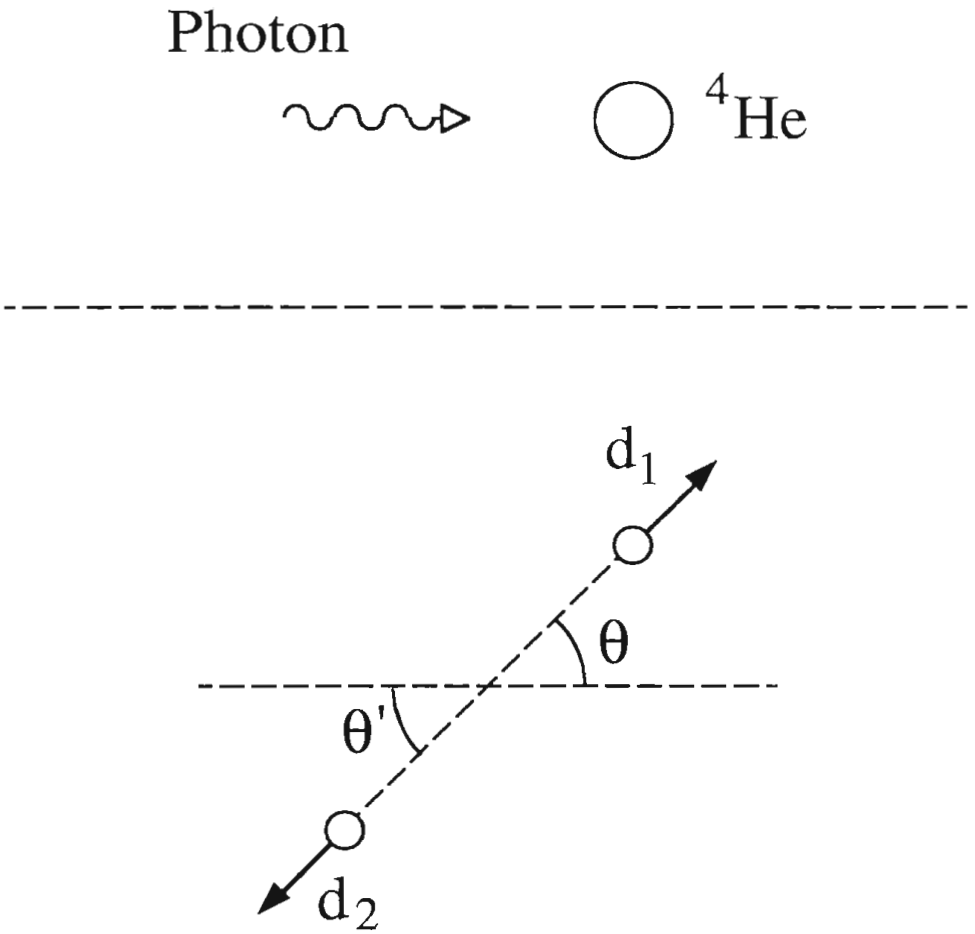

FIG. 3.11.2 ^{4}He(γ,d)^{2}H reaction seen in the center-of-mass system. The ^{4}He nucleus photodisintegrates, above, leaving two deuterons recoiling at θ and θ´, below.

CHAPTER 4

Polarization Observables

4.1 Introduction

The focus of this study has been to determine which transition amplitudes are involved in the $^2H(\vec{d},\gamma)^4He$ reaction at low energies. Analyzing powers are sensitive to the interference of transition amplitudes, hence, provide a sensitive means of determining which transitions and multipolarities are involved in a reaction. We have measured the vector and tensor analyzing powers $A_y(\theta)$ and $A_{yy}(\theta)$ of the $^2H(\vec{d},\gamma)^4He$ reaction at E_d = 80 keV. This chapter first describes the polarization observables, and then goes on to present the experimental results.

4.2 Madison Convention

As explained in Section 2.3, beams are polarized by rearranging the populations of magnetic substates to create a desired polarization state. A formalism must be used to describe phenomena associated with polarized beams. In this work, we have used the

Madison Convention (see Figure 4.2.1) [Hae75] to describe the polarization phenomena. It is defined to be a right-handed coordinate system with the z-axis along the beam momentum axis $\vec{k}_{in}$, and positive y-axis along the normal to the reaction plane, $\vec{k}_{in} \times \vec{k}_{out}$. The polarization axis ζ is defined by the angles β and ϕ. β is the angle between the z-axis and the quantization axis ζ. ϕ is the angle between the projection of the quantization axis ζ onto the x-y plane and the y-axis.

Polarization of a spin-1 deuteron beam can be expressed in terms of a rank 2 tensor. The polarization parameters can be expressed either with Cartesian tensor moments p_i, p_{ij} or spherical tensor moments t_{kq}. In this experiment it is easiest to work with the Cartesian system. The Cartesian spin moments are defined by

$$p_i = \langle S_i \rangle \qquad i = x, y, z \qquad \text{vector polarization} \qquad (4.2.1)$$

$$p_{ij} = \frac{3}{2}\langle S_i S_j + S_j S_i \rangle - 2\delta_{ij} \qquad i,j = x, y, z \qquad \text{tensor polarization} \qquad (4.2.2)$$

where $\vec{S}$ is the spin-1 operator.

The polarized-ion source creates beam having axial symmetry where ζ is along the z-axis. In this case, the polarization can be expressed in terms of two quantities, p_ζ and $p_{\zeta\zeta}$ which are given by

$$p_\zeta = N_+ - N_- \qquad (4.2.3)$$

$$p_{\zeta\zeta} = 1 - 3N_0 \qquad (4.2.4)$$

where N_+, N_0, and N_- are the fractions of particles with $m_j = +1$, 0, and -1, respectively.

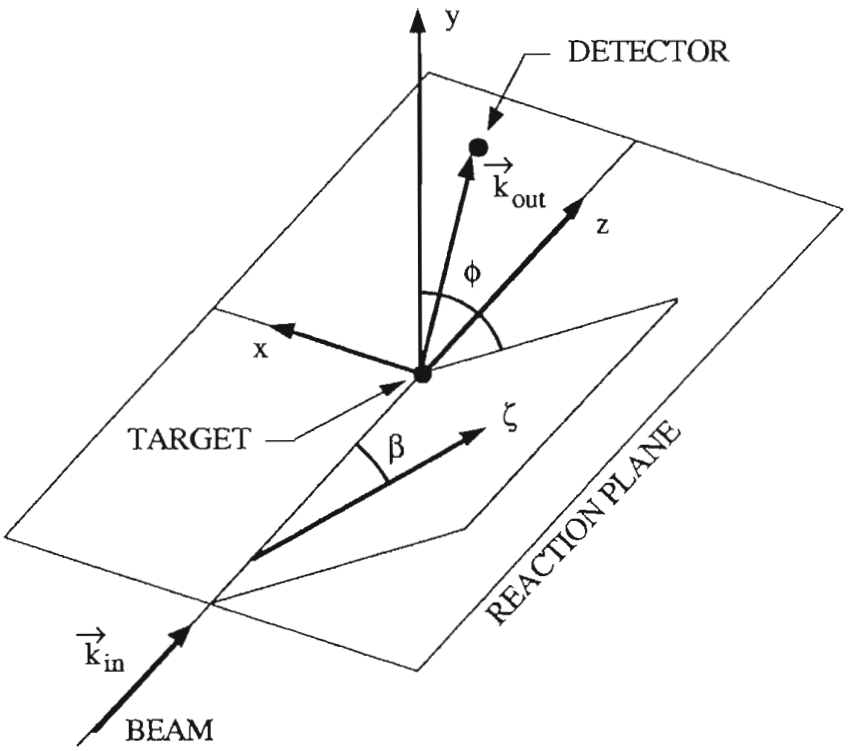

FIG. 4.2.1 Coordinate system as defined by the Madison Convention. The figure illustrates the right-handed coordinate system with the z-axis along the beam momentum axis $\vec{k}_{in}$, and positive y-axis along the normal to the reaction plane, $\vec{k}_{in} \times \vec{k}_{out}$. The polarization axis ζ is defined by β, the angle between the z-axis and the quantization axis ζ, and ϕ, the angle between the projection of the quantization axis ζ onto the x-y plane and the y-axis.

4.3 Analyzing Power Formulas

Analyzing powers formulas are derived from the expression for the polarized cross section $\sigma_P(\theta)$ in terms of the unpolarized cross section $\sigma_0(\theta)$ and spin tensor moments. The cross section for incident spin-1 particles in the reaction $A(\vec{a},b)B$ at a given angle θ is given by [Dar71]

$$\begin{aligned}\sigma_P(\theta) = \sigma_0(\theta)[1 &+ \frac{3}{2} p_\zeta A_y(\theta)\sin(\beta)\cos(\phi) + \frac{1}{4} p_{\zeta\zeta} A_{zz}(\theta)(3\cos^2(\beta)-1) \\ &+ \frac{1}{4} p_{\zeta\zeta} A_{zz}(\theta)(3\cos^2(\beta)-1) \\ &+ p_{\zeta\zeta} A_{xz}(\theta)\sin(\beta)\cos(\beta)\sin(\phi) \\ &+ \frac{1}{4} p_{\zeta\zeta}(A_{xx}(\theta)-A_{yy}(\theta))\sin^2(\beta)\cos(2\phi)]. \qquad (4.3.1)\end{aligned}$$

By choosing certain β and ϕ combinations, a specified analyzing power can be measured.

To measure $A_y(\theta)$ and $A_{yy}(\theta)$ simultaneously, β is set to 90° and ϕ is set to 0°, which corresponds to having the quantization axis along the y-axis. With $\beta = 90°$ and $\phi = 0°$, eq. 4.3.1 reduces to

$$\sigma_P(\theta) = \sigma_0(\theta)[1 + \frac{3}{2} p_\zeta A_y(\theta) + \frac{1}{2} p_{\zeta\zeta} A_{yy}(\theta)]. \qquad (4.3.2)$$

Since eq. 4.3.2 has two analyzing powers, either two detectors or two polarization states must be used for the measurement. Since two detectors would not fit in the close geometry of the setup, the experiment involved two polarization states. The two polarization states included the $3 \leftrightarrow 5$ transition for State 1, resulting in theoretical limits of $p_\zeta = -1/3$ and $p_{\zeta\zeta} = -1$, and the $2 \leftrightarrow 6$ transition for State 2, resulting in theoretical limits of $p_\zeta = -1/3$ and $p_{\zeta\zeta} = +1$. Inserting $p_{\zeta 1}$, $p_{\zeta\zeta 1}$, $p_{\zeta 2}$, and $p_{\zeta\zeta 2}$ into eq. 4.3.2 gives

$$\frac{\sigma_1(\theta)}{\sigma_0(\theta)} = [1 + \frac{3}{2} p_{\zeta 1} A_y(\theta) + \frac{1}{2} p_{\zeta\zeta 1} A_{yy}(\theta)], \tag{4.3.3}$$

$$\frac{\sigma_2(\theta)}{\sigma_0(\theta)} = [1 + \frac{3}{2} p_{\zeta 2} A_y(\theta) + \frac{1}{2} p_{\zeta\zeta 2} A_{yy}(\theta)], \tag{4.3.4}$$

where $\sigma_1(\theta)$ and $\sigma_2(\theta)$ are the polarized cross sections for States 1 and 2, respectively, and $\sigma_0(\theta)$ is the unpolarized cross section. Eqs. 4.3.3 and 4.3.4 are arranged to show that the measurement reduces to a ratio of cross sections. Detector efficiency and solid angle, along with the target thickness, cancel out, eliminating the errors originating from these sources. Solving for the analyzing powers gives

$$A_y(\theta) = \frac{2p_{\zeta\zeta 1}}{3(p_{\zeta 2}p_{\zeta\zeta 1} - p_{\zeta 1}p_{\zeta\zeta 2})}\left[\frac{Y_2(\theta)}{Y_U(\theta)} - 1 - \frac{p_{\zeta\zeta 2}\, Y_1(\theta)}{p_{\zeta\zeta 1}\, Y_U(\theta)} + \frac{p_{\zeta\zeta 2}}{p_{\zeta\zeta 1}}\right], \tag{4.3.5}$$

$$A_{yy}(\theta) = \frac{2p_{\zeta 2}}{p_{\zeta 2}p_{\zeta\zeta 1} - p_{\zeta 1}p_{\zeta\zeta 2}}\left[\frac{Y_1(\theta)}{Y_U(\theta)} - 1 - \frac{p_{\zeta 1}\, Y_2(\theta)}{p_{\zeta 2}\, Y_U(\theta)} + \frac{p_{\zeta 1}}{p_{\zeta 2}}\right], \tag{4.3.6}$$

where $Y_1(\theta)$ and $Y_2(\theta)$ are the yields for the two polarized states and $Y_U(\theta)$ is the yield of the unpolarized yield. Typical values for the polarizations are $p_{\zeta 1} = -0.307 \pm 0.021$, $p_{\zeta\zeta 1} = -0.913 \pm 0.054$, $p_{\zeta 2} = -0.290 \pm 0.022$, and $p_{\zeta\zeta 2} = 0.861 \pm 0.048$, where the indicated errors are statistical.

4.4 Statistical Errors of the Analyzing Powers

Now consider the statistical errors of the analyzing powers. What uncertainty exists in the final result when the result is derived from several parameters with individual uncertainties? Propagation of errors is the method used to estimate these uncertainties. For a function, *f*, which contains contributions from several uncorrelated independent measurements, the error function is given by [Bev69]

$$\sigma_f^2 \equiv \sigma_u^2\left(\frac{\partial f}{\partial u}\right)^2 + \sigma_v^2\left(\frac{\partial f}{\partial v}\right)^2 + \cdots, \tag{4.4.1}$$

where σ_u, σ_v, ... are the errors in variables u, v, ... Specifically, we have

$$\left(\Delta A_y(\theta)\right)^2 = (\Delta Y_1(\theta))^2\left(\frac{\partial A_y(\theta)}{\partial Y_1(\theta)}\right)^2 + (\Delta Y_2(\theta))^2\left(\frac{\partial A_y(\theta)}{\partial Y_2(\theta)}\right)^2$$

$$+(\Delta Y_U(\theta))^2\left(\frac{\partial A_y(\theta)}{\partial Y_U(\theta)}\right)^2, \tag{4.4.2}$$

$$\left(\Delta A_{yy}(\theta)\right)^2 = (\Delta Y_1(\theta))^2\left(\frac{\partial A_{yy}(\theta)}{\partial Y_1(\theta)}\right)^2 + (\Delta Y_2(\theta))^2\left(\frac{\partial A_{yy}(\theta)}{\partial Y_2(\theta)}\right)^2$$

$$+(\Delta Y_U(\theta))^2\left(\frac{\partial A_{yy}(\theta)}{\partial Y_U(\theta)}\right)^2. \tag{4.4.3}$$

The errors of the yields are estimated to be

$$\Delta Y_i(\theta) = \chi_v^2\sqrt{Y_i(\theta)}, \tag{4.4.4}$$

as explained in Section 3.4.

For $A_y(\theta)$ and $A_{yy}(\theta)$, the statistical errors are given by

$$\left(\Delta A_y(\theta)\right)^2 = \left[\frac{2p_{zz1}}{3\left(p_{z2}p_{zz1} - p_{z1}p_{zz2}\right)}\right]^2\left[\left(\frac{1}{Y_0(\theta)^2}\right)\left(Y_2(\theta)\right)^2\right.$$

$$+\left(\frac{p_{zz2}}{p_{zz1}}\frac{1}{Y_0(\theta)}\right)^2\left(\Delta Y_1(\theta)\right)^2$$

$$\left.+\left[\frac{p_{zz2}}{p_{zz1}}\frac{Y_1(\theta)}{Y_0(\theta)^2} - \frac{Y_2(\theta)}{Y_0(\theta)^2}\right]^2\left(\Delta Y_0(\theta)\right)^2\right], \tag{4.4.5}$$

$$\left(\Delta A_{yy}(\theta)\right)^2 = \left[\frac{2p_{z2}}{p_{z2}p_{zz1} - p_{z1}p_{zz2}}\right]^2\left[\left(\frac{1}{Y_0(\theta)^2}\right)\left(Y_1(\theta)\right)^2\right.$$

$$+\left(\frac{p_{z1}}{p_{z2}}\frac{1}{Y_0(\theta)}\right)^2\left(\Delta Y_2(\theta)\right)^2$$

$$+\left[\frac{p_{z1}}{p_{z2}}\frac{Y_2(\theta)}{Y_0(\theta)^2}-\frac{Y_1(\theta)}{Y_0(\theta)^2}\right]^2\left(\Delta Y_0(\theta)\right)^2\Bigg]. \qquad (4.4.6)$$

As already noted, many errors involved in cross section measurements cancel out in analyzing power measurements, since analyzing powers are expressed as ratios of yields. Errors due to the relative efficiency calibration, relative target thickness normalization, and PSD-TAC settings cancel out. The dominant source of error in the analyzing power is the uncertainty in the beam polarization, estimated to be less than 10%.

4.5 Target Thickness Normalization

Since the analyzing powers depend upon measurement of yields in different polarization states, it was necessary to normalize the γ-ray yields to the proton yields for the three states. This resulted from the changing target thicknesses during runs. The normalization method was similar to that used for the differential cross section calculation, with the complication of the protons having analyzing powers. To compensate for this effect, runs were taken to measure the analyzing powers of the protons. These runs were short runs to eliminate the effects due to changing target thickness, and were repeated several times throughout the experiment to insure consistency. The analyzing powers of the protons were then folded into the normalization procedure.

4.6 Depolarization in the Target

In our region, depolarization of the deuteron beam may affect the results of the measurement. In order to depolarize, a deuteron must pick up an electron for a time comparable to the Larmor precession period of an electron around a deuteron nucleus [Cla70]. The Larmor period is given by

$$T_L = \frac{h}{\Delta E} \tag{4.6.1}$$

where h is Planck's constant and ΔE is the hyperfine structure splitting. For a deuteron, $\Delta E = 2.17 \times 10^{-25}$ J, while the Larmor period is 3.05×10^{-9} seconds. The 80 keV deuteron takes 5.16×10^{-12} seconds to stop in the Deuterated-Titanium target. Since the deuteron stops very quickly compared to the Larmor precession period, depolarization is not expected to affect the results.

An investigation of depolarization effects below 100 keV has been previously performed, [Lan89]. In this measurement, 3.375 MeV deuterons were degraded to 800 keV with a 25.4 μm Havar foil. The deuterons passed through deuterium gas and impinged upon a Tritiated-Titanium target. The pressure of the gas was adjusted to achieve the desired deuteron energy at the Tritiated-Titanium target. The polarization of neutrons from the ^{3}H(d,n)^{4}He reaction was measured as a function of deuteron energy. No depolarization was observed for deuteron energies below 100 keV.

4.7 Results

The results obtained for the vector and tensor analyzing powers $A_y(\theta)$ and $A_{yy}(\theta)$ at E_d(lab) = 80 - 0 keV are given in Table 4.7.1 and shown in Figure 4.7.1. Accidental and dead-time corrections have been applied to the data. The indicated errors represent

the statistical uncertainty of the data. (The finite geometry corrected data are given in Appendix C.) The vector analyzing power $A_y(\theta)$ is small, negative, and almost consistent with zero; the tensor analyzing power $A_{yy}(\theta$ is negative and approximately -0.25. Recalling the results for the differential cross section, we see that the reaction clearly does not proceed solely via s-wave E2 capture to the D-state since the cross section is *not* isotropic and $A_{yy}(\theta)$ is *not* +0.25. The next chapter focuses on the extraction of the transition strengths involved in the reaction.

θ_{cm} (deg.)	$A_y(\theta) \pm \Delta A_y(\theta)$	$A_{yy}(\theta) \pm \Delta A_{yy}(\theta)$
0.	0.020 ± 0.140	-0.232 ± 0.082
45.	-0.255 ± 0.200	-0.333 ± 0.121
82.	-0.078 ± 0.202	-0.194 ± 0.109

TABLE 4.7.1 Results obtained for the angular distribution of vector and tensor analyzing powers $A_y(\theta)$ and $A_{yy}(\theta)$ for the $^2H(d,\gamma)^4He$ reaction at $E_d(lab)$ = 80 - 0 keV. The uncertainties represent the statistical errors associated with the data points.

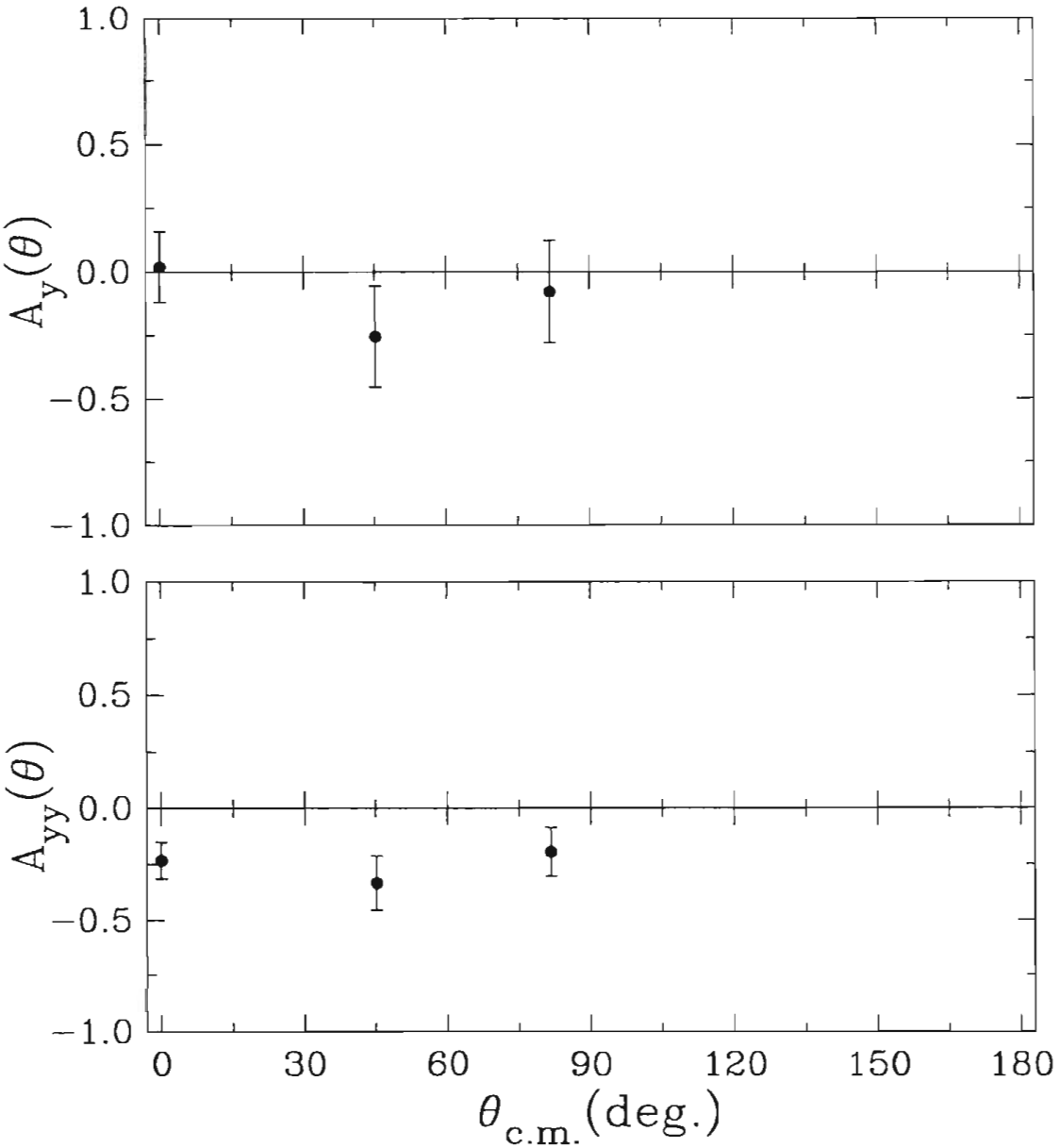

FIG. 4.7.1 Results obtained for the angular distribution of vector and tensor analyzing powers $A_y(\theta)$ and $A_{yy}(\theta)$ for the $^2H(d,\gamma)^4He$ reaction at $E_d(lab)$ = 80 - 0 keV. The uncertainties represent the statistical errors associated with the data points.

CHAPTER 5

Transition Matrix Element Analysis

5.1 Introduction

We now proceed to extract information on the transitions involved in the $^2H(\vec{d},\gamma)^4He$ reaction at low energies. This is accomplished through a model-independent transition matrix element (TME) analysis based on the formalism of [Sey79]. Here, the cross section and analyzing powers are expressed in terms of reduced transition matrix elements. A χ^2-minimization routine is used to fit all of the measured observables simultaneously in terms of the TME's.

5.2 Allowed Transitions

There are eight partial wave amplitudes of multipolarity $\lambda \leq 2$ in the $^2H(d,\gamma)^4He$ reaction and seven undetermined relative phases, forming a set of 15 parameters with which to fit the data. Unfortunately, the data set is limited, so several transition amplitudes are neglected. The centrifugal barrier greatly suppresses the $\ell = 2$, 3, and 4

partial waves. The $\ell = 2$ penetrability factor is about three orders of magnitude smaller than the $\ell = 1$ factor, and the $\ell = 3$ and 4 factors are much smaller than the $\ell = 2$ factor, hence the $\ell = 2$, 3, and 4 amplitudes are neglected in the TME analysis. The remaining parameters are the $^5s_2$(E2), $^3p_1$(E1), and $^3p_2$(M2) transitions. (The notation $^{2S+1}\ell_J$ is used to identify the quantum numbers of the continuum state.) These transitions are then used in the analysis.

5.3 Theory of the Transition Matrix Element Analysis

The differential cross section for a spin-1 tensor polarized beam can be described in terms of vector and tensor moments

$$\sigma(\theta,\phi) = \sigma_u(\theta)\left[1 + \tfrac{3}{2}p_y A_y(\theta) + t_{20}T_{20}(\theta) + 2\,\mathrm{Re}\,t_{21}T_{21}(\theta) + 2\,\mathrm{Re}\,t_{22}T_{22}(\theta)\right], \qquad (5.3.1)$$

where p_y and t_{kq} are the vector and tensor beam moments and $A_y(\theta)$ and $T_{kq}(\theta)$ are the vector and tensor analyzing powers. The cross section for a point detector may also be expanded in terms of the Legendre and associated Legendre polynomials

$$\sigma(\theta,\phi) = \sum_k (A_k P_k + B_k P_k^1 p_y + C_k P_k t_{20} + D_k P_k^1 \,\mathrm{Re}\,t_{21} + E_k P_k^2 \,\mathrm{Re}\,t_{22}), \qquad (5.3.2)$$

where P_k^m are the associated Legendre polynomials, and A_k, B_k, C_k, D_k, and E_k, are the related coefficients.

The analyzing powers can be written in terms of the expansion coefficients by comparing eqs. 5.3.1 and 5.3.2. For the unpolarized cross section $\sigma_u(\theta)$, vector analyzing power $A_y(\theta)$, and tensor analyzing power, $A_{yy}(\theta)$, we have

$$\sigma_u(\theta) = \sum_k A_k Q_k P_k(\cos\theta), \tag{5.3.3}$$

$$A_y(\theta)\sigma_u(\theta) = \sum_k \tfrac{2}{3} B_k Q_k P_k^1(\cos\theta), \tag{5.3.4}$$

$$A_{yy}(\theta)\sigma_u(\theta) = \sum_k \tfrac{-1}{\sqrt{2}} C_k Q_k P_k(\cos\theta) + \tfrac{\sqrt{3}}{2} E_k Q_k P_k^2(\cos\theta), \tag{5.3.5}$$

where the relation $A_{yy}(\theta) = \frac{-1}{\sqrt{2}}T_{20}(\theta) + \sqrt{3}T_{22}(\theta)$ has been used. The Q_k terms account for the finite geometry effects of the detector [Ros53]. It should be noted that the C_k and E_k coefficients cannot be extracted in this analysis due to non-orthogonalities, see eq. 5.3.5. This does not present a problem as we want to extract the TME's from which the coefficients are derived.

The Legendre polynomials coefficients can be expressed in terms of the complex reduced transition matrix elements using the formalism of [Sey79]. The TME's are labeled by the continuum state quantum numbers and the multipolarity of the outgoing γ ray. The amplitudes and phases of the TME's can thereby be fit to all observables simultaneously, yielding a model-independent interpretation of the results. The fortran code TMEFIT, using MINUIT function minimization subroutines, was used to perform the TME analysis of the data. The Legendre polynomial expansion in terms of the TME's is given in Appendix A.

5.4 Results of the Transition Matrix Element Analysis

The TME analysis began with the simplest interpretation (fewest matrix elements) of the reaction and proceeded by adding the necessary transition amplitudes to construct a reasonable fit. As previously mentioned, the reaction was expected to be dominated by the $^5s_2$(E2) transition. This is clearly not the case, since $A_{yy}(\theta) \neq +0.25$ and the cross

section is not isotropic. The next step in the TME analysis was to add the $^1d_2$(E2) transition and attempt to fit the data. This resulting fit proved unsatisfactory, so more matrix elements had to be added.

The next strongest transitions are expected to be those involving p-waves, *i.e.* the $^3p_1$(E1) and $^3p_2$(M2) transitions. To minimize the number of fitting parameters, the only E2 amplitude included was the $^5s_2$(E2) transition, since d-waves are expected to be strongly suppressed by the angular momentum barrier. Fits were performed using combinations of E2, E1, and M2 radiative transitions. Satisfactory solutions were not found for fits including E2 and E1 radiation or E2 and M2 radiation. However, a fit including E2, E1, and M2 transitions produced a satisfactory solution. Due to the limited data set, three solutions with similar χ^2 results were found. These results are given in Table 5.4.1 and shown in Figure 5.4.1. The solutions include: (1) dominant E2 (40%) with nearly equal E1 (29%) and M2 (31%) contributions, (2) dominant E2 (49%) with strong E1 contributions (36%), and (3) dominant M2 (73%) with similar E2 (15%) and E1 (12%) contributions. Unfortunately, no one solution can be chosen from the analysis. To determine the best solution, the measurement would have to be performed at back angles where the three solutions differ. This was not feasible as the detector would have to be positioned much farther away from the target than in the current experiment, which would lower the count rate to below acceptable levels. For example, to make a measurement at θ(lab) = 135°, the detector would have to be positioned about 30 cm further from the target than in the present configuration, resulting in a factor of seven decrease in count rate. Fits were also performed with the addition of the E2 $^1d_2$-wave transition. Since the d-wave strength should be strongly suppressed by the angular momentum barrier, the amplitude was constrained to be less than 10% of the cross section. The results of these fits showed that some of the E2 s-wave strength could be

shifted to the d-wave strength, while the E1 and M2 p-wave strength remained essentially unchanged. To summarize, it is evident that the E1/M2 p-wave contribution accounts for more than half of the cross section in contrast to earlier predictions.

Transition	Multipolarity	FIT 1	
		Strengths	Phase
$^5s_2$	E2	39.8 ± 10.2	0°
$^3p_1$	E1	29.0 ± 10.2	-154° ± 39°
$^3p_2$	M2	31.2 ± 21.3	-120° ± 34°
χ^2_ν		0.368	

Transition	Multipolarity	FIT 2		FIT 3	
		Strengths	Phase	Strengths	Phase
$^5s_2$	E2	48.8 ± 7.6	0°	15.3 ± 24.2	0°
$^3p_1$	E1	35.8 ± 5.0	206° ± 24°	12.1 ± 5.1	-26°± 89°
$^3p_2$	M2	15.4 ± 5.7	212° ± 55°	72.6 ± 23.0	-38° ± 51°
χ^2_ν		0.376		0.389	

TABLE 5.4.1 Results of the model-independent transition matrix element analysis for each of the three fits. The transition matrix element strengths are presented as percent contributions to the total cross section; the phases are relative to the $^5s_2$(E2) term which has been arbitrarily set to zero. The notation $^{2S+1}\ell_J$ is used to identify the continuum state quantum numbers. The number of degrees of freedom is taken to be ν = (12 observables - 5 parameters) = 7. The fits are illustrated in Figure 5.4.1.

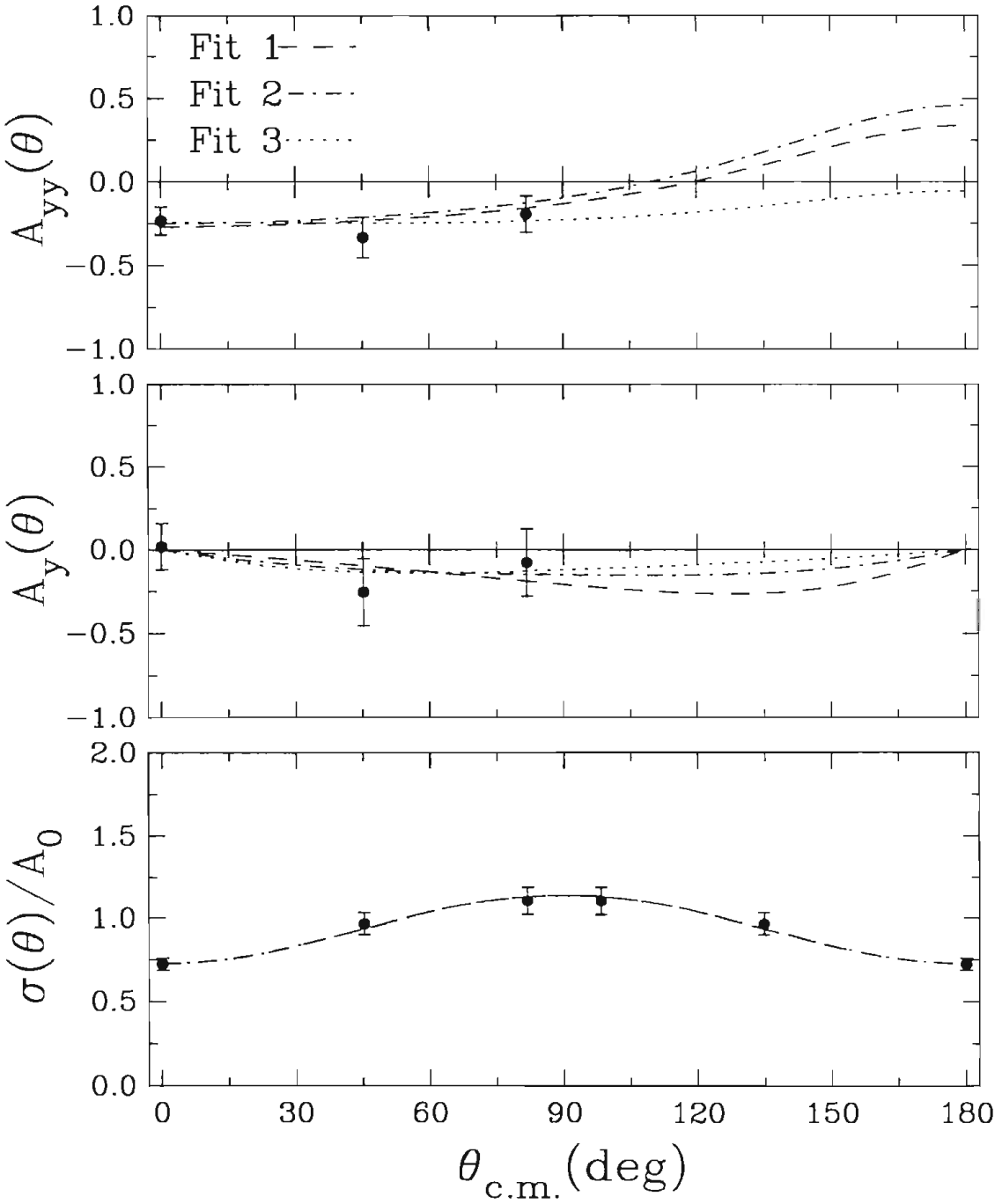

FIG 5.4.1 Results of the model-independent transition matrix element analysis. Three solutions, each of which yields equally good fits, are shown. The three solutions are identical in the $\sigma(\theta)/A_0$ case. The contributions of the various transitions to these fits are summarized in Table 5.4.1. Note the $\sigma(\theta)/A_0$ data have been reflected about $\theta = 90°$.

CHAPTER 6

Theory

6.1 Introduction

This chapter focuses on the theoretical understanding of the $^2H(d,\gamma)^4He$ reaction at low energies. This understanding is strongly affected by the fact that there have been no previous polarization measurements below E_d(lab) = 500 keV. As a result, most interpretations of data in this energy region assume that the reaction is dominated by E2 $^5S_2$-wave capture to the $^5D_0$ state. The current measurement does not support this assumption, although earlier models have reproduced the previous unpolarized data well. The goal is to understand the reaction mechanism in light of the current results.

We begin by examining several direct capture calculations. These calculations describe the capture reaction in terms of a simple one-step direct process. The calculations differ in their description of the incoming and outgoing channels – from point particle wave functions to more complex microscopic wave functions. These calculations show the importance of including the structure of the participating particles.

Next, a recent resonating group model calculation is examined. This model has the advantage over direct capture models of including the p-^{3}H and n-^{3}He channels in the calculation. It also includes E1, M2, and M1 in addition to E2 radiative transitions. As will be seen, the addition of the extra channels and multipolarities proves crucial to describing the ^{2}H(d,γ)^{4}He reaction at E_d(lab) = 80 keV. Finally, several mechanisms which may create the large p-wave strength observed in our experiment are examined. This interpretation leads to a possible explanation of the large p-wave strengths observed in the reaction.

6.1 Direct Capture Calculations

Direct capture reaction theory describes the ^{2}H(d,γ)^{4}He reaction through transitions between initial continuum states and final bound states as a one-step process. The transition is accomplished via an interaction with the electromagnetic field. The transition can be written as

$$\langle \psi_f | H_{int} | \psi_i \rangle, \tag{6.1.1}$$

where H_{int} is the interaction Hamiltonian.

In its simplest form, the direct capture model assumes point deuterons. Here, the ^{4}He ground state wave functions are constructed from a Woods-Saxon potential where the depth of the potential is adjusted to reproduce the experimental d-d binding energy. The continuum wave functions are also calculated from a Woods-Saxon potential, where the parameters are taken from optical model fits to elastic scattering. Improvements can be made in generating the wave functions, for example, using a resonating group model to create the wave functions. The improvements can show the sensitivity of the calculation to the wave function parameterization.

The first direct capture calculation of the $^2H(d,\gamma)^4He$ reaction at low energies was performed in conjunction with the first low energy cross section measurement [Wil85]. Here, the Γ_γ/Γ_p branching ratio was measured for incident deuteron energies of 50 - 150 keV. The data showed a flat branching ratio, although earlier predictions indicated that the branching ratio decreased at lower energy. A simple model was then used to interpret the results. It was found that the branching ratios could be reproduced by assuming a dominant E2 process, with an admixture of M1 radiation. The M1 radiation results from capture to the $^5D_0$ final state from the $^5d_1$ continuum state. The angular momentum barrier should strongly suppress the d-wave capture. As we shall see, later calculations refute the M1 contributions.

An investigation of the ^{4}He D-state was performed by Weller, *et al.* [Wel86] who measured the cross section between $E_d(lab) = 0.7$ - 15 MeV. A direct capture calculation was carried out in order to extract the asymptotic D-to-S state ratio, ρ. The asymptotic D-to-S state ratio is defined as

$$\rho = \frac{N_2}{N_0}, \tag{6.1.2}$$

where N_2 and N_0 are the coefficients of the asymptotic form of the radial wave function given by

$$u_L(r) \underset{r\to\infty}{\to} -N_L\, i^L h_L(i\alpha r), \tag{6.1.3}$$

where α is the wave number corresponding to the separation of two deuterons from ^{4}He and $h_L(i\alpha r)$ is a spherical Hankel function of the first kind. In this investigation, only E2 transitions were considered, since the reaction was expected to proceed predominantly by E2 transitions. The scattering state wave functions were generated from separable potentials constructed to reproduce phase shifts obtained from a resonating group model calculation which described the elastic scattering data. The bound state was taken to be a

dominant S-state with an admixture of D-state. The bound states were generated with a Woods-Saxon potential where the potential depth was adjusted to give the correct d-d binding energy. The calculation included $^1d_2$-wave E2 capture to the $^1S_0$ state and $^5s_2$-, $^5d_2$-, and ^5s_g-wave E2 capture to the $^5D_0$ state. The results of the calculation found the asymptotic D-to-S state ratio to be in the range $-0.25 < \rho < -0.15$. The calculation also showed that the low energy cross section resulted predominately from E2 $^5s_2$-wave capture to the $^5D_0$ state.

Another low energy measurement and calculation was done by Barnes, *et al.* [Bar87]. The cross section and angular distribution was measured between E_d(lab) = 100 - 1000 keV. The angular distribution data at E_d(lab) = 150 keV showed an isotropic cross section. Again, this was interpreted as resulting from dominant E2 $^5s_2$-wave capture to the $^5D_0$ state. A direct capture calculation assuming point deuterons was carried out to estimate the magnitude of the D-state admixture. The resulting D-state probability was found to be (1.4 ± 0.8)%. This result was not considered reliable, as the calculation was thought to be over simplified.

To investigate the dependence of the low energy capture cross sections on the potential parameterizations of direct capture calculations, Blüge, *et al.* [Blü87] calculated low energy cross sections using several potentials. Wave functions created using the previously mentioned Woods-Saxon parameterizations (and several not mentioned) were investigated. Most of the parameterizations were based on a Woods-Saxon potential which reproduced microscopic resonating group model phase shifts that describe the low energy d-d scattering. Only E2 radiative transitions were included in the calculations. It was found that slight changes in the parameters could create drastic changes in the cross section predictions. Therefore, quantitative statements about derived quantities (*i.e.* D-state parameters) were considered unreliable. These same authors noted that including

the effects of the n-^{3}He and p-^{3}H channels, as well as the deuteron D-state, may be important in an accurate description of this reaction. With this in mind, we now consider several more sophisticated models.

Piekarewicz and Koonin studied the effect of the deuteron D-state in a simple phenomenological model [Pie87]. Both the scattering-state and bound-state wave functions, as well as the E2 electromagnetic operator, explicitly included the internal coordinates of the deuteron. Transitions from the $^5s_2$- and $^1d_2$-scattering states to the $^1S_0$- and $^5D_0$-bound states were included in the calculation. The $^5s_2$ to $^1S_0$ transition is made possible by the inclusion of the deuteron D-state in the calculation. Results showed that this transition is important in determining the cross section at low energies (below 1 MeV), where it interferes with the $^5s_2$ to $^5D_0$ capture. The resulting asymptotic D-to-S state ratio was found to be twice as large as in earlier calculations. However, another group performed an improved microscopic calculation including the deuteron D-state and found good agreement with data using a value of ρ = -0.18 [Arr88]. These authors suggest that the large value of ρ in [Pie87] is a consequence of approximations involved in their method for including the effects of the deuteron D-state. These investigations have shown the importance of the deuteron D-state in the ^{2}H(d,γ)^{4}He reaction at low energies.

The reaction was also studied with a microscopic description of the wave functions by Assenbaum and Langanke [Ass87]. The bound state wave functions were derived from anti-symmeterized nucleon-nucleon wave functions in a nucleon-nucleon interaction containing central, spin-orbit, and tensor terms. Both shell model and d-d cluster states were included. The wave functions were found by employing the variational method to solve the four-particle Schrödinger equation. The scattering states were taken to be the anti-symmeterized d-d cluster wave functions. The initial and final

states were thus constructed consistently. E2 transitions from the $^5s_2$ state to the $^5D_0$ state and from the $^1d_2$ state to the $^1S_0$ state were included in the calculation. The results agreed well the measured cross section and predicted a D-state admixture of 5 - 7%.

Finally, a recent calculation using Variational Monte Carlo techniques has been used to study the reaction for deuteron laboratory energies below 1 MeV [Arr91]. Here, only E2 radiative transitions from the $^5s_2$-continuum state to the ^{4}He ground state were considered since these transitions were expected to dominate in this energy region. One advantage of this treatment is that both initial and final states are derived consistently. The effects of the deuteron and the alpha particle D-states were investigated by calculating the total cross section with and without both D-states included. Agreement with the experimental data was less than satisfactory. However, the results showed that the calculation was sensitive to both the deuteron and ^{4}He D-states. An improved calculation, including better wave functions and more transitions, is in progress. Hopefully, this may lead to a better understanding of the reaction.

In summary, we have seen that various refinements have been made to the direct capture calculations. It seems clear that details of the wave functions, including the deuteron D-state, are quite important in extracting reliable results. Unfortunately, these models have all assumed E2 capture dominated by $^5s_2$-wave capture to the $^5D_0$ state. The present data contradicts that assumption. We now move on to a more sophisticated calculation which does not make this assumption and which takes the coupling to the n-^{3}He and p-^{3}H channels into account.

6.3 Resonating Group Model Calculation

The $^2H(d,\gamma)^4He$ reaction has been examined in terms of a microscopic coupled-channel resonating group model (MCCRGM) by Hofmann, *et al.* [Wac88], [Kel89]. In resonating group models the system is described using an expansion in terms of a collection of cluster wave functions. These wave functions include the substructure of the clusters, resulting in a microscopic description of the system. The formalism also allows for many channels to be included in the calculation. In the ^4He case, both the n-^3He and p-^3H channels are included in addition to the d-d channel. Hofmann points out that since the charge radius of the deuterons is larger than that of the ^4He nucleus, proper anti-symmeterization of the ^4He wave function destroys the identity of the deuterons, and hence, the need to include the extra channels [Wac88]. The wave functions were generated by employing the variational method and searching for the minimum energy. The continuum and bound state wave functions were consistently derived from nucleon-nucleon potentials including Coulomb, central, spin-orbit, and tensor forces, where the strengths of the spin-orbit and tensor forces were adjusted to reproduce two-nucleon scattering phase shifts. As mentioned, the wave functions consisted of p-^3H, n-^3He, and d-d components. Only s-, p-, and d-continuum waves were considered and the ground state was a linear combination of $^1S_0$ (^3H,p), $^1S_0$ (^3He,n), $^1S_0$ (d,d), and $^5D_0$ (d,d) components. Transitions via E2, E1, M2, and M1 radiation were included in the long wavelength approximation.

The wave functions were generated from two different nucleon-nucleon potentials, a semi-realistic potential and a realistic potential. The realistic potential is the r-space version of the one-boson-exchange full Bonn potential expressed in terms of Gaussians [Kel89]. It has a soft core with a few GeV repulsion at the origin. D-states were included in all of the fragments in the realistic potential – d, ^3He, and ^3H. The

D-state admixture in the deuteron is 4.8% and the total non-S = 0 contribution to the ^{4}He ground state which this leads to is between 12 - 13%. It should be noted that this does not mean that the total D-state is between 12 - 13 %. Consider the D-state of a fragment coupled to the relative D-state between fragments, creating an S = 0 state. This cannot be distinguished from the usual S-state because it is not orthogonal. Hence, the 12 - 13% value is a lower limit to the total D-state.

The semi-realistic potential is derived from the potential given by [Eik71], but with the strong core reduced to 200 MeV. This is done for the central term only, the remaining terms are essentially unchanged. The advantage here is that the smaller core allows the deuteron to be bound by pure s-waves, simplifying the calculation. As a result, the internal wave functions of the fragments contain only s-waves. The disadvantage is that the calculated d-d threshold is too low (by about 2 MeV [Hof81]), and the nearby 1^- and 2^- resonances contribute more than in reality. One of the motivations for utilizing the realistic potential was that it reproduces the thresholds and resonance positions correctly. For the semi-realistic potential, the effective two-body force predicted a 6.2% D-state probability for the deuteron and, through the MCCRGM calculation, it predicted a 2.2% D-state probability for the ^{4}He ground state. Note that for the ^{4}He nucleus this only represents the D-state associated with the L = 2 relative motion of the two s-state deuterons and is not the total ^{4}He D-state probability. It should also be noted that the D-state in these two potentials are not necessarily inconsistent, since inclusion of the deuteron D-state in the semi-realistic potential would raise the total D-state to around 12 - 15%.

The semi-realistic potential has been used to interpret data at higher energies. At E_d(lab) = 10 MeV, the model was shown to reproduce the data well [Wac88]. It was found that most of the contribution to the matrix elements came from coupling to the

n-^{3}He and p-^{3}H channels and it was suggested that direct capture calculations are not reliable because they do not include these channels. The authors also found that changing the ^{4}He D-state from 2.2% to 12% had little effect on the observables, and concluded that extracting the ^{4}He D-state is not as simple as once believed. It should be noted that this conclusion may not necessarily follow because the D-state was adjusted inconsistently in the model. The total D-state was increased by boosting the contribution from the D-state portion of the ^{4}He ground state wave function. A better method would have been to increase the two-body tensor force strength which, in turn, would increase the total D-state in a consistent manner, affecting the binding energy and therefore the asymptotic D-to-S state ratio. This may explain why the observables seemed insensitive to changes in the D-state in [Wac88].

The MCCRGM using the semi-realistic potential has also been successful at predicting observables below E_d(lab) = 3 MeV [Lan88], [Lan90]. It gives a total cross section near the measured values, without having to include any normalization factors. The model also gives a fair representation of the polarized data at E_d(lab) = 1.2 MeV and E_d(lab) $\leq$ 0.8 MeV. Even at these energies, it predicts large p-wave capture strength, about 30% $^3p_1$ (E1) and about 25% $^3p_2$ (M2).

Results of the MCCRGM calculation including both potentials are given in Table 6.3.1 and shown in Figure 6.3.1 along with the experimental data. Although the realistic potential is by many measures deemed to be superior to the semi-realistic potential, the semi-realistic potential produces the best agreement with data. The semi-realistic potential does a fair job of describing the analyzing powers $A_y(\theta)$ and $A_{yy}(\theta)$, although the angular distribution of the cross section $\sigma(\theta)/A_0$ is poorly described, especially at extreme angles. While the calculation at this energy has a significant E2 component (39%), there are also large E1 (30%) and M2 (31%) contributions. It is interesting to

note that the calculated transition strengths resemble one of the TME analysis results (FIT 1), although the relative phases do not agree. The realistic potential predicts dominant s-wave E2 strength (75%) with only 12% E1 and 9% M2 radiation. The tensor analyzing power $A_{yy}(\theta)$ is predicted to be near +0.25 and the vector analyzing power $A_y(\theta)$ is near zero. This is a consequence of the large s-wave E2 contribution. We have no explanation for this discrepancy, although it may be related to the tensor force in the Bonn potential. The strength of the tensor force in the Bonn potential is reduced compared to conventional descriptions, which is demonstrated by the deuteron D-state and ε_1 mixing parameter. The model predicts only a 4.8% D-state probability for the deuteron, which is on the low side of the generally accepted value of 4 - 7%. There are also discrepancies with the ε_1 mixing parameter, which gives the $^3S_1$ - $^3D_1$ admixture and is related to the tensor force. If the tensor force is important in this reaction, then the reduced tensor force in the Bonn potential (and therefore the realistic MCCRGM) may lead to the poor agreement of the realistic MCCRGM calculation with the experimental data. Nonetheless, the data make it clear that large p-waves are present in the $^2H(d,\gamma)^4He$ reaction at $E_d(lab)$ = 80 - 0 keV.

	Semi-Realistic Potential		Realistic Potential	
Transition	Cross Section (%)	Relative Phase	Cross Section (%)	Relative Phase
$^1d_2$ (E2)	0.9	-104.90°	3.8	131.56°
$^5s_2$ (E2)	38.2	0.00°	75.3	0.00°
$^5d_2$ (E2)	0.1	-68.52°	–	–
$^3p_1$ (E1)	29.8	-146.16°	12.3	101.82°
$^3p_2$ (M2)	30.9	-55.10°	8.6	-117.40°
$^5d_1$ (M1)	<0.1	112.48°	–	–

TABLE 6.3.1 The transition matrix element (TME) strengths from the microscopic coupled-channel resonating group model calculation for both the semi-realistic and realistic potentials given as a percentage of the total cross section and phases relative to the $^5s_2$(E2) term. The notation $^{2S+1}\ell_J$ is used to identify the scattering state quantum numbers. The results are illustrated in Figure 6.3.1.

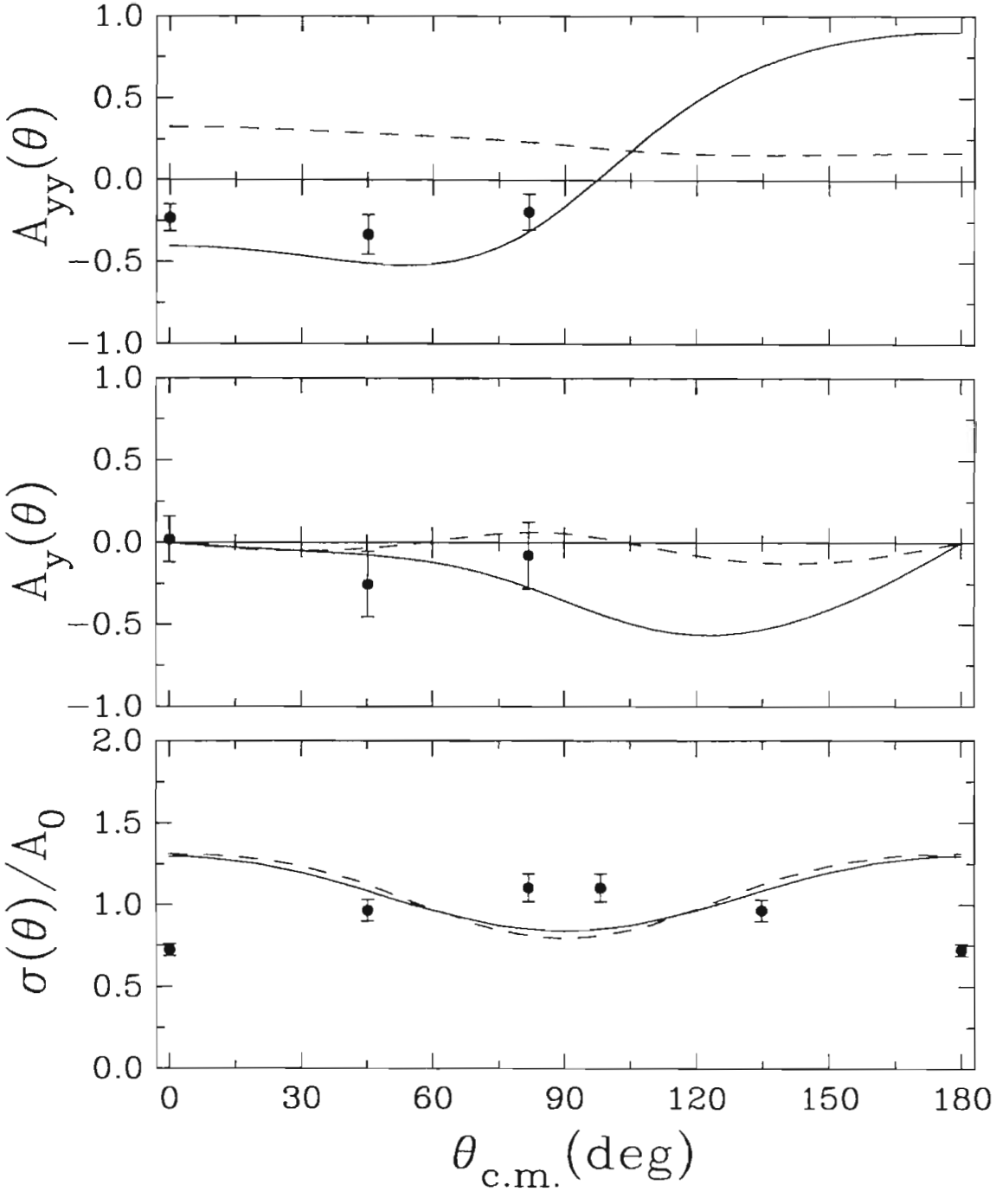

FIG. 6.3.1 The results of the microscopic coupled-channel resonating group model calculation compared to the experimental data. Results are for the differential cross section and analyzing powers calculated for both the semi-realistic (solid) and realistic potentials (dashed). The contributions of the various transitions are given in Table 6.3.1.

6.4 Mechanisms for Enhanced p-waves.

We now examine two mechanisms which may be responsible for the large p-wave strength found in the reaction. First, the behavior of the Coulomb wave functions and penetrabilities is examined in our energy region. At very low energies, the angular momentum dependence of the Coulomb functions goes away, so the s- and p-waves can be of similar magnitude. The tensor force is also examined as a possible source of the p-wave strength.

It has long been established that the Coulomb wave functions have no ℓ dependence at low energies [Bie55]. This behavior results from the fact that at large radii (*i.e.* low energy) the angular momentum barrier is negligible to the Coulomb barrier. We therefore have examined the Coulomb barrier penetrability factors below E_d(lab) = 100 keV for the ^{2}H(d,γ)^{4}He reaction, which are illustrated in Figure 6.4.1. Penetrabilities are derived from the regular and irregular Coulomb wave functions, explicitly

$$P_\ell(kr) = \frac{kr}{F_\ell(kr)^2 + G_\ell(kr)^2}, \qquad (6.4.1)$$

where $P_\ell(kr)$ is the penetrability, $F_\ell(kr)$ and $G_\ell(kr)$ are the regular and irregular Coulomb functions, k is the wave number, r is the matching radius, and ℓ is the angular momentum quantum number. As can be seen in the figure, the ℓ = 1 penetrabilities are smaller than the ℓ = 0 penetrabilities. At 80 keV this ratio is 12. At lower energies, the factor increases to 39 at 1 keV. At low enough energies, the ratio decreases and eventually reaches 1. We can observe the lack of ℓ dependence by considering two ^{20}Ne particles. In this case, the ratio of penetrabilities is flat below about 1 MeV, illustrating the independence of ℓ. If a matching radius of 30 fm is used for the ^{4}He case at 80 keV, then

this argument would hold, however this radius is unphysical. As stated in [Bie55], the Sommerfeld parameter η must be large for the Coulomb functions to be independent of ℓ. At 80 keV, $\eta = 0.79$, so ℓ independence should not be expected. We therefore conclude that the penetrabilities alone cannot be used to explain the large p-wave strength.

The tensor force, however, may provide an explanation of the large p-wave strength. The tensor force can allow for coupling between the S = 0 and S = 1 incident deuteron channels and also coupling between the d-d, n-^{3}He, and p-^{3}H channels. This coupling would allow for E1 and M2 p-wave transitions. The tensor force in addition to spin-flip E1 may then be the mechanism which enhances the p-wave strength in the ^{2}H(d,γ)^{4}He reaction. A full coupled-channel calculation which varies the tensor force should be undertaken to determine if the tensor force is responsible for the large p-wave strength in the reaction.

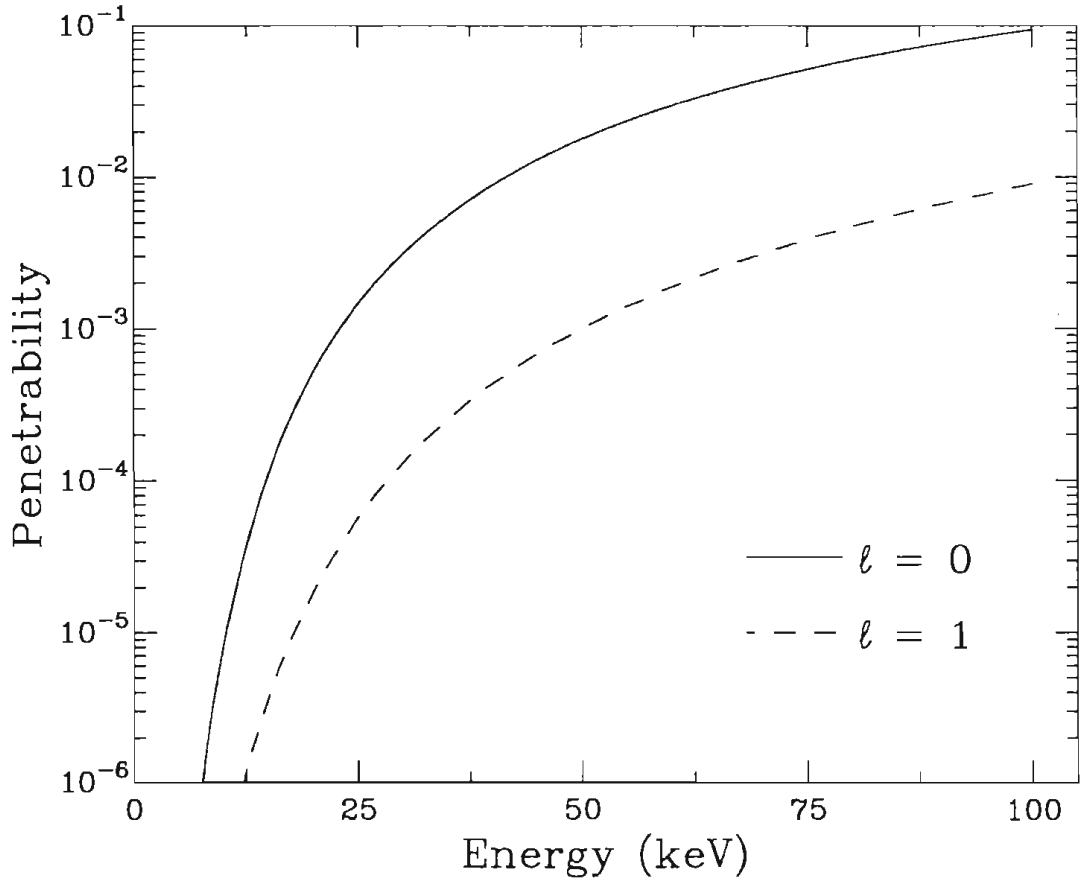

FIG. 6.4.1 Penetrabilities for the $^{2}H(d,\gamma)^{4}He$ reaction below E_d(lab) = 100 keV. A matching radius of 8.6 fm was used in the calculation.

CHAPTER 7

Conclusion

The differential cross section and vector and tensor analyzing powers for the $^2H(d,\gamma)^4He$ reaction have been measured at $E_d(lab) = 80 - 0$ keV and $\theta = 0°$, 45°, and 82°. Our results lead to the conclusion that over 50% of the cross section strength at these low energies is due to p-wave capture, in sharp contrast to previous assumptions of dominant s-wave E2 capture.

A transition matrix element analysis has been performed and three solutions with nearly-identical χ^2 were found. The solutions indicate that over 50% of the capture strength results from p-wave E1/M2 capture. The remaining strength results from E2 $^5s_2$-wave capture. This observed p-wave strength is unexpectedly large.

The data were compared to a microscopic coupled-channel resonating group model calculation, which included the d-d, p-^{3}H, and n-^{3}He channels and E2, E1, M2, and M1 radiation. These calculations included wave functions calculated from two potentials, a semi-realistic and a realistic potential. The semi-realistic potential was found to give the best agreement with data. The semi-realistic potential included large p-wave strength which resulted from the inclusion of the p-^{3}H and n-^{3}He channels. The agreement is somewhat puzzling, as the semi-realistic potential is expected to include too

much p-wave strength as a result of incorrectly positioned thresholds and resonances. The realistic potential corrects these problems, but fails to predict the experimental results. The origin of this discrepancy is not understood, although it may result from an underestimated tensor force in this particular model of the two-nucleon force. Nonetheless, it is clear from the data that p-waves play an important role in the $^2H(d,\gamma)^4He$ reaction.

An attempt was made to understand the origin of the large p-wave strengths found in the reaction in terms of the Coulomb wave functions and penetrabilities, although this approach proved to be unplausible. The tensor force may be responsible for the large p-waves through coupling to other channels. More calculations are needed to verify this hypothesis.

The astrophysical S-factor is the total cross section with Coulomb barrier effects removed, explicitly

$$S(E) = \sigma(E)\, E\, e^{2\pi\eta}, \qquad (7.1)$$

where $\sigma(E)$ is the total cross section, E is the center of mass energy, and η is the Sommerfeld parameter. Recent studies of the low energy $^2H(d,\gamma)^4He$ cross section have lead to a factor of 32 enhancement in S(0) over previous values based on the extrapolation of higher energy data. This enhancement has been attributed to $^5s_2$-wave E2 capture to the $^5D_0$-state of ^4He. As we have seen, this assumption is not supported by our results. We find the $^2H(d,\gamma)^4He$ reaction to be dominated by $^3p_1$ (E1) and $^3p_2$ (M2) capture below $E_d(lab) = 80$ keV. Previous conclusions regarding the D-state probability in ^4He, the asymptotic D-to-S state ratio, and the astrophysical S factor must be re-evaluated in light of these findings.

Appendix A

Transition Matrix Element Coefficients

Below are the transition matrix element coefficients which are used to generate the Legendre polynomial coefficients and used in the analysis of the experiment. The polynomial coefficients are calculated by combining two matrix elements and multiplying by the given coefficient, explicitly

$$A_k, C_k, E_k = (\text{coefficient})\ (\text{TME})\ (\text{TME})'\cos(\theta' - \theta), \qquad (A.1)$$

$$B_k = (\text{coefficient})\ (\text{TME})\ (\text{TME})'\sin(\theta' - \theta), \qquad (A.2)$$

The coefficients in the table are identified by the quantum numbers and multipolarity of the two transition matrix elements to be combined.

Coefficient	Value	Mult.	2S+1	2ℓ+1	2J+1	Mult.	2S+1	2ℓ+1	2J+1
A0	3.000	E1	3	3	3	E1	3	3	3
A0	5.000	E2	1	5	5	E2	1	5	5
A0	5.000	E2	5	1	5	E2	5	1	5
A0	5.000	M2	3	3	5	M2	3	3	5
A2	1.500	E1	3	3	3	E1	3	3	3
A2	-11.619	E1	3	3	3	M2	3	3	5
A2	3.571	E2	1	5	5	E2	1	5	5

A2	2.500	M2	3	3	5	M2	3	3	5
A4	-8.571	E2	1	5	5	E2	1	5	5
B1	-4.500	E1	3	3	3	E2	1	5	5
B1	-3.558	E1	3	3	3	E2	5	1	5
B1	-5.809	E2	1	5	5	M2	3	3	5
B1	4.593	E2	5	1	5	M2	3	3	5
B2	2.905	E1	3	3	3	M2	3	3	5
B3	-3.000	E1	3	3	3	E2	1	5	5
B3	-3.873	E2	1	5	5	M2	3	3	5
C0	-1.061	E1	3	3	3	E1	3	3	3
C0	4.472	E2	5	1	5	E2	1	5	5
C0	0.354	M2	3	3	5	M2	3	3	5
C1	-6.037	E1	3	3	3	E2	5	1	5
C1	2.598	E2	5	1	5	M2	3	3	5
C2	-0.530	E1	3	3	3	E1	3	3	3
C2	4.108	E1	3	3	3	M2	3	3	5
C2	3.194	E2	5	1	5	E2	1	5	5
C2	-1.768	E2	5	1	5	E2	5	1	5
C2	0.631	M2	3	3	5	M2	3	3	5
C3	-4.025	E1	3	3	3	E2	5	1	5
C3	10.392	E2	5	1	5	M2	3	3	5
C4	-7.667	E2	5	1	5	E2	1	5	5
C4	-3.637	M2	3	3	5	M2	3	3	5
E2	0.650	E1	3	3	3	E1	3	3	3
E2	1.677	E1	3	3	3	M2	3	3	5
E2	-1.304	E2	5	1	5	E2	1	5	5
E2	-0.722	E2	5	1	5	E2	5	1	5
E2	0.464	M2	3	3	5	M2	3	3	5
E3	-0.548	E1	3	3	3	E2	5	1	5
E3	1.414	E2	5	1	5	M2	3	3	5
E4	-0.522	E2	5	1	5	E2	1	5	5
E4	-0.247	M2	3	3	5	M2	3	3	5

Appendix B

Computer Source Code

B.1 Spectrum Fitting Code - RAWFIT_LB

As discussed in Section 3.4, the pulse height distributions were fit to a response function plus a background function. The response function was the measured line shape plus three fitting parameters including the height, width, and peak position. The background fitting function was an exponential with quadratic argument. The computer source code used to perform the fits follows. The code is a subroutine which is called by the MINUIT function minimization routine. Spectra data are input and output directly from the XSYS data areas. Other input information, such as the fitting region and line-shape parameters, are read from disk files. Sample input and output files are given following the source code.

```
      SUBROUTINE FCN(NPAR, DERIV, CHISQ, X, IFLAG)
C  Gamma-ray Spectrum Fitting Routine which utilizes MINUIT.  Fits spectrum
C    with one peak to a lineshape plus background.  Lineshape function is the
C    standard lineshape ( exponentials of polynomials ) with height, width,
C    and peak position fitting parameters.  The background is an exponential
C    of polynomials.  Utilizes XSYS routines to import/export data to/from
C    data areas.
```

```
C                                        by Laird Kramer, 9/91
C
C  Background function defined as:
C               EXP(X(1) + Z * X(2) + Z^2 * X(3) + Z^3 * X(4) + Z^4 * X(5))
C  in the region defined by IBEGIN - IEND
C
C  Lineshape function defined as:
C               X(6)*EXP(A1 + B1*ZP + C1*ZP*ZP + D1*ZP*ZP*ZP + E1*ZP*ZP*ZP*ZP)
C                                                 for ZP < JNT
C               X(6)*EXP(A2 + B2*ZP + C2*ZP*ZP + D2*ZP*ZP*ZP + E2*ZP*ZP*ZP*ZP)
C                                                 for ZP > JNT
C  where ZP = ( A_CALIB * Z + B_CALIB - X(7) ) / X(8) + STCEN
C  and X(7) and X(8) are normailized by STHEI and STWID
C  Lineshape is given a linear tail below exponential region
C
C  Minuit subroutine inputs:
C    NPAR  = Number of adjustable parameters
C    DERIV = Derivative vector    -- not used here --
C    CHISQ = Value of function to be minimized
C    X     = Parameter vector
C    IFLAG = Control marker 1: Initializing entry, set up constants
C                           2: Entry with gradient    -- not used here --
C                           3: Terminating entry, write output
C                           4: Entry without gradient, calc. F(X), ie CHI-SQR
C                          >4: Not used
C
C=======================================================================

        INCLUDE 'XSYSDIR:XSCOM.FOR/NOLIST'
        INCLUDE 'XSYSDIR:XERRDEF.FOR/NOLIST'

        REAL*8 X(50), DERIV(50)          ! Parameter arrays
        REAL*8 CHISQ                     ! Chi-squared
        REAL*8 LINE, BKGD, FIT           ! Fitting values
        REAL*8 LS_DATA(512)              ! Lineshape array
        REAL*8 DATA(512)                 ! Spectrum data array
        REAL*8 ERR(512)                  ! Spectrum error array
        REAL*8 A_CALIB, B_CALIB          ! Spectrum calibration parameters
        REAL*8 Z, ZT, RI                 ! Lineshape argument
        REAL*8 A1, B1, C1, D1, E1        ! Lineshape parameters - exp args I
        REAL*8 A2, B2, C2, D2, E2        ! Lineshape parameters - exp args II
        REAL*8 JOINT                     ! Lineshape parameter - joint
        REAL*8 LOWER_BND, UPPER_BND      ! Lineshape parameter - bounds
        REAL*8 STHEI                     ! Standard lineshape height parameter
        REAL*8 STWID                     ! Standard lineshape width parameter
        REAL*8 STCEN                     ! Standard lineshape centroid parameter
        REAL*8 HEIGHT                    ! Lineshape height parameter
        REAL*8 SHIFT                     ! Lineshape peak shifting parameter
        REAL*8 WIDTH                     ! Lineshape width parameter
        REAL*8 SLOPE                     ! Slope of linear tail
        REAL*8 U(50), WERR(50)           ! Common block parameters
```

```
        REAL*8 XS(50), XTS(50), WTS(50) ! Common block parameters

        INTEGER NPAR, IFLAG             ! Minuit parameters
        INTEGER DATA_SP_NUM             ! Input spectrum data area number
        INTEGER LINE_SP_NUM             ! Output lineshape data area number
        INTEGER BKGD_SP_NUM             ! Output background data area number
        INTEGER IEND, IBEGIN            ! Begin, end channels of fit
        INTEGER I, INDEX, IFIX(50)      ! Counters and flags
        INTEGER IPFIX(50), NPFIX        ! Common block parameters

        CHARACTER*7 COMM(10)            ! Comment string

        COMMON /FIX/    IPFIX, XS, XTS, WTS, NPFIX
        COMMON /PAREXN/ U, WERR
        COMMON /KEEP/   DATA, ERR, A_CALIB, B_CALIB, IEND, IBEGIN,
     >                  A1, B1, C1, D1, E1, A2, B2, C2, D2, E2,
     >                  JOINT, LOWER_BND, UPPER_BND, STHEI, STWID,
     >                  STCEN, DATA_SP_NUM, LINE_SP_NUM, BKGD_SP_NUM

        GO TO (10,20,30,40,20), IFLAG

C=======================================================================

C **** Initialization

10      CONTINUE

C **** Read input parameters

        READ(15,*) DATA_SP_NUM, LINE_SP_NUM, BKGD_SP_NUM

        READ(10,*) IBEGIN, IEND
        READ(10,*) B_CALIB, A_CALIB
        READ(10,*) A1, B1, C1, D1, E1
        READ(10,*) A2, B2, C2, D2, E2
        READ(10,*) JOINT, LOWER_BND, UPPER_BND
        READ(10,*) STHEI, STCEN, STWID

C100      FORMAT(4(6X,E15.9,/), 6X,E15.9)
C105      FORMAT(9X,F10.5,//,15X,F8.3,//,15X,F8.3)

C **** Map Global Section

        CALL PARSE
        IF (X_ERR.GT.1) CALL XERROR( %VAL(X_ERR), 'MAPDATA',X_MERR)

C **** Map in Data Area

        CALL MAP(DATA_SP_NUM, X_DATA(1), 'XDATA',INFO,X_MERR,X_ERR)
        IF(X_ERR.GT.1)CALL XERROR (%VAL (X_ERR), 'MOVE',X_MERR)
```

```
        DO I = 1, 512

          DATA(I) = DFLOAT(X_DATA(I))

          IF (DATA(I) .EQ. 0.) THEN
            ERR(I) = 1.0D0
          ELSE
            ERR(I) = DSQRT( DATA(I) )
          ENDIF

        ENDDO

C **** Done Mapping

        RETURN

C=======================================================================

20      RETURN          !  Unused: First Derivative Not Known

C=======================================================================

C **** Final Call to FCN
C        Create Output, Put Spectra in Data Areas

30      CONTINUE

C **** Map Background Into BACK_SP_NUM Data Area

        CALL MAP(BKGD_SP_NUM,R4DATA,'XDATA',INFO,X_MERR,X_ERR)
        IF(X_ERR.GT.1)CALL XERROR (%VAL (X_ERR), 'MOVE',X_MERR)

        DO I = 1, IBEGIN - 1
          R4DATA(I) = 0.
        ENDDO

        DO I = IBEGIN, IEND
          RI = DFLOAT(I)
          R4DATA(I) = SNGL( DEXP(X(1) + X(2)*RI + X(3)*RI*RI +
     >                           X(4)*RI*RI*RI + X(5)*RI*RI*RI*RI ) )
        ENDDO

        DO I = IEND + 1, 512
          R4DATA(I) = 0.
        ENDDO

C **** Generate lineshape and background

        CHISQ  = 0.
        HEIGHT = X(6)
        CENT   = X(7)
```

```
      WIDTH  = X(8)

      DO I = IBEGIN, IEND

        RI = DFLOAT(I)
        BKGD = DEXP(X(1) + X(2)*RI + X(3)*RI*RI +
     >                      X(4)*RI*RI*RI + X(5)*RI*RI*RI*RI)

        Z = ( A_CALIB * I + B_CALIB - CENT ) / (WIDTH / STWID) + STCEN

        IF (( Z .GE. LOWER_BND ) .AND. ( Z .LE. UPPER_BND)) THEN

          IF( Z .LT. JOINT ) THEN
            LS_DATA(I) = HEIGHT * STHEI *
     >              DEXP(A1 + B1*Z + C1*Z*Z + D1*Z*Z*Z + E1*Z*Z*Z*Z)
          ELSE
            LS_DATA(I) = HEIGHT * STHEI *
     >              DEXP(A2 + B2*Z + C2*Z*Z + D2*Z*Z*Z + E2*Z*Z*Z*Z)
          ENDIF

        ELSE

          IF( Z .LT. LOWER_BND ) THEN         ! Linear tail

            SLOPE = HEIGHT * STHEI / LOWER_BND * DEXP(A1 + B1*LOWER_BND +
     >              C1*LOWER_BND**2 + D1*LOWER_BND**3 + E1*LOWER_BND**4)

            LS_DATA(I) = SLOPE * Z

          ELSE

            LS_DATA(I) = 0.

          ENDIF

        ENDIF

        FIT  = BKGD + LS_DATA(I)

        CHISQ = CHISQ + ((DATA(I) - FIT)/ERR(I))**2

      ENDDO

C **** Map Lineshape Into LINE_SP_NUM Data Area

      INDEX = 1 + NPG*128

      CALL MAP(LINE_SP_NUM,R4DATA(INDEX),'XDATA',INFO,X_MERR,X_ERR)
      IF(X_ERR.GT.1)CALL XERROR (%VAL (X_ERR), 'MOVE',X_MERR)

      DO I = 1, IBEGIN - 1
```

```
        R4DATA(I+INDEX-1) = 0.
      ENDDO

      DO I = IBEGIN, IEND
        R4DATA(I+INDEX-1) = SNGL( LS_DATA(I) )
      ENDDO

      DO I = IEND + 1, 512
        R4DATA(I+INDEX-1) = 0.
      ENDDO

      DO I = 1, 50
        IFIX(I) = 0
      ENDDO

      I = 1
299   IF (IPFIX(I) .NE. 0) THEN
        IFIX(IPFIX(I)) = 1
        I = I + 1
        GOTO 299
      ENDIF

      WRITE(20,300) DATA_SP_NUM, LINE_SP_NUM, BKGD_SP_NUM
300     FORMAT(' === LS FIT ===',/'  FIT SPECTRA # ',
     .                I3, /,'  LINESHAPE IN SPECTRA # ', I3,
     .                /,'  BACKGROUND IN SPECTRA # ', I3)

      WRITE(20,310) IBEGIN, IEND
310     FORMAT(/'  GATE:  ', I4, ' TO ', I4,//'  FINAL PARAMETERS:',/)

      DO I = 1, 8

        IF ( IFIX(I) .EQ. 1 ) THEN
          COMM(I) = '*FIXED*'
        ELSE
          COMM(I) = '        '
        ENDIF

      ENDDO

      DO I = 1, 5

        WRITE(20,330) I, X(I), WERR(I), COMM(I)
330       FORMAT('    X(',I1,') = ',E15.8,' +/- ',E15.8,2X,A7)

      ENDDO

        WRITE(20,335) 'HEI ', X(6), WERR(6), COMM(6)
        WRITE(20,335) 'CENT', X(7), WERR(7), COMM(7)
        WRITE(20,335) 'WID ', X(8), WERR(8), COMM(8)
335       FORMAT('    ',A4,' = ',E15.8,' +/- ',E15.8,2X,A7)
```

```
        WRITE(20,340) CHISQ
340       FORMAT(/'  CHI-SQUARED: ', F8.3)

        WRITE(20,350) CHISQ/DFLOAT(IEND - IBEGIN + 1 - NPAR)
350       FORMAT(/'  CHI-SQUARED/DEGREE OF FREEDOM: ', F8.3)

        RETURN

C=======================================================================

C **** Define Minimization Function, CHISQ

40      CHISQ = 0.

        HEIGHT = X(6)
        CENT   = X(7)
        WIDTH  = X(8)

        DO I = IBEGIN, IEND

          RI = DFLOAT(I)
          BKGD = DEXP(X(1) + X(2)*RI + X(3)*RI*RI +
     >                          X(4)*RI*RI*RI + X(5)*RI*RI*RI*RI)

          Z = ( A_CALIB * I + B_CALIB - CENT ) / (WIDTH / STWID) + STCEN

          IF (( Z .GE. LOWER_BND ) .AND. ( Z .LE. UPPER_BND)) THEN

            IF( Z .LT. JOINT ) THEN
              LINE = HEIGHT * STHEI *
     >               DEXP(A1 + B1*Z + C1*Z*Z + D1*Z*Z*Z + E1*Z*Z*Z*Z)
            ELSE
              LINE = HEIGHT * STHEI *
     >               DEXP(A2 + B2*Z + C2*Z*Z + D2*Z*Z*Z + E2*Z*Z*Z*Z)
            ENDIF

          ELSE

            IF( Z .LT. LOWER_BND ) THEN         ! Linear tail

              SLOPE = HEIGHT * STHEI / LOWER_BND * DEXP(A1 + B1*LOWER_BND +
     >                  C1*LOWER_BND**2 + D1*LOWER_BND**3 + E1*LOWER_BND**4)

              LINE = SLOPE * Z

            ELSE

              LINE = 0.

            ENDIF
```

```
  ENDIF

  FIT  = BKGD + LINE

  CHISQ = CHISQ + ((DATA(I) - FIT)/ERR(I))**2

ENDDO

RETURN

END
```

Below are sample input and output files for RAWFIT_LB. Input consists of two files, one for direct input into the program and the other for use by MINUIT. The direct file includes the line-shape parameters, fitting region, and energy calibration. The MINUIT file includes the starting and limit values for the fitting parameters and the MINUIT fitting commands. Spectra data are read directly from the XSYS data areas. Output consists of the file below and resulting fit spectra written to XSYS data areas.

DIRECT INPUT:

```
 214 400
  -0.573
   0.09383
  -0.101495422E+05
   0.18835661E+04
  -0.13090048E+03
   0.40382005E+01
  -0.46645767E-01
   0.30602128E+06
  -0.48598524E+05
   0.28941017E+04
  -0.76593899E+02
   0.76009464E+00
  24.39899
  20.000
  26.000
   1.
  23.38
   2.05
```

MINUIT INPUT:

```
DATA FIT, D+D 80 KEV 0 DEGREES
A     6.5      0.0001
B    -0.013    0.0001
C     0.1E-6   0.1E-6
D     0.0E-6   0.1E-6
E     0.000    0.0001
HEI    0.086   0.001    0.    10.
CEN   22.5     0.001   20.   26.
WID    2.      0.001    0.00  5.

FIX 4
FIX 5
MINIMIZE
HESSE
```

```
MINIMIZE
MINIMIZE
EXIT
```

OUTPUT:

```
=== LS FIT ===
 FIT SPECTRA #  12
 LINESHAPE IN SPECTRA #  22
 BACKGROUND IN SPECTRA #  32

 GATE:   214 TO  400

 FINAL PARAMETERS:

   X(1) =  0.61076115E+01 +/-  0.70854413E-01
   X(2) = -0.17167874E-01 +/-  0.54055734E-03
   X(3) =  0.69259617E-05 +/-  0.94680991E-06
   X(4) =  0.00000000E+00 +/-  0.10000000E-06  *FIXED*
   X(5) =  0.00000000E+00 +/-  0.99999997E-04  *FIXED*
   HEI  =  0.43659143E-01 +/-  0.42273805E-02
   CENT =  0.22331328E+02 +/-  0.47693919E-02
   WID  =  0.19740816E+01 +/-  0.26591427E-02

 CHI-SQUARED:  195.527

 CHI-SQUARED/DEGREE OF FREEDOM:    1.080
```

B.2 Cross Section Energy Dependence Code - DDGTI

As discussed in Section 3.8, the energy dependence of the cross section was investigated by calculating the thick target yield as a function of deuteron beam energy for E_d = 80 - 0 keV. In the calculation, the target was divided up into many thin layers, 5 $\mu g/cm^2$ thick. Energy loss for an 80 keV beam was calculated through the layers using the energy loss method of Anderson and Zeigler [And77]. The relative yields for each layer were then calculated using existing branching ratio and cross section data [Bro90], [Wil85]. Input to the code is the beam energy and a sample output for an 80 keV beam is shown in Table 3.8.1. The computer source code used to perform the fits follows.

```
C     DDGTI  --  Yield for D(d,gamma) for thick target (Ti-D)

      DIMENSION ER(1000),RY(1000),pcy(1000),ryint(1000)

C     50uA per hour gives 1.12E18 deuterons
C     For titanium deuteride, 8.45E16 D-nuclei/cm**2 in 5 ug/cm**2 of Ti
C     Conversion from b to cm**2 = 1.0E-24
C     Conversion to differential cross section from total cross section
C          divide by 4*pi (assuming isotropy)

      DATA C1/1.12E18/,C2/8.45E16/,C3/1.0E-24/,PI/3.14159265/
      C= C1*C2*C3/(4.0*PI)

      NI= 1000

      WRITE(*,*)'DDGTI  --  Yield calculation for D(d,gamma)'
      WRITE(*,*)' Enter beam energy:'
      READ(*,*) EB
      E0= EB

C     Choose titanium target

      IZZ= 22

      DO 100 I=1,NI+1
C       Divide target into 5 ug/cm**2 thick slices
        X1= FLOAT(I-1)*5.0
```

```
        DE1= ENLOSS(X1,E0,2,IZZ)
        E1= E0 - DE1
        IF(E1 .LE. 1.0) GO TO 110
        NAI= I
        ER(I)= E1
        RY(I)= XSECT(E1)*C
        IF(RY(I) .LT. (1.0E-6)*RY(1)) GO TO 110
100   CONTINUE

110   CONTINUE

      YTOT= 0.0
      DO 120 I=1,NAI
        YTOT= YTOT + RY(I)
        ryint(i)= ytot
120   continue

      do 130 i=1,nai
130   pcy(i)= 100.*ryint(i)/ytot

      OPEN(7,FILE='DDGTI.OUT',STATUS='NEW')
      WRITE(7,201) E0,NAI
201   FORMAT(' D(d,gamma) Yield Calculation for Thick Ti-D Target',/,
     1 '    Calculated for successive 5 ug/cm**2 layers of Ti',/,
     2'    Beam energy =',f5.0,' keV',5x,'No. of iterations =',i3,/)
      WRITE(7,203) YTOT
      WRITE(7,205)
205   FORMAT(/,'       E1      Yield     Int Yield    % of Total',/)
      WRITE(7,202) (ER(I),RY(I),ryint(i),pcy(i),I=1,NAI)
202   FORMAT(F10.1,2E12.3,f10.1)
203   FORMAT('    Total yield =',f8.3,' per hour-sr-(50 uA of beam)')
      CLOSE(7)

      STOP
      END


      FUNCTION XSECT(E)
C     CROSS SECTION FOR D(d,gamma)
c     Use total cross section from Brown and Jarmie, PRC 41,1391(1990) for
c     D(d,p) times branching ratio (Wilkinson and Cecil)
c     Energy in keV

      DATA S/55.49/, ALPH/0.001709/,BR/1.2E-7/

      IF(E .LE. 0.0) THEN
         XSECT= 0.0
      ELSE
         XSECT= (2.0*S*(1.0+ALPH*E)/E)*EXP(-44.4021/SQRT(E))*BR
      ENDIF
```

```
      RETURN
      END

      FUNCTION ENLOSS(X,E0,ITYPE,IZZ)
C     CALCULATION OF ENERGY LOSS IN TARGET THICKNESS X
C     USES FUNCTION DEDX(E,ITYPE,IZZ)

      IF(X .LE. 0.0) THEN
         ENLOSS= 0.0
         RETURN
      ENDIF

C     NI = no. of steps in iteration
      NI= 100
      DX= X/FLOAT(NI)
      E= E0

      DO 50 I=1,NI
         DE= DX*DEDX(E,ITYPE,IZZ)
         E= E - DE
         IF(E .LE. 0.0) THEN
             ENLOSS= E0
             RETURN
         ENDIF
50    CONTINUE
      ENLOSS= E0 - E
      RETURN
      END


      FUNCTION DEDX(EI,ITYPE,IZZ)
C     Calc. of dE/dx using Ziegler's equations
c     ITYPE= 1 for protons;  ITYPE= 2 for deuterons
c     Energy in keV
c     IZZ= Z of absorber
c     IZZ= 74 is special case for polyethylene

      DIMENSION A(5,74), C(74)
      DATA A(1,1),A(2,1),A(3,1),A(4,1),A(5,1)/1.262,1.44,242.6,
     1 12000.,0.1159/
      DATA A(1,6),A(2,6),A(3,6),A(4,6),A(5,6)/2.631,2.989,1445.,
     1 957.2,0.02819/
      DATA A(1,22),A(2,22),A(3,22),A(4,22),A(5,22)/4.862,
     1 5.496,5165.,568.5,0.009474/
C     Units of dE/dx are keV/(ug/cm**2)
      DATA C(1),C(6),C(22),C(74)/0.5977,0.05016,0.01183,0.1129/

      NN= 0
      E= EI/FLOAT(ITYPE)
      IZ= IZZ
```

```
C     IZZ= 74 is special case (deuterated polyethylene)
      if((izz.eq.74).and.(NN.eq.0)) IZ= 1

10    IF(E .LT. 10.0) THEN
         S= A(1,IZ)*SQRT(E)
      ELSE
         SL= A(2,IZ)*E**(0.45)
         SH= (A(3,IZ)/E)*ALOG(1.0 + (A(4,IZ)/E) + (A(5,IZ)*E))
         S= 1.0/(1.0/SL + 1.0/SH)
      ENDIF

      IF(IZZ .EQ. 74) THEN
         IF(NN .EQ. 0) THEN
             S1= S
             NN= 1
             IZ= 6
             GO TO 10
         ELSE
             S= 2.0*S1/3.0 + S/3.0
         ENDIF
      ENDIF

      DEDX= S*C(IZZ)

      RETURN
      END
```

Appendix C

Finite Geometry Corrected Data

We now present the finite geometry corrected observables. These can be used to compare theory results to point geometry results. The standard method of presenting this information is to first fit observables with the $Q_k(\theta)$ geometry correction coefficients included and then calculate the observables from the fit parameters without the $Q_k(\theta)$ coefficients. We present results based on the most physical TME analysis fit, FIT 1, given in Section 5.4.

		$\sigma(\theta)/A_0 \pm \Delta\sigma(\theta)/A_0$	$A_y(\theta) \pm \Delta A_y(\theta)$	$A_{yy}(\theta) \pm \Delta A_{yy}(\theta)$
$\theta = 0°$	Measured	0.723 ± 0.037	0.020 ± 0.140	-0.232 ± 0.082
	Corrected	0.552 ± 0.037	0.000 ± 0.140	-0.179 ± 0.082
$\theta = 45°$	Measured	0.964 ± 0.067	-0.255 ± 0.200	-0.333 ± 0.121
	Corrected	0.889 ± 0.067	-0.080 ± 0.200	-0.288 ± 0.121
$\theta = 82°$	Measured	1.103 ± 0.085	-0.078 ± 0.202	-0.194 ± 0.109
	Corrected	1.213 ± 0.085	-0.199 ± 0.202	-0.279 ± 0.109

TABLE C.1 Finite geometry corrected data for the $^2H(\vec{d},\gamma)^4He$ reaction at $E_d(lab)$ = 80 - 0 keV.

Appendix D

The γ ray-Recoil Detector System

D.1 Introduction

We now describe a development project begun at TUNL in 1988. The goal of the project is to measure the vector and tensor analyzing powers of the $^4He(\vec{d},\gamma)^6Li$ and $^1H(\vec{d},\gamma)^3He$ reactions. The challenge in both of these experiments results from the low Q-values of the reactions, which makes it difficult to detect the outgoing γ ray. The recoil nucleus must be detected in coincidence with the γ ray to overcome this problem. A new NaI-recoil detector system has been designed and built and will be used to perform these experiments. Since the experiments become easier at higher beam energies, the project was delayed until the completion of the tandem upgrade at TUNL. As a result, no data have been taken, although several development runs have been completed which demonstrate the feasibility of the detection system.

D.2 Motivation

Motivation to study the $^4He(\vec{d},\gamma)^6Li$ reaction comes from several sources. First, in the d-α cluster model of ^6Li, the ground state is composed of two pieces, $^3S_1$ and $^3D_1$. Since analyzing powers are sensitive to the interference of different partial waves, their measurement should lead to an estimate of the D-state in ^6Li. Second, the reaction is dominated by E2 radiation below $E_d(lab) = 20$ MeV [Rob81], although the differential cross section indicates the presence of some E1 radiation. The origin of this E1 radiation is not fully understood, but it may arise from charge polarization of the incident deuteron by the ^4He target nucleus, as well as from the spin-flip ($\Delta S = 1$) isoscalar part of the E1 operator. The vector analyzing power $A_y(\theta)$ should be sensitive to the interference of the E1 and E2 radiation, providing a means to study the E1 mechanism.

Finally, the ground state of ^6Li and corresponding alpha-deuteron and alpha-neutron-proton scattering states have been investigated theoretically from the viewpoint of three-body models [Leh78], [Leh83]. These models have been successful in describing the static properties of the ground state, *i. e.* the ^6Li magnetic moment and the ^6Li rms radius, as well as elastic α-d scattering. Model calculations show that the α-d component comprises 60% of the ground-state wave function of ^6Li. The model finds the D-state part of α-d cluster wave function to be sensitive to the tensor force in the nucleon-nucleon interaction as well as the $s_{1/2}$ alpha-nucleon interaction.

The motivation to study the analyzing powers of the $^1H(\vec{d},\gamma)^3He$ reaction is also based on the reaction mechanism and a three-body model. First, we hope to measure a complete set of analyzing powers to complement the previous $T_{20}(\theta)$ measurement [Vet85]. Previous work has shown that $T_{20}(\theta)$ is sensitive to the ^3He D-state and the admixture was estimated to be between 5% and 9%. Also Fonseca and Lehman [Fon91] are currently examining the system in terms of a three-body model. Their results indicate

that the ^{3}He D-state is responsible for the tensor analyzing powers. Measurement of all the analyzing powers in conjunction with the three-body results should lead to an understanding of the reaction mechanism.

D.3 Experimental Design

The NaI-recoil experimental setup consists of an anti-coincidence shielded NaI spectrometer, a dipole bending magnet, and a set of fast plastic scintillators, shown in Figure D.3.1. The capture γ rays are detected in the NaI detector, while the recoil nuclei are deflected out of the beam by the dipole magnet and detected in the plastic scintillators. A coincidence requirement is placed upon the γ rays and recoils to identify the desired capture events. The targets for the experiments include solid polyethylene (~1.2 mg/cm^2 thick) for the ^{1}H(d,γ)^{3}He reaction and a liquid nitrogen cooled gas cell for the ^{4}He(d,γ)^{6}Li reaction. One experimental difficulty which arises in the ^{4}He(d,γ)^{6}Li case is that the recoil ^{6}Li nuclei loose a large fraction of their energy in the exit foils; therefore, the thinnest possible foils must be used.

The NaI spectrometer consists of a Bicron 25.4 cm $\times$ 25.4 cm NaI(Tl) detector placed inside a 10.16 cm thick Bicron BC412 plastic anti-coincidence shield. The shield is used to discriminate against unwanted events – those due to cosmic rays, neutrons, and events which did not deposit their full γ-ray energy in the NaI detector. Passive shielding is located around the detectors to further decrease the background. Lead surrounds the detectors, 5.1 cm on top and bottom and 10.2 cm on front and sides, which reduces the γ-ray background. An 0.08 cm thick cadmium sheet is positioned outside of the front and side lead to reduce thermal neutron background. Polyethylene and borated polyethylene, approximately 20 cm thick, is then stacked around the lead and cadmium to reduce the

neutron background. The whole assembly is positioned on a rotating cart to allow for angular distribution measurements.

The recoil detection system consists of a dipole magnet and fast plastic scintillators which are placed inside a large vacuum chamber. The magnet was placed as close to the target assembly as possible (40 cm downstream) to maximize the separation of the recoil particles from the beam at the scintillators. The plastic scintillators were located approximately 180 cm downstream of the target, where the recoils are well separated from the beam. Two thin parallel scintillators were included, the front detected the recoils while the rear provided a veto for scattered deuterons which entered the front detector. The beam was stopped in a tantalum-lined beam dump behind the scintillators. To minimize beam and recoil scattering, the chamber was kept at high vacuum, generally near 3×10^{-6} torr.

The scintillators are Bicron BC408 plastic connected to lucite light pipes which are viewed by Hamamatsu R329 photomultiplier tubes with high-current transistorized bases. The size of the scintillators was determined by allowing for the acceptance of the NaI detector and straggling effects in the target. For the $^{1}H(d,\gamma)^{3}He$ experiment, small 7.6 cm $\times$ 7.6 cm scintillators are used. However, for the $^{4}He(d,\gamma)^{6}Li$ experiment larger (17.8 cm $\times$ 33.0 cm) scintillators are used, since the ^{6}Li recoils must pass through the gas cell exit foil, which causes energy straggling and therefore spreads them out in position. The scintillators are connected to 5.08 cm round light pipes for transmission of the light pulses through vacuum feedthroughs and to the photomultiplier tubes. An adiabatic strip light pipe was placed between the scintillator and the round light pipe to improve light collection in the $^{4}He(d,\gamma)^{6}Li$ case. To reduce background, the light pipes and rear scintillator are covered with aluminized Mylar. The front scintillator cannot be covered as the ^{6}Li recoils would stop in the Mylar.

A fast coincidence circuit between the NaI and recoil detectors was set up to identify the γ rays of interest. Signals from both scintillators were first sent through a bipolar amplifier. The front scintillator signal then passed into a linear fan out where one output was sent into a 300 Mhz discriminator and then into a four-fold logic unit. Here, events in coincidence with the rear scintillator are gated out. This signal was then used as the stop for a time-amplitude converter (TAC), the start coming from the fast output of the NaI discriminator. The TAC signals were then sent to an ADC to be stored in the computer. Coincidences were seen as a peak in the TAC spectrum. The second output of the linear fan out was sent through a fast linear gate triggered on the fast NaI discriminator output and into an ADC for storage in the computer. Timing for the linear gate was determined by using a neutron detector and an Americium-Berylium (Am-Be) source. The neutron detector consisted of an encapsulated liquid scintillator connected to a photomultiplier tube and base. By placing the Am-Be source between the neutron and NaI detectors, the 4.44 MeV γ rays and associated neutrons could be detected in coincidence. To insure accurate timing, the front scintillator signal cable was used for the neutron detector. This technique proved invaluable in setting up the coincidence circuit between the γ ray and recoil detectors. The electronic circuit is given in Figure D.3.2.

Beam quality plays an important role in the detection of the recoil nuclei. Poor focusing and scattering from slits and chamber walls can increase the scintillator background. To aid in beam tuning, several diagnostic elements were installed in the beam line. Two quartz beam viewers were placed in the beam line, one between the final quadrupole and target and the second just upstream of the beam dump. Also a phosphorus target was used to view the beam at the target position. A beam scanner positioned just upstream of the target provided additional beam diagnostics. Beam current was read from several sources, including a collimator 7.6 cm in front of the target,

apertures placed on the target ladder, and the beam dump. In addition, current was read from a 2.54 cm × 2.54 cm tantalum stop placed on a moveable probe located near the beam dump. By tuning onto the current probe, the beam spot size at this position was minimized, which decreased the background. The current probe also allowed for tracking of the beam when the bending magnet was engaged.

A computer code has been developed to simulate the recoil events. The code R_SPOT uses Monte Carlo techniques to determine the recoil and beam particles' trajectories. The program includes the NaI detector acceptance, kinematic, target straggling, and exit window straggling effects. The program has been quite useful in determining optimal target-scintillator detector configurations. It also allows for estimation of the location of the beam relative to the recoil particles. The source code is given in Appendix D.5.

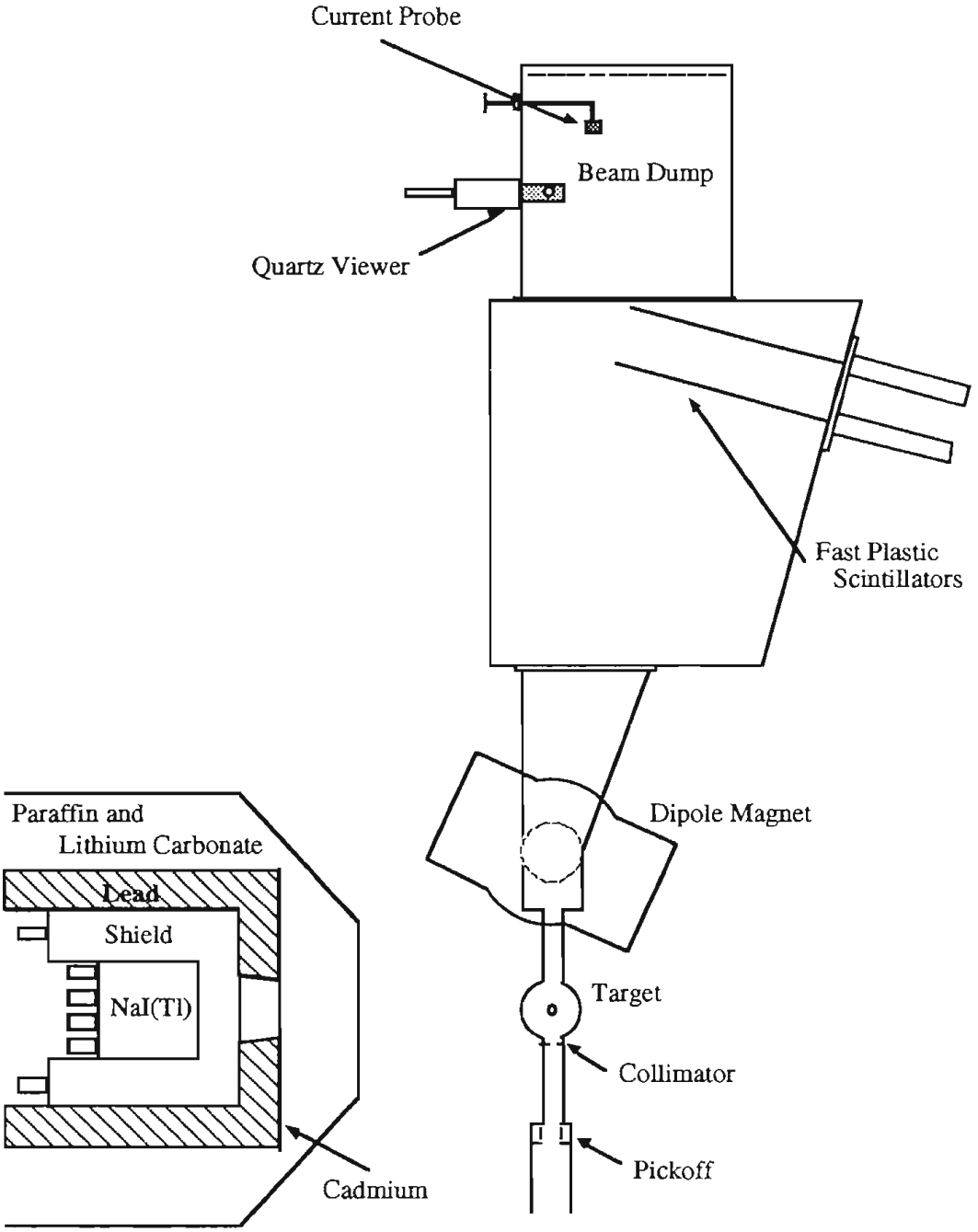

FIG. D.3.1 Experimental setup for the γ ray-recoil detection system including the NaI spectrometer, dipole bending magnet, and recoil scintillators.

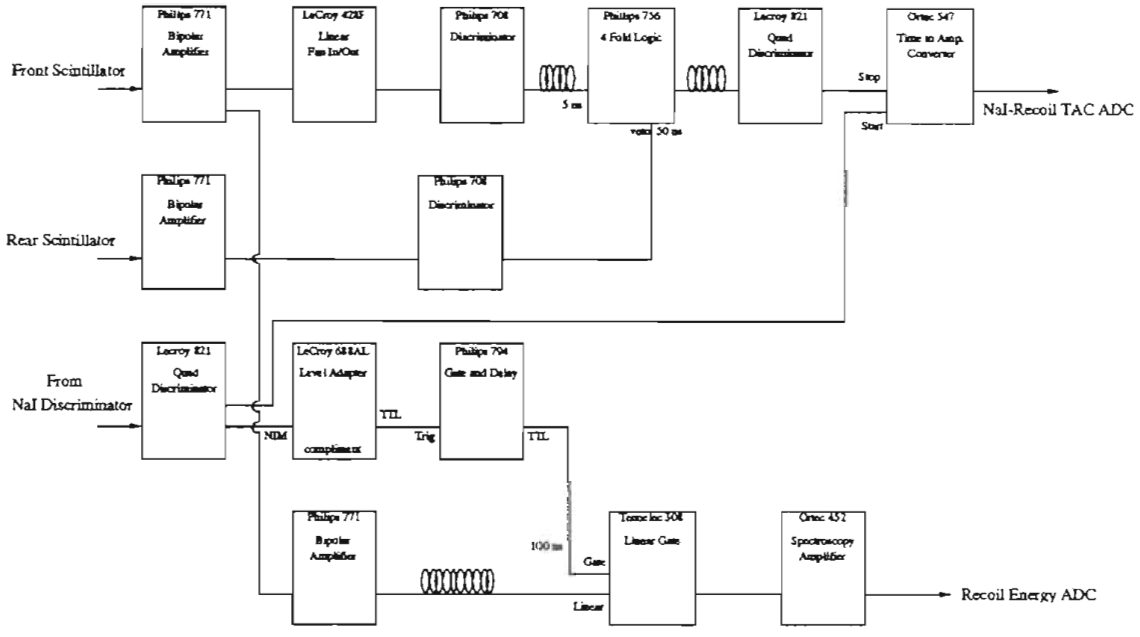

FIG. D.3.2 Electronic circuit used for the γ ray-recoil fast coincidence condition in the $^{1}H(d,\gamma)^{3}He$ experiment.

D.4 NaI-recoil System Development Runs

Seven development runs have been completed at the present time, including a beam line commissioning, NaI detector testing, and several γ ray-recoil coincidence test runs. The NaI detector performance was tested using the $^{3}H(p,\gamma)^{4}He$ reaction with 6.5 MeV protons, which produced 25.6 MeV γ rays. The detector response function is shown in Figure D.4.1. The measured resolution at this energy was found to be $(3.0 \pm 0.2)\%$. Correcting the data for kinematic broadening and target thickness has a small effect, reducing the resolution to 2.9%. The detector response was then fit to a function composed of exponentials of polynomials in the energy, identical to the form given in Section 3.4. The result of the fit is included in Figure D.4.1. This empirical form is inserted into our line shape fitting routine for analysis of the capture γ-ray spectra.

The γ ray-recoil system has been successfully tested with both the $^{2}H(p,\gamma)^{3}He$ and $^{1}H(d,\gamma)^{3}He$ reactions. The test runs have taught us the techniques necessary to perform the actual experiments. We found that one important factor is the beam tune quality, since the recoil detectors are very sensitive to scattered particles. The first step of every run was to establish a high quality, stable beam tune. It was especially critical to have a good focus behind the target near the scintillators.

Determining the desired field strength for the bending magnet was the first step in detecting recoils. Since the recoils experience effects due to the whole magnetic field, including fringe fields, it was not possible to calculate the exact magnetic field necessary. An iterative approach was thereby used to find the field setting. An estimate of the field was first made by using the Monte Carlo simulation code R_STOP. This provided an

estimate of the location of the deflected beam when the recoils should be incident upon the scintillators. With this information, the current probe was placed at the expected beam position, and the magnetic field was increased until the beam was on the probe. Next a short run was taken and the γ ray-recoil TAC spectrum was examined for coincidences. Coincidences appeared as a peak in the TAC spectrum. Many short runs were taken at different magnetic fields to identify the best magnetic field setting, *i. e.* the largest TAC peak. This technique proved most successful.

With the magnetic field set, other parameters were fine tuned. The recoil detector threshold was adjusted to achieve the best foreground-to-background ratio in the TAC spectrum. The gain of the recoil was adjusted to achieve a good energy spectrum. While the TAC condition provided coincidence information, the recoil detector energy spectrum provided diagnostic information. Finally, spectrum gating requirements were set.

The resulting spectra from a test run are shown in Figures D.4.2, D.4.3, and D.4.4. These are from a $^1H(d,\gamma)^3He$ run at $E_d(lab) = 15$ MeV and $\theta = 90°$. A solid CH_2 target was used, 1.18 mg/cm^2 thick. Figure D.4.2 illustrates the γ ray-recoil TAC spectrum. The peak corresponds to the γ ray-^{3}He coincidence events. The top plot in Figure D.4.3 is the NaI energy spectrum, and the bottom plot is the corresponding energy spectrum which has been gated on the TAC coincidence peak. The importance of the coincidence requirement is evident. Figure D.4.4 illustrates the corresponding recoil detector spectra. The top plot is the raw recoil detector energy spectrum, and the bottom gives the same spectrum gated on the TAC coincidence peak. Again, the ^{3}He recoil events are selected out with the coincidence requirement. This also illustrates that the ^{3}He recoils are above the recoil detector threshold.

These test runs have shown the feasibility of the $^1H(d,\gamma)^3He$ experiment. Test runs for the $^4He(d,\gamma)^6Li$ experiment will be pursued in the near future. Data taking for

both experiments should commence shortly thereafter. We recently had a test run with the upgraded tandem. We found the tandem to be very stable at 18 MeV and were able to detect ^{3}He recoils from the $^{1}H(d,\gamma)^{3}He$ reaction. There were also indications that the tandem should be capable of producing 20 MeV deuteron beams. This extra energy should simplify the experiments, since the recoils are easier to detect at higher energies. These results are very encouraging, and hopefully the experiments will lead to a better understanding of the D-state in ^{3}He and ^{6}Li.

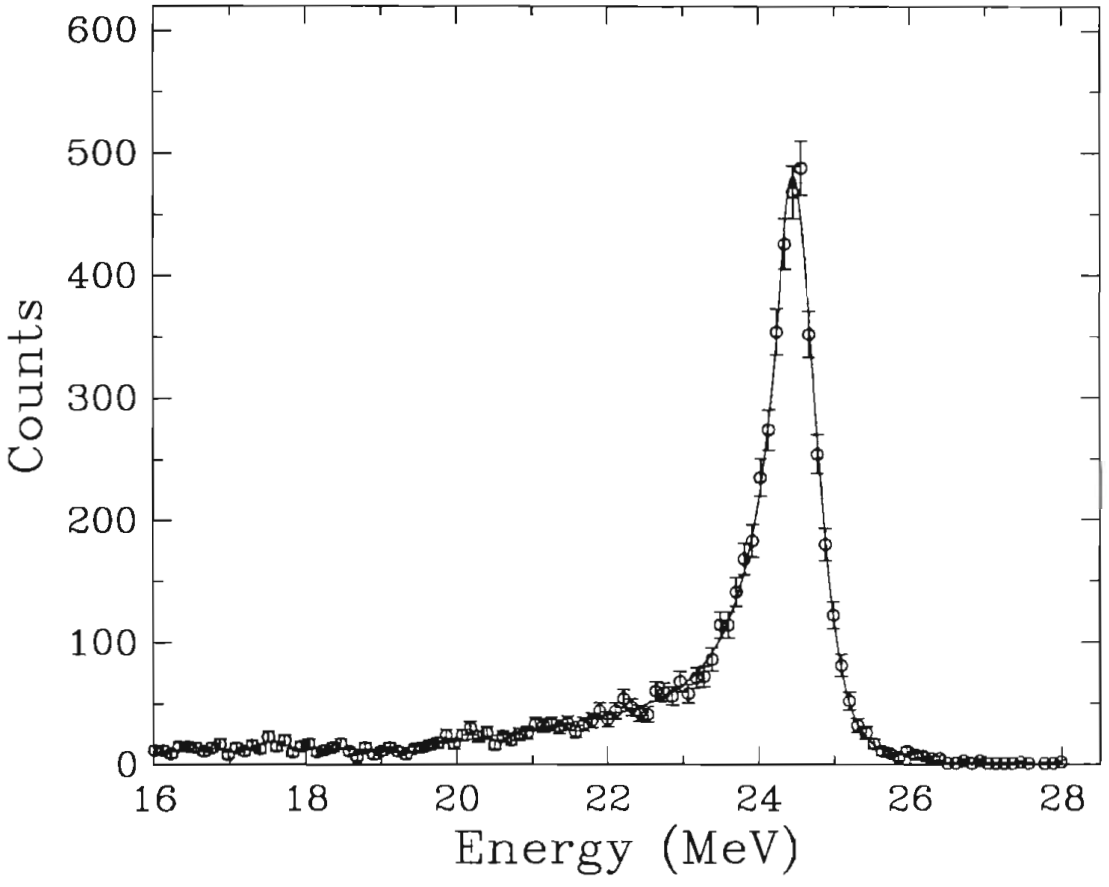

FIG. D.4.1 NaI detector response, as measured in the $^{3}H(p,\gamma)^{4}He$ reaction with 6.5 MeV protons. The solid curve is the result of the fit to a composite function, as discussed in the text.

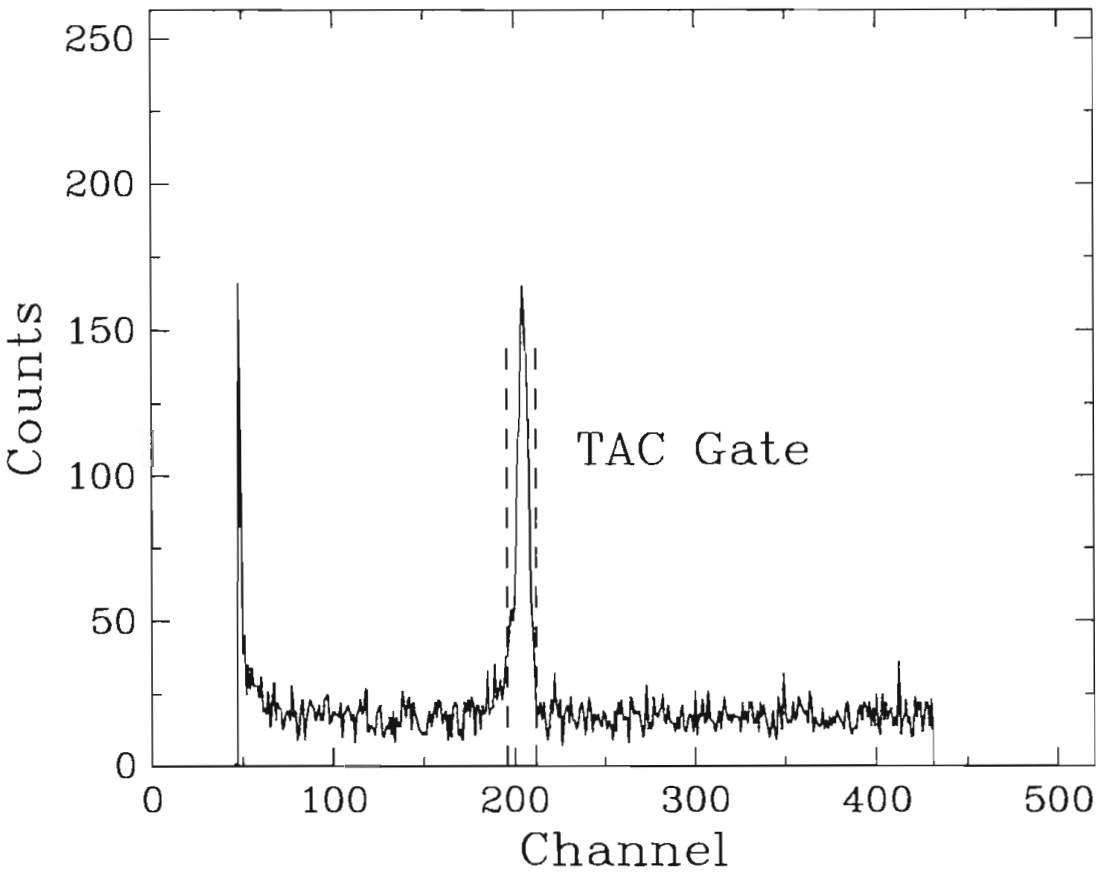

FIG. D.4.2 Capture γ ray-recoil TAC spectrum from the test run of the γ ray-recoil detection system using the $^{1}H(d,\gamma)^{3}He$ reaction with 15 MeV deuterons and θ - 90°. The peak corresponds to the γ ray-3He recoil events. The coincidence gate is included in the figure.

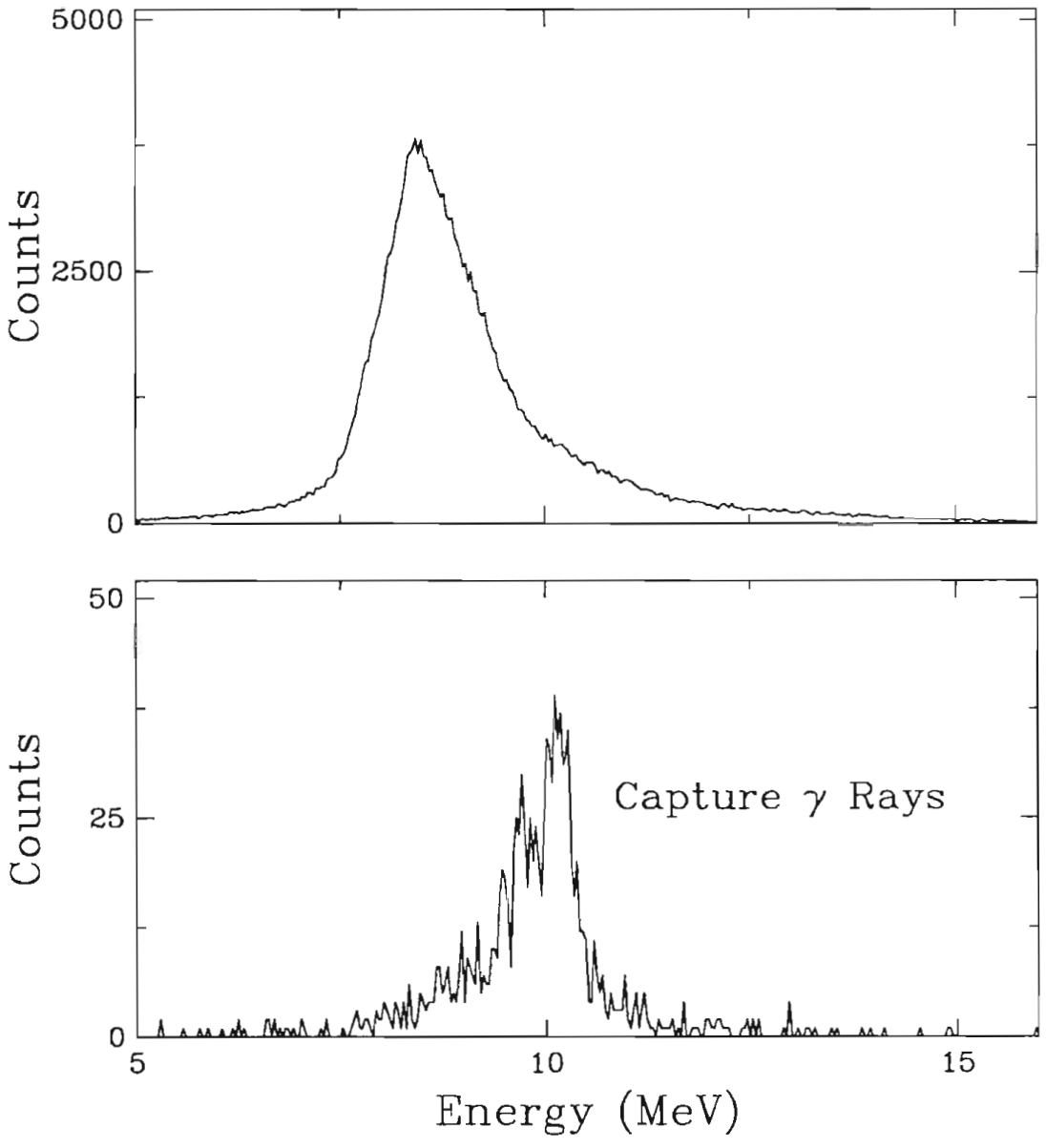

FIG. D.4.3 NaI detector energy spectra from the test run of the γ ray-recoil detection system using the $^{1}H(d,\gamma)^{3}He$ reaction with 15 MeV deuterons and θ - 90°. The top is the raw NaI spectrum and the bottom is the NaI spectrum which results from gating on the TAC coincidence peak.

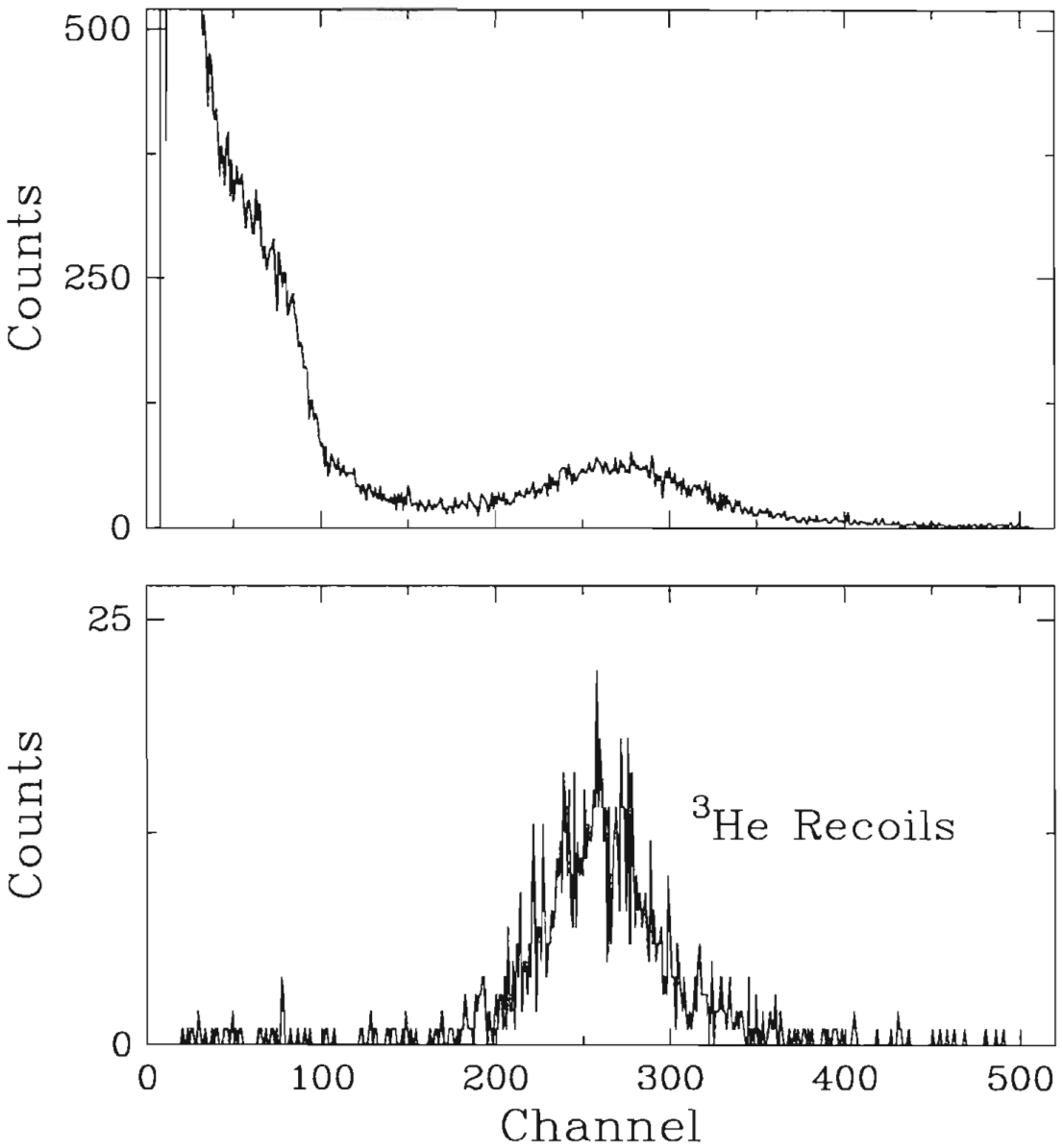

FIG. D.4.4 Recoil detector spectra from the test run of the γ ray-recoil detection system using the ^{1}H(d,γ)^{3}He reaction with 15 MeV deuterons and θ - 90°. The top shows the raw recoil detector energy spectrum and the bottom shows same spectrum after gating on the TAC coincidence peak. Events corresponding to ^{3}He recoils are selected out with the coincidence requirement.

D.5 Recoil Simulation Code - R_STOP

Below is the recoil detector simulation code, described in Appendix D.3. The code uses Monte Carlo techniques to determine the recoil and beam particles' trajectories. The program includes the NaI detector acceptance, kinematic, target straggling, and exit window straggling effects. Sample input and output files are given following the source code.

```
C  VS01$DUA0:[KRAMER.RECOIL]R_SPOT.FOR
C       Monte Carlo simulation of recoil particles for the 70 degree capture
C       beam line.  Recoil nuclei are tracked from the target through a
C       magnetic field and onto the detector plane.  Included are NaI detector
C       acceptance, kinematic, target straggling, and exit window straggling
C       effects.
C
C       by Laird Kramer, 7/90
C
C  Inputs:
C       UNIT 10:  Configuration information
C  Outputs:
C       UNIT 20:  Standard output
C       UNIT 30:  Plot of recoils, x-y plane, back view
C       UNIT 35:  Plot of detector, x-y plane, back view
C       UNIT 40:  Plot of recoils, x-z plane, top view
C
C  Input Variables:
C
C
C       IZP             Z of projectile
C       IAP             A of projectile
C       IZT             Z of target
C       IAT             A of target
C       IZS             Z of scatterer
C       IAS             A of scatterer
C       IZR             Z of recoil nucleus
C       IAR             A of recoil nucleus
C       PRES            target gas pressure (atm)
C       TEMP            target gas temperature (K)
C       APM             atoms per molecule for target gas
C       LTGT            length of target (cm)
C       ZFOIL           Z of exit foil
```

```
C       AFOIL           A of exit foil
C       FOILTHK         exit foil thickness (mg/cm^2)
C       DIST            distance to back face of NaI (cm)
C       ANGLED          NaI detector angle (degree)
C       DNAI            diameter of NaI (cm)
C       MAGDIS          distance from target to center of magnet (cm)
C       BWIDTH          effective width of magnetic field (cm)
C       BFACT           strength of magnetic field (BFACT * BDATA(I) = Gauss)
C       DELTA           tracking increment (cm)
C       SCINDIS         distance to front of scintillator (cm)
C       XSCINT1         distance from beam to near edge of scintillator (cm)
C       XSCINT2         distance from beam to far edge of scintillator (cm)
C       YSCINT          half height of scintillator (cm)
C       ELAB            incident energy (MeV)
C       NTRIES          number of events
C       IXYPLOT         = 1 for x-y plot
C       IXZPLOT         = 1 for x-z plot
C       NDATA           number of magnetic field data points
C       RDATA(I)        array of radii for magnetic field data (cm)
C       BDATA(I)        array of magnetic field strengths (BFAC * BDATA = Gauss)
C
C       USEFUL CONSTANTS
C       c = 3.00 E+10   cm/sec
C       R = 8.31441     J/(K mole)
C       e = 1.602 E-19  C
C       mole = 6.02 E+23 particles
C       amu = 1.661 E-27 kg

        IMPLICIT NONE

        CHARACTER*3 NUCLEI(0:20,0:20)

        REAL ZPROJ, APROJ, ZTGT, ATGT, ZSCAT, ASCAT, ZRES, ARES
        REAL PRES, TEMP, APM, LTGT, ZFOIL, AFOIL, FOILTHK
        REAL DIST, ANGLED, DNAI, SCINDIS, XSCINT1, XSCINT2, YSCINT
        REAL MAGDIS, BWIDTH, BFACT, ELAB, DELTA
        REAL BDATA(100), RDATA(100), BRADIAL(0:1000)
        REAL X1, X2, Y1, Y2, R, BRMAX, R1, R2
        REAL DEGTORAD, RADTODEG, PI, AMU, ERROR, RNAI, TGTDENS, TGTTHK
        REAL XNAI, YNAI, ZEVENT, ANGLE, ANGLOUTD, ANGLOUT
        REAL THETAC, THETA, PHI, PHIS, THETAS, THETASD
        REAL EOUT, EKIN, ELOSS, EMASS
        REAL SIG1, SIG2, SIGMA, XGAUSS, YGAUSS
        REAL VEL, RADIUS, THET2, PHI2, YLEN
        REAL ANG, ANGP, X, Z, XHIT, YHIT
        REAL SUMX, SUMXSQ, STDEVX, MAXX, MINX
        REAL SUMY, SUMYSQ, STDEVY, MAXY, MINY
        REAL SUME, SUMESQ, STDEVE, MAXE, MINE, EFFC

        REAL*8 G(20), DANGLOUTD, DEOUT
```

```
      INTEGER IZP, IAP, IZT, IAT, IZS, IAS, IZR, IAR
      INTEGER NTRIES, NDATA, IXYPLOT, IXZPLOT
      INTEGER ISEED, IERROR, IBAD, IMISS, IHITS
      INTEGER IXYFILE, IXYDETFILE, IXZFILE
      INTEGER INDEX, I, J, IRMAX

      DATA NUCLEI(0,0), NUCLEI(1,1),NUCLEI(2,1), NUCLEI(3,2),
     .         NUCLEI(4,2), NUCLEI(6,3)
     .         /' G ', ' P ', ' D ', '3He', '4He', '6Li'/

C     Data Input

      READ(10,*) IZP, IAP, IZT, IAT, IZS, IAS, IZR, IAR
      READ(10,*) PRES, TEMP, APM, LTGT, ZFOIL, AFOIL, FOILTHK
      READ(10,*) DIST, ANGLED, DNAI, MAGDIS, BWIDTH, BFACT, DELTA
      READ(10,*) SCINDIS, XSCINT1, XSCINT2, YSCINT, ELAB, NTRIES
      READ(10,*) IXYPLOT, IXZPLOT, NDATA

C     Setup Parameters

      AMU = 931.5016
      PI = 4. * ATAN(1.)
      DEGTORAD = PI / 180.
      RADTODEG = 180. / PI
      RNAI = DNAI / 2.
      ANGLE = ANGLED * DEGTORAD
      SUMX = 0.
      SUMXSQ = 0.
      MAXX  = 0.
      MINX  = 1000.
      SUMY = 0.
      SUMYSQ = 0.
      MAXY  = 0.
      MINY  = 0.
      SUME = 0.
      SUMESQ = 0.
      MAXE = 0.
      MINE = 10000.
      IHITS = 0
      IMISS = 0
      IBAD = 0
      ISEED = 549632111
      IXYFILE = 30
      IXYDETFILE = 35
      IXZFILE = 40

      APROJ = IAP + EMASS(IAP, IZP)/AMU
      ATGT  = IAT + EMASS(IAT, IZT)/AMU
      ASCAT = IAS + EMASS(IAS, IZS)/AMU
      ARES  = IAR + EMASS(IAR, IZR)/AMU
      ZPROJ = FLOAT(IZP)
```

```
      ZTGT  = FLOAT(IZT)
      ZSCAT = FLOAT(IZS)
      ZRES  = FLOAT(IZR)

      TGTDENS = PRES * APM * ATGT * 101.3 / TEMP / 8.31441
                              ! Target Thickness / Length  (mg/cm^3)

C     Scintillator Position Output

      IF ( IXYPLOT .EQ. 1 ) THEN
        WRITE(IXYDETFILE,*) XSCINT1, YSCINT
        WRITE(IXYDETFILE,*) XSCINT2, YSCINT
        WRITE(IXYDETFILE,*) XSCINT2, YSCINT * (-1.)
        WRITE(IXYDETFILE,*) XSCINT1, YSCINT * (-1.)
        WRITE(IXYDETFILE,*) XSCINT1, YSCINT
      ENDIF

C     Magnetic Field Input and Manipulation

      DO I = 1, NDATA
        READ(10,*) RDATA(I), BDATA(I)
      ENDDO

C     Field at Bwidth Assumed Zero

      BDATA(NDATA + 1) = 0.
      RDATA(NDATA + 1) = BWIDTH/2.
      BDATA(NDATA + 2) = 0.
      RDATA(NDATA + 2) = BWIDTH

C     Field Interpolation

      IRMAX = NINT( 2. * BWIDTH ) + 10        !  Maximum Radius in 1/4 cm's
      X1 = RDATA(1)
      X2 = RDATA(2)
      Y1 = BDATA(1)
      Y2 = BDATA(2)
      J  = 1

      DO I = 0, IRMAX
        R = I/4.
        IF (R .LT. X2) THEN
          BRADIAL(I) = ((Y2-Y1)*(R-X1)/(X2-X1) + Y1)*BFACT
        ELSE
          X1 = X2
          Y1 = Y2
          X2 = RDATA(J+2)
          Y2 = BDATA(J+2)
          J  = J + 1
          BRADIAL(I) = ((Y2-Y1)*(R-X1)/(X2-X1) + Y1) * BFACT
        ENDIF
```

```
          IF ( BRADIAL(I) .LT. 0. ) THEN
            WRITE(6,*) '*** WARNING ***'
            WRITE(6,*) '*** NEGATIVE MAGNETIC FIELD CALCULATED ***'
            WRITE(6,*) '*** MAGNETIC FIELD INTERPOLATION ERROR ***'
            WRITE(6,*) '*** PROGRAM TERMINATED ***'
            STOP
          ENDIF
        ENDDO

C   Find Last Non-Zero Magnetic Field Point

        BRMAX = 0.
        DO I = 0, IRMAX
          IF (BRADIAL(I) .GT. 0.) BRMAX = I/4.
        ENDDO

C   Main Loop

        DO 500 I = 1, NTRIES

100       XNAI = RAN(ISEED) * DNAI - RNAI        ! Random X in NaI (cm)
          YNAI = RAN(ISEED) * DNAI - RNAI        ! Random Y in NaI (cm)
          IF ((XNAI**2 + YNAI**2) .GT. DNAI**2) GO TO 100
          ZEVENT = RAN(ISEED) * LTGT - LTGT/2.   ! Random Z in Target (cm)

C   Calculate Angles

          THETAC = ATAN2( XNAI - ZEVENT * SIN(ANGLE),
     .                    DIST - ZEVENT * COS(ANGLE) )
          THETA = ANGLE - THETAC
          PHI = ATAN2( YNAI, DIST - ZEVENT * COS(ANGLE) )
          PHIS = ATAN2( YNAI, ( DIST - ZEVENT * COS(ANGLE) ) / COS(THETAC)
     .                        * SIN(THETA) )
          THETAS = ATAN2( YNAI/SIN(PHIS),
     .                   (DIST - ZEVENT * COS(ANGLE)) / COS(THETAC)
     .                        * COS (THETA) )
          THETASD = THETAS * RADTODEG
          TGTTHK = ( LTGT/2. - ZEVENT ) * TGTDENS        ! mg/cm^2

C   Kinematics for Reaction

          CALL SRKIN(ELAB,APROJ,ATGT,ASCAT,ARES,0.0,THETASD,
     .          G(1),G(2),G(3),DEOUT,G(4),G(5),G(6),G(7),G(8),
     .          G(9),G(10),G(11),G(12),G(13),G(14),DANGLOUTD)

          EOUT = SNGL(DEOUT)
          ANGLOUTD = SNGL(DANGLOUTD)

C   Energy Loss in the Target

          CALL ENLOSS(EOUT,ARES,ZRES,ATGT,ZTGT,TGTTHK,0.,0.,0.,
```

```
     .                    ELOSS,IERROR)

          IF ( IERROR .NE. 0 ) GO TO 900
        EKIN = EOUT - ELOSS/2.
        EOUT = EOUT - ELOSS

C   Angle Staggling Through the Target

        CALL MULTSCAT(ZTGT,ZRES,ATGT,ARES,TGTTHK,EKIN,SIG1,IERROR)

C   Energy Loss in Foil

        CALL ENLOSS(EOUT,ARES,ZRES,AFOIL,ZFOIL,FOILTHK,0.,0.,0.,
     .                    ELOSS,IERROR)

          IF ( IERROR .NE. 0 ) GO TO 900
        EKIN = EOUT - ELOSS/2.
        EOUT = EOUT - ELOSS

C   Angle Straggling Through the Foil

        CALL MULTSCAT(ZFOIL,ZRES,AFOIL,ARES,FOILTHK,EKIN,SIG2,IERROR)

        SIGMA = (SIG1**2+SIG2**2)**0.5
        IF ( SIGMA .GT. (PI/3.)) GO TO 100
        ANGLOUT = ANGLOUTD * DEGTORAD

C   Use Box-Muller Method for Generating Straggling Gaussian
C     see Kalos and Whitlock, "MONTE CARLO METHODS Volume I: Basics"
C     John Wiley & Sons, New York (1986).

        R1 = RAN(ISEED)
        R2 = RAN(ISEED)
        XGAUSS = SIGMA * (-2.*ALOG(R1))**0.5 * COS(2.*PI*R2)
        YGAUSS = SIGMA * (-2.*ALOG(R1))**0.5 * SIN(2.*PI*R2)

C   Outgoing Angles from Target

        THET2 = ATAN( TAN(ANGLOUT) * COS(-PHIS) )
        PHI2  = ATAN( TAN(ANGLOUT) * SIN(-PHIS) * COS(THET2) )
        THET2 = THET2 + XGAUSS
        PHI2  = PHI2  + YGAUSS

C   X, Z Position at Beginning of Magnet Field

        Z = (MAGDIS - ( MAGDIS**2 - ( 1. + TAN(THET2)**2) *
     .          (MAGDIS**2 - BRMAX**2))**.5 )/ (1.+TAN(THET2)**2.
        X = ( Z - ZEVENT) * TAN(THET2)
        YLEN = ( X**2 + Z**2 )**0.5
        ANG = THET2
        VEL = 3.E+10 * (1. - ((ARES*AMU)/(ARES*AMU+EOUT))**2)**.5     ! cm/sec
```

```
      INDEX = NINT((((Z-MAGDIS)**2 + X**2)**.5)*4.)

      IF ( IXZPLOT .EQ. 1 ) THEN
        WRITE(IXZFILE,*) 0., 0.
        WRITE(IXZFILE,*) X, Z
      ENDIF

C     Track Through Magnet Field

250   INDEX = NINT((((Z-MAGDIS)**2 + X**2)**.5)*4.)

      IF (BRADIAL(INDEX) .EQ. 0. ) GO TO 300
      RADIUS = ARES * VEL * 1.0368E-4 / ZRES / BRADIAL(INDEX)    ! cm
      ANGP = ATAN(DELTA/RADIUS)
      ANGP = ANG + ANGP
      YLEN = YLEN + DELTA
      X = X + DELTA * SIN(ANGP)
      Z = Z + DELTA * COS(ANGP)
      ANG = ANGP

      IF ( IXZPLOT .EQ. 1 ) WRITE(IXZFILE,*) X,Z
      IF ( Z .LT. (MAGDIS + BWIDTH/2.) ) GO TO 250

300   THET2 = ANG
      XHIT = X + ( SCINDIS - Z ) * TAN(THET2)
      YLEN = YLEN + ( (XHIT - X)**2 + (SCINDIS - Z)**2 )**0.5
      YHIT = YLEN * TAN(PHI2)

      IF ( IXYPLOT .EQ. 1 ) WRITE(IXYFILE,*) XHIT, YHIT
      IF ( IXZPLOT .EQ. 1) WRITE(IXZFILE,*) XHIT, SCINDIS

C     Hit Statistics

      SUMX   = SUMX + XHIT
      SUMXSQ = SUMXSQ + XHIT * XHIT
      SUMY   = SUMY + YHIT
      SUMYSQ = SUMYSQ + YHIT * YHIT
      SUME   = SUME + EOUT
      SUMESQ = SUMESQ + EOUT * EOUT

      IF (XHIT .GT. XSCINT1)THEN
        IF (ABS(YHIT) .LT. YSCINT ) THEN
          IF (XHIT .LT. XSCINT2) IHITS = IHITS + 1     ! Hits in Scint
        ENDIF
      ENDIF

      IF ( XHIT .LT. MINX ) MINX = XHIT
      IF ( XHIT .GT. MAXX ) MAXX = XHIT
      IF ( YHIT .LT. MINY ) MINY = YHIT
      IF ( YHIT .GT. MAXY ) MAXY = YHIT
      IF ( EOUT .LT. MINE ) MINE = EOUT
```

```
        IF ( EOUT .GT. MAXE ) MAXE = EOUT

        GO TO 950

900     IBAD = IBAD + 1          ! Number of Error Return Codes From ENLOSS

950     CONTINUE

500     CONTINUE

C   Parameter Output and Statistics

        STDEVX = SQRT(ABS((SUMXSQ - SUMX**2/NTRIES)/NTRIES))
        STDEVY = SQRT(ABS((SUMYSQ - SUMY**2/NTRIES)/NTRIES))
        STDEVE = SQRT(ABS((SUMESQ - SUME**2/NTRIES)/NTRIES))

        EFFC = FLOAT(IHITS)/FLOAT(NTRIES)

        IF ( IBAD .GT. 1 ) THEN
          WRITE(6,*) '*** ENLOSS ERRORS = ', IBAD
        ENDIF

C   Output to Unit 020

        WRITE(20,2000) NUCLEI(ATGT,ZTGT),NUCLEI(APROJ,ZPROJ),
     .                 NUCLEI(ASCAT,ZSCAT),NUCLEI(ARES,ZRES), ELAB
2000      FORMAT(15X,A3,'(',A3,',',A3,')',A3,'  at ',
     .                 F4.1,' MeV',/)

        WRITE(20,*)'      NaI          NaI          Scint        Scint      ',
     .                 '  Scint       Scint'
        WRITE(20,*)'     Angle        Dist.         Dist.         X-1       ',
     .                 '    X-2         Hgt.'
        WRITE(20,2010) ANGLED, DIST, SCINDIS, XSCINT1, XSCINT2, YSCINT
2010      FORMAT(4X,F5.1,' deg',4X,F5.1,' cm',4X,F5.1,' cm',4X,F5.1,
     .                 ' cm',4X,F5.1,' cm',3X,F5.1,' cm',/)

        WRITE(20,*)' Target:    Pres.       Temp.       A/M      Length ',
     .                 '       Thickness'
        WRITE(20,2020) PRES, TEMP, APM, LTGT, TGTDENS * LTGT
2020      FORMAT(9X,F5.2,' atm',4X,F5.1,' K',4X,F4.1,4X,
     .                 F5.2,' cm',4X,F5.2,' mg/cm^2'/)

        WRITE(20,*)'      Foil         Zfoil    Afoil     Mag. Field',
     .                 '    Iterations     Efficiency'
        WRITE(20,2030) FOILTHK,ZFOIL,AFOIL,BFACT,NTRIES,EFFC*100.
2030      FORMAT(1X,F5.2,' mg/cm^2',4X,F5.2,3X,F5.2,4X,F7.1,' G',
     .                 6X,I6,7X,F6.2,' %'/)

        WRITE(20,*)'                X            Y       Energy'
        WRITE(20,*)'-------------------------------------------'
```

```
      WRITE(20,2050)SUMX/NTRIES, SUMY/NTRIES, SUME/NTRIES
2050    FORMAT(' Average |',3X,F7.3,5X,F7.3,4X,F5.2)
      WRITE(20,2060)MINX,MINY,MINE
2060    FORMAT(' Minimum |',3X,F7.3,5X,F7.3,4X,F5.2)
      WRITE(20,2070)MAXX,MAXY,MAXE
2070    FORMAT(' Maximum |',3X,F7.3,5X,F7.3,4X,F5.2)
      WRITE(20,2080)STDEVX, STDEVY, STDEVE
2080    FORMAT(' St Dev  |',3X,F7.3,5X,F7.3,4X,F5.2)

      END
```

Below are sample input and output files for the R_STOP program. In this example, the $^{1}H(d,\gamma)^{3}He$ reaction with 16 MeV deuterons was modeled. The target was a gas cell with 7.6 μm Kapton exit windows. With a 4 kG field, 99% of the recoils enter the 7.6 cm × 7.6 cm scintillator.

INPUT:

```
1    2    1    1    0    0    2    3
1.          300.        2.          1.905       6.29        12.55       0.836
106.05      90.         25.4        40.         50.         4000.       0.5
180.        29.2        36.8        3.81        16.         1000
0    0    9
 0.0        1.
 2.54       0.99333
 5.08       0.75
 7.62       0.70
10.16       0.41667
12.70       0.25
15.24       0.15
17.78       0.08333
20.32       0.05
```

OUTPUT:

```
                P ( D , G )3He  at 16.0 MeV

      NaI          NaI          Scint        Scint        Scint        Scint
     Angle        Dist.        Dist.         X-1          X-2          Hgt.
    90.0 deg    106.1 cm     180.0 cm      29.2 cm      36.8 cm      3.8 cm

 Target:    Pres.       Temp.       A/M      Length       Thickness
          1.00 atm     300.0 K      2.0      1.90 cm      0.16 mg/cm^2

     Foil          Zfoil    Afoil     Mag. Field    Iterations     Efficiency
 0.84 mg/cm^2       6.29    12.55      4000.0 G         1000          99.10 %

                 X             Y       Energy
-------------------------------------------------
Average |     34.813        -0.049     10.34
Minimum |     32.073        -3.832     10.14
Maximum |     37.617         3.996     10.52
St Dev  |      0.818         1.211      0.08
```

REFERENCES

[And77] H. H. Anderson and J. F. Ziegler, *Hydrogen Stopping Powers and Ranges in All Elements*, (Pergammon, New York, 1977).

[Arr88] A. Arriaga, A. M. Eiró, F. D. Santos, and J. E. Ribeiro, Phys. Rev. C **37**, 2312 (1988).

[Arr91] A. Arriaga, V. R. Pandharipande, and R. Shiavilla, Phys. Rev. C **43**, 983 (1991).

[Ass87] H. J. Assenbaum and K. Langanke, Phys. Rev. C **36**, 17 (1987).

[Bal92] M. J. Balbes, Ph.D. Thesis, unpublished (1992).

[Bar75] C. M. Bartle, NIM **124**, 547 (1975).

[Bar87] C. A. Barnes, K. H. Chang, T. R. Donoghue, C. Rolfs, and J. Kammeraad, Phys. Lett. B **197**, 315 (1987).

[Bas64] R. Bass, W. Kessel, and G. Majoni, NIM **30**, 237 (1964).

[Bet40] H. A. Bethe, Phys. Rev. **57**, 390 (1940).

[Bev69] P. R. Bevington, Data Reduction and Error Analysis for the Physical Sciences, (McGraw-Hill, New York, 1969).

[Bie55] L. C. Biedenharn, R. L. Gluckstern, M. H. Hull, and G. Breit, Phys. Rev. **97**, 542 (1955).

[Bir64] J. B. Birks, *The Theory and Practice of Scintillation Counting*, (Pergamon Press, New York, 1964).

[Blü87] G. Blüge, H. J. Assenbaum and K. Langanke, Phys. Rev. C **36**, 21 (1987).

[Bro90] R. E. Brown and N. Jarmie, Phys. Rev. C **41**, 1391 (1990).

[Cla70] G. Clausnitzer, *et al.*, NIM **80**, 245 (1970).

[Cro91] E. R. Crosson, T. B. Clegg, H. J. Karwowski, and S. K. Lemieux, NIM **A310**, 703 (1991).

[Dar71] S. E. Darden, "Description of Polarization and Suggestions for Additional Conventions", H. H. Barschall and W. Haeberli, ed., Polarization Phenomena in Nuclear Reactions (University of Wisconsin Press, Madison, 1971) p. 39.

[Dol89] P. Doll, *et al.*, NIM **A288**, 464 (1989).

[Dus62] S. Dushman, *Scientific Foundations of Vacuum Technique* (John Wiley and Sons, New York, 1962).

[Eik71] H. Eikenmeier and H. H. Hackenbroich, Nuclear Physics **A169**, 407 (1971).

[Fon91] A. C. Fonseca and D. R. Lehman, Phys. Lett. **B267**, 159 (1991).

[Fow84] W. A. Fowler, Rev. Mod. Phys. **56**, 169 (1984).

[Fri79] J. L. Friar, Phys. Rev. C **20**, 325 (1979).

[Ger41] E. Gerjuoy, J. Schwinger, Phys. Rev. **61**, 138 (1941).

[Hae75] W. Haeberli, in Nuclear Spectroscopy and Reactions, ed. J. Cerny (Academic Press, New York, 1975) Part A, p. 151.

[Hof81] H. M. Hofmann, W. Zahn, and H. Stowe, Nuclear Physics **A357**, 139 (1981).

[Hub69] J. H. Hubbell, *Photon Cross Sections, Attenuation Coefficients, and Energy Absorption Coefficients From 10 keV to 100 GeV*, Nat. Stand. Ref. Data Ser., Nat Bur. Stand. **29** (1969).

[Kel89] H. Kellerman, H. M. Hofmann, and Ch. Elster, Few Body Systems **7**, 31 (1989).

[Lan88] J. L. Langenbrunner, G. Feldman, H. R. Weller, D. R. Tilley, B. Wachter, T. Mertelmeier, and H. M Hofmann, Phys. Rev. C **38**, 565 (1988).

[Lan89] J. L. Langenbrunner, Ph.D. Thesis, unpublished (1989).

[Lan90] J. L. Langenbrunner, H. R. Weller, and D. R. Tilley, Phys. Rev. C **42**, 1214 (1990).

[Leh78] D. R. Lehman, Mamta Rai, and A. Ghouvanlou, Phys. Rev. C **17**, 744 (1978).

[Leh83] D. R. Lehman and W. C. Parke, Phys. Rev. C **28**, 364 (1983).

[Mel86a] S. Mellema, T. R. Wang, and W. Haeberli, Phys. Rev. C **34**, 2043 (1986).

[Mel86b] S. Mellema, T. R. Wang, and W. Haeberli, Phys. Lett. B **166**, 282 (1986).

[Mer88] B. Wachter, T. Mertelmeier, and H. M Hofmann, Phys. Lett. B **200**, 246 (1988).

[Nel85] W. R. Nelson, H. Hirayama, and D. W. O. Rogers, SLAC Report No. 265, (1985).

[Pie87] J. Piekarewicz and S. E. Koonin, Phys. Rev. C **36**, 875 (1987).

[Rar41] V. Rarita, J. Schwinger, Phys. Rev. **59**, 436 (1941).

[Rob81] R. G. H. Robertson, *et al.*, Phys. Rev. C **47**, 1867 (1981).

[Ros53] M. E. Rose, Phys. Rev. **91**, 610 (1953).

[Sey79] R. G. Seyler, H. R. Weller, Phys. Rev. C **20**, 453 (1979).

[Sch39] J. Schwinger, Phys. Rev. **55**, 235 (1939).

[Vet 85] M. C. Vetterli, J. A. Kuehner, A. J. Trudel, C. L. Woods, R. H. Dymarz, A. A. Pilt, and H. R. Weller, Phys. Rev. Lett. **54**, 1129 (1985).

[Wel84] H. R. Weller, P. Colby, N. R. Roberson, and D. R. Tilley, Phys. Rev. Lett. **53**, 1325 (1984).

[Wel86] H. R. Weller, P. Colby, J. Langenbrunner, Z. D. Huang, D. R. Tilley, F. D. Santos, A. Arriaga, and A. M. Eiro, Phys. Rev. C **34**, 32 (1986).

[Wel88] H. R. Weller, R. M. Whitton, J. Langenbrunner, E. Hayward, W. R. Dodge, S. Kuhn, and D. R. Tilley, Phys. Lett. B **213**, 413 (1988).

[Whi86] D. M. Whittal and C. M. Bartle, NIM **A247**, 390 (1986).

[Wil85] F. J. Wilkinson III and F. E. Cecil, Phys. Rev. C **31**, 2036 (1985).

Biography
Laird Hayman Kramer

Personal: Born in Wilmington, Delaware, December 2, 1963

Education: B. A., The George Washington University, May 1986
M. A., Duke University, Durham, North Carolina, February 1989

Positions: Research Assistant, Triangle Universities Nuclear Laboratory, 1987 - 1992
Graduate Teaching Assistant, Duke University, 1986 - 1987
Research Assistant, The George Washington University, 1985 - 1986
Teaching Assistant, The George Washington University, 1984 - 1986

Selected Publications:

Isovector Giant Quadrupole Resonance Observed in $^{30}Si(\vec{p},\gamma)^{31}P$
G. Feldman, L. H. Kramer, H. R. Weller, E. Hayward, and W. R. Dodge,
Physical Review C **43**, 223 (1991).

Ground-State Widths of ^5He and ^5Li Determined in the $^3H(d,\gamma)^5He$ and the $^3He(d,\gamma)^5Li$ Reactions
M. J. Balbes, G. Feldman, L. H. Kramer, H. R. Weller, and D. R. Tilley,
Physical Review C **43**, 343 (1991).

The $^3H(p,\gamma)^4He$ Reaction and the $(\gamma,p)/(\gamma,n)$ Ratio in ^4He
G. Feldman, M. J. Balbes, L. H. Kramer, J. Z. Williams, H. R. Weller, and D. R. Tilley,
Physical Review C **42**, R1167 (1990).

Measurement of the Spin-Rotation Parameters A and R for $\pi^+p \rightarrow \pi^+p$ and $\pi^-p \rightarrow \pi^-p$ Scattering from 471 to 625 MeV/c
D. B. Barlow, R. S. Kessler, G. J. Kim, B. M. K. Nefkens, C. Pillai, J. W. Price, J. A. Wightman, S. Hall, D. W. Lane, S. R. Loe, L. K. Morton, M. E. Sadler, S. D. Adrian, W. J. Briscoe, L. H. Kramer, A. Mokhtari, A. M. Petrov, C. J. Seftor, M. F. Taragin, J. F. Davis, and I. Supek,
Physical Review Letters **62**, 1009 (1989).